UNIVERSITY OF CALIFORNIA

Los Angeles

Design of Noble Metal Nanostructures for Heterogeneous Catalytic Applications

A dissertation submitted in partial satisfaction of the requirements for the degree Doctor of Philosophy in Materials Science and Engineering

by

Michelle Margarita Flores Espinosa

2019

ABSTRACT OF THE DISSERTATION

Design of Noble Metal Nanostructures for

Heterogeneous Catalytic Applications

by

Michelle Margarita Flores Espinosa

Doctor of Philosophy in Materials Science and Engineering

University of California, Los Angeles, 2019

Professor Yu Huang, Chair

Worldwide efforts have been focused to introduce greener chemical and energetic processes that drive the society away from the dependency on fossil fuels, looking to reduce the environmental footprint of modern societies. Catalysis for instance, has been for decades the winning technology which helps to improve the efficiency of processes in petrochemical, pharmaceutical, and biomedical industries to mention a few. Efficiency of catalysts come mostly from its structure and composition which proportionate high activity and selectivity. However, the use of expensive noble metals as catalyst materials remains a key issue for industrial applications. Thus, developing materials that reduce and mitigate carbon dioxide emissions as well as decrease of waste of the materials using during these processes remain a tremendous challenge to overcome. Nanotechnology for instance, is a growing technology with great impact in the industrial,

pharmaceutical and energetical sectors. In fact, nanomaterials provide a better economical option, less waste and still with superior performance than their bulk counterparts which is explained from their reduce size, shape and larger surface areas which leads to overall higher catalytic performance. Nanocatalysis modify the rate of a chemical reaction by speeding up or accelerating the reaction rate without being consumed, making the process more energetically favored. Nanocatalyst have significant impact in different industrial processes as chemical reactions to produce fine chemicals, or for renewable energy and among others. As it was mentioned previously, the high performance of nanocatalyst is associated with the atoms at the surface of the nanostructure which are known as the active sites for catalysis. Moreover, it is well known that surface atoms placed at the corner or edges of the nanocatalyst are more active than those surface atoms at planes, and it the same manner with surface-to-volume ratio, their number will increase with decrease of particle size. In addition to nanoparticle size, crystallographic facets lead to different shapes or morphologies which are also contributing to the number of atoms at the surface, edges and corners. All of these contributing together to the efficiently performance of nanocatalyst for the target reactions . In this thesis is presented nanocatalyst materials development, and studies about their synergetic effect of the different components for heterogeneous catalytic applications.

First, benzaldehyde byproduct is an intermediate in the production of fine chemicals and additives. Tuning selectivity to benzaldehyde is therefore critical in alcohol oxidation reactions at the industrial level where the typical methods employ toxic oxidant chemicals for its production. Herein, we report a simple but innovative method for the synthesis of palladium hydride and nickel palladium hydride nanodendrites with controllable morphology, high stability, and excellent catalytic activity. The synthesized dendrites can maintain the palladium hydride phase even after

their use in the chosen catalytic reaction. Remarkably, the high surface area morphology and unique interaction between nickel-rich surface and palladium hydride (β-phase) of these nanodendrites are translated in an enhanced catalytic activity for benzyl alcohol oxidation reaction. Our Ni/$PdH_{0.43}$ nanodendrites demonstrated a high selectivity towards benzaldehyde of about 92.0% with a conversion rate of 95.4%, showing higher catalytic selectivity than their $PdH_{0.43}$ counterparts and commercial Pd/C. The present study opens the door for further exploration of metal/metal-hydride nanostructures as next-generation catalytic materials.

Second, palladium hydride system (PdHx) has been of great interest primarily due to the high solubility of hydrogen on the palladium fcc (Pd-face centered cubic) lattice which make them suitable candidates as environmental friendly materials for applications in terms of storage and use of energy, having specific relevance in hydrogen storage, fuel cell, batteries, kinetics reversibility studies, and more. Palladium hydride properties do not only include adsorption and desorption of hydrogen, but they are also effective for electrocatalytic applications. Overall, palladium hydride and its alloys properties are strongly correlated with their electronic and crystal structure changes. Thus, a deep understanding and methodology for their production is crucial for their use in the mentioned applications. Despite of the studies found in literature, there is still a lack of studies for direct but simple synthesis of palladium hydride with practical applications. For instance, palladium hydride literature studies are mostly based on in-situ studies where a limitation of sample, stability and reproducibility are some of the major problems associated with them which also leads to a lack of studies related to their properties and how to tune them. Herein, we reported a simple yet well designed method for the synthesis of stable β palladium hydride with different morphologies and decoration of its surface with organic ligands which lead to different effects in

terms of nanocrystal sizes and the ability of tune of its properties. Upon the use of different capping agents during the synthesis, diverse magnetic properties have arisen, as well as an increase in their hydrogen storage capacity. These properties are found to be different from their counterpart of pure palladium and palladium hydride material without coating agents.

Third, developing non-platinum materials with enhance performance for electrocatalytic reactions has been gaining attention in recently years. Palladium and Palladium-based materials are the most suitable candidates to substitute platinum catalysts in anodic and cathodic reactions. Here we developed a facile path to synthesize PdCu nanowires having alloy and intermetallic phases within their structures. To the best of our knowledge, the catalytic properties of *PdCu intermetallic nanowires for hydrogen evolution reaction and formic acid oxidation reaction are higher than their PdCu alloy counterpart and those previously reported for 0D and 1D bimetallic nanostructures. Tafel slopes and overpotential presented here during hydrogen evolution reaction of *PdCu NWs in both acidic and basic conditions are superior than PdCu alloy nanowires, Pd nanowires and comparable to commercial Pt. In terms of formic acid oxidation reaction, *PdCu NWs also exhibits the highest mass activity, followed by PdCu alloy NWs, and being both superior than commercial Pd. In addition, PdCu nanowires also exhibit superior stability for both reactions: hydrogen evolution reaction in acid and basic conditions, and formic acid oxidation reaction as well as good resistance against CO poisoning. Density functional theory (DFT) calculations demonstrate that the improved HER performance at acidic condition is due to the decrease in the hydrogen binding energy of the compressed PdCu-B2 phase, and the improved HER performance at alkaline condition is due to the reduced water dissociation barriers at alkaline condition of *PdCu intermetallic phase.

The dissertation of Michelle Margarita Flores Espinosa is approved.

Mark S. Goorsky

Yong Chen

William M. Gelbart

Yu Huang, Committee Chair

University of California, Los Angeles

2019

Dedicated to my mother Margarita Espinosa,

for her unconditional love, dedication and support

And to my auntie Gloria, for back-up my dreams

Table of Contents

List of Figures

List of Tables

Acknowledgments

First and foremost, I would like to express my gratitude to my advisor Professor Yu Huang whom during these years have been a truly mentor in my professional development, and from whom I have learned to be consistent and honest to my work. Her devotion, perfectionism and specific attention to details towards science projects have impact my life and work ethic, being someone to look up to as a role model of woman in science and technology. I want to use this opportunity to thank Prof. Huang for her support during my research and constant advice, and also for allowing me to express, develop and growth my own ideas which overall have helped me to culminate successfully this stage in my career.

Moreover, I would like to thank my lab members for their collaboration, support, advice and friendship during these years. Special thanks to Dr. Zipeng Zhao, Chungseok Choi, Dr. Hui-Ying Shiu, and the rest of lab members.

To my friends at UCLA, big thanks to all of you. It wouldn't be the same without your constant support and friendship during this challenger path of the Ph.D. studies. You helped to make it lighter to overcome any obstacle in front of us.

Thanks to all my family and closest friends from Ecuador and my family here in the U.S. for all the emotional and physical support here or back at home. Being far away from my home country was by far the hardest part but you have always pushed me to pursue my dreams and finish them successfully. Special thanks to my mom Margarita for all your effort and love for us. Look

where we are thanks to you! Thanks to my sisters María José, Katherine and their respective families for always believe and helped me with anything, literally anything that I needed. And thanks to Dan W. for all your love, support and patience during this process. I love you all immensely, and this milestone is to all of you.

Finally, I would like to thank my committee members: Prof. Mark S. Goorsky, Prof. Yong Chen, Prof. William Gelbart, and Prof. Yu Huang for all your help with this project but also for your advice and taught during my studies here at UCLA. I have been lucky to either being your student in your lectures or have served as teaching assistance in your classes. In either way, I have learned from you not only the science fundaments of nanotechnology, materials or quantum mechanics but also how to become an excellent lecturer, passionate for science and willing to help in the best way to the students. My sincerely gratitude is with all of you. And to all the staff of MSE, thanks.

"There is Plenty of Room at the Bottom"

by Richard Feynman

VITA

Michelle Margarita Flores Espinosa was born in Ecuador (South America). She finished her high school as valedictorian of the year, receiving a full year government scholarship to study at Pontificia Universidad Católica del Ecuador where she finished her undergrad studies. Later on, she was finalist on the Bayer IIV edition Young Warming Global Climate change-2010 and won the Seed Project 2010: development and characterization of activated carbon cloth which was also her final work to obtain her bachelor's degree in analytical chemistry. In 2013, she was awarded with a scholarship of "Top World Universities" program from the Secretary for Higher Education, Science and Technology of Ecuador to pursue her Master studies at UCLA. On January 2016, she started her Ph.D. studies in the same department. Through her Ph.D. studies at UCLA, she was awarded with MSE Department Fellowship during spring 2018, spring 2017 and spring 2016. She joined Dr. Yu Huang`s group in Fall 2014 and conducted research in nanocatalyst for hydrogen storage and electrochemical reactions. She has co-published a paper, submitted a patent with Prof. Y. Huang and X. Duan, and collaborate with other papers. She gave oral presentation in the ACS fall meeting 2019 in San Diego. In addition, she won and was invited to participate in the 136th International Summer Course of BASF SE for PhD students and postdocs in Ludwigshafen, Germany 2019. Her research interests include synthesis, characterization and applications of nanocatalysts for energy storage purposes and electrochemical reactions for fuel cells as a mean of renewable energies.

Education:

- *University of California, Los Angeles* Jan. 2016 – Sep. 2019

  Department of Materials Science and Engineering

  Ph.D. Candidate in Materials Science and Engineering

- *University of California, Los Angeles* Jan. 2014 – Dec. 2015

  Department of Materials Science and Engineering

  MSc. in Materials Science and Engineering

- *Pontificia Universidad Católica del Ecuador* Sep. 2004 – March. 2010

  School of Chemistry

  B.Sc. Chemistry with specialization in Analytical Chemistry.

Selected Publications:

- Oral presentation at ACS Fall 2019 National Meeting & Exposition in San Diego, CA, August 25 - 29, 2019. Division: Division of Energy and Fuels. Session: Sustainable Energy & Water via Innovative Electrocatalytic, Photocatalytic & Hybrid Catalytic Systems
- Synthesis of surface controlled nickel/palladium hydride nanodendrites with high performance in benzyl alcohol oxidation. Z Zhao*, MM Flores Espinosa*, J Zhou, W Xue, X Duan, J Miao, Y Huang, Nano Research, 2019, 1-6.
- Stable Alloy of Palladium Hydride with High Hydrogen Content. U.S. Provisional Patent Application No.: 62/486,276. Tech ID: 29275 / UC Case 2017-729-0. Filing Date: April 17, 2017. Yu Huang, Xiangfeng Duan, Michelle Flores Espinosa.
- A Highly Active Star Decahedron Cu Nanocatalyst for Hydrocarbon Production at Low Overpotentials. Chungseok Choi, Tao Cheng, Michelle Flores Espinosa, Huilong Fei, Xiangfeng Duan, William A. Goddard III, Yu Huang, Adv.Mater.2019, 31, 180540

Chapter 1

1 Introduction

At the present, the effects of global warming are well known and tangible in every community, country and continent. From climate change and increase of global temperature, to sea level rise and oceans acidification, its effects are the results of the increased concentration of atmospheric carbon dioxide (CO_2). Worldwide efforts have been focused to introduce greener chemical and energetic processes that drive the society away from the dependency on fossil fuels, looking to reduce the environmental footprint of modern societies. Catalysis for instance, has been for decades the winning technology which helps to improve the efficiency of processes in petrochemical, pharmaceutical, and biomedical industries to mention a few. Efficiency of catalysts come mostly from its structure and composition which proportionate high activity and selectivity. However, the use of expensive noble metals as catalyst materials remains a key issue for industrial applications. Nanomaterials on the other hand, provides a better economical option, less waste and still with superior performance than their bulk counterparts which is explained from their reduce size, shape and larger surface areas which leads to overall higher catalytic performance.[1,2]

1.1. Nanomaterials

Nanomaterials exhibit improved properties if compared with bulk metal materials which is mainly attributed to the reduction in their size (quantum size effect), leading to large surface areas. Studies have focused on optimizing morphology, concentration and surface engineering towards an enhancement of intrinsic surface reactivity of nanomaterials. All of these features make

nanomaterials as the next suitable candidates for various applications as in nanocatalysis (Figure 1.1).

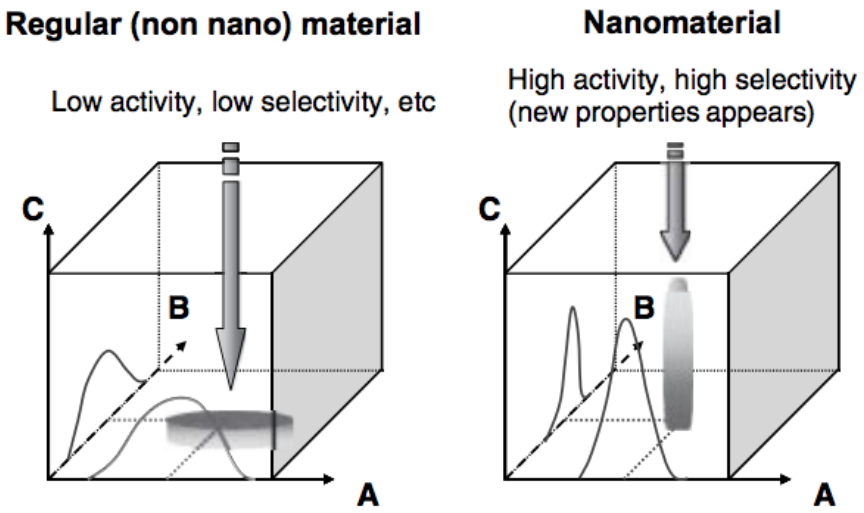

Figure 1.1 Nanoarchitecture: an avenue to superior precision. Axes are: A: composition of functional sites; B: ordering level of sites; C: functional properties of material.

To understand better size effects on the properties of nanomaterials, we can take in consideration two major phenomena occurring at the nanoscale regime. First, if we take as example metal and semiconductors, the relation between occupied and occupied electronic bands are different from atoms to cluster to nanoparticles to finally bulk materials (Figure 1.2). Due to quantum effect, valence band and conduction band split into discrete, quantized, electronic levels which are similar to those in atoms and clusters. As a result, the bandgap is found to increase with decreasing particle sizes because the electron-hole pairs are much closer, thus, Coulombic interaction between them cannot longer be neglected resulting in an overall higher kinetic energy.[1]

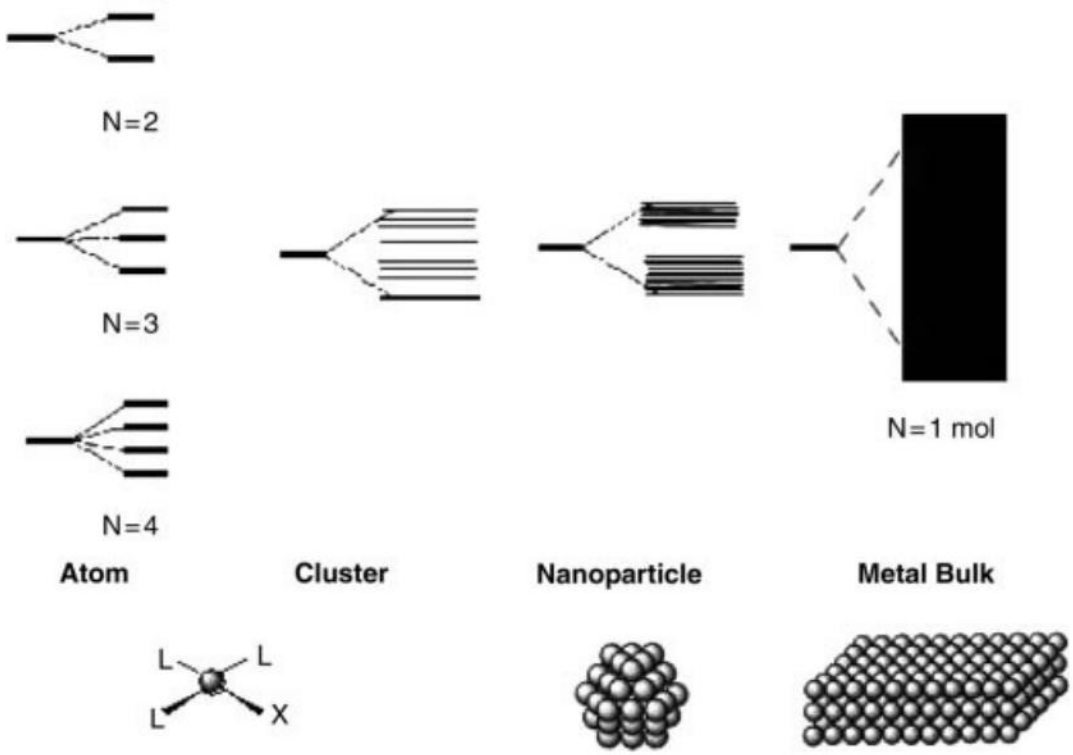

Figure 1.2 Electron levels of atom, cluster, nanoparticle and bulk metal

Second, as the size of the nanomaterials is decreased, the number percentage of atoms at the surface increases. At the end, the surface-to-volume ratio of nanomaterials as nanoparticles will increase the number of active sites on the catalyst surface (Table 1.1, Figure 1.3) while decrease the amount of unused material which happen at bulk scale. Therefore, properties in nanomaterials become mainly dominated by their surface structure. [1,3]

Table 1.1 Number of surface atoms in relation with the total number of atoms in full shell clusters.[1]

Full-shell clusters	Total number of atoms	Number of surface atoms	Surface atoms (%)
1 shell	13	12	92
2 shells	55	42	76
3 shells	147	92	63
4 shells	309	162	52
5 shells	561	252	45
6 shells	923	362	39

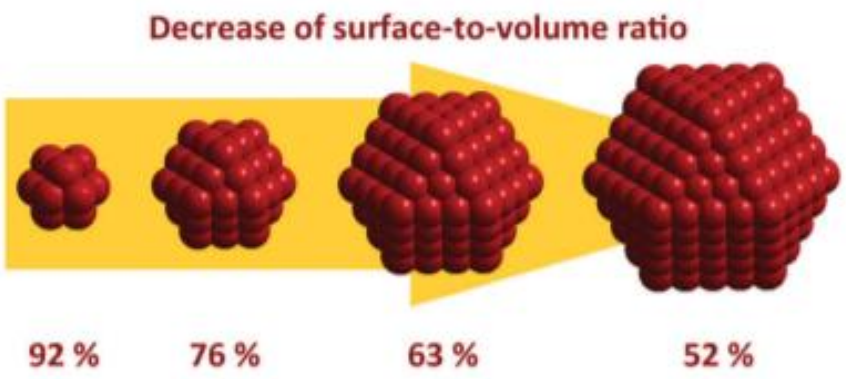

Figure 1.3 Decrease of surface-to-volume ratio for cuboctahedral nanoparticles (fraction of surface atoms given in %).[3]

1.2. Nanocatalyst

Nanocatalysis is a growing technology that employs nanomaterials as catalyst used to modify the rate of a chemical reaction by speeding up or accelerating the reaction rate without being consumed.[4] Nanocatalyst have significant impact in different industrial processes as chemical reactions to produce fine chemicals, or for renewable energy and among others. As it

was mentioned previously, the high performance of nanocatalyst is associated with the atoms at the surface of the nanostructure which are known as the active sites for catalysis. Moreover, it is well known that surface atoms placed at the corner or edges of the nanocatalyst are more active than those surface atoms at planes, and it the same manner with surface-to-volume ratio, their number will increase with decrease of particle size. In addition to nanoparticle size, crystallographic facets lead to different shapes or morphologies which are also contributing to the number of atoms at the surface, edges and corners. For instance, different shapes as octahedral and nanocubes exhibit different number of atoms at the vertices or corners, possessing six vertices or eight vertices respectively which is translated into a lower-coordination-number sites for a higher number of atoms at the vertices. Since a low-coordination number are likely more reactive, it is suggested an increase in the catalytic activity of the nanocatalyst. Therefore, nanocatalysts with different faces are highly desirable to target specific products during chemical and electrochemical reactions. [5,6]

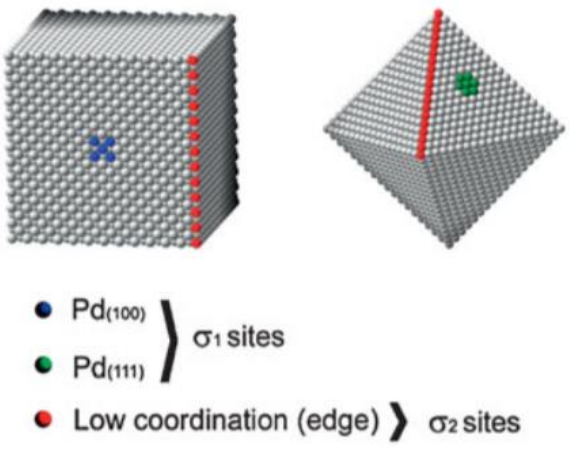

Figure 1.4 The effect of shape control. (a) Schematic of the two types of catalytically active sites (σ1 and σ2) presented on the surface of Pd nanocrystals. [5]

Another parameter to take in consideration in the synthesis of nanocatalyst is the stability of nanomaterials. To approach this common problematic in nanoparticles as an example, different stabilizing agents have been employed to help with the stability factor. Polymers, surfactants, capping agents, and ligands are considered as the stabilizing agents for nanomaterials. Stabilizing agents are not only used to protect the material, but they are also proved to play a major role controlling morphology, size and surface chemistry (steric and/or electronic modifications). Thus, they are also used as options to tune the properties of the material towards higher activity and selectivity. However, the addition of these molecules could also lead to a blockage of active sites at the surface of the catalyst, therefore, its optimization is of great importance during the synthesis of the nanocatalyst having a major role in their crystal size, structure, and surface composition.

Therefore, different methods can be employed to tune the properties of a nanocatalyst as: a) size of nanomaterial, b) composition (intrinsic composition and surface state), c) crystal structure, d) morphologies/shape, e) use of stabilizing agents as surfactants, ligands or polymers.

1.2.1. Bimetallic nanocatalysts, synergetic effect and applications

Bimetallic nanomaterials offer a variety of properties as magnetic, optical, electrical and in catalysis due to a synergetic effect attributed to the combination of different metals forming the nanostructures. In addition, their bimetallic structure as core-shell or solid solution influences directly in their chemical and physical properties due to the ability of control the electron transfer between metals and surface strain effects.[7] Thus, it is not surprising that they performance better than monometallic materials.

Moreover, bimetallic synthesis of nanomaterials also allows for a better control over the tuning of properties of the nanocatalyst. For instance, bimetallic nanostructures as core-shell, heterostructure, intermetallic or alloy structures can be used in surface engineering technique to tune and control the properties. As it was stablished, their properties at not only expected to be a combination of two independent properties but instead a synergistic effect is anticipated between two metals. However, compared with monometallic structures, bimetallic synthesis is more challenge to achieve but at the same time more interesting to observe.[1]

In the following section, we will be reviewing the applications for bimetallic catalytic structure as in chemical reaction for industry, effects on hydrogen storage, and catalysts for renewable energies as hydrogen as a fuel.

1.2.2. Nanocatalyst for fine chemicals synthesis and its applications

Fine chemicals and its intermediate products are of great value for laboratory and commercial procedures as in pharmaceutical, agrochemical, additives and food industry to mention a few. However, their procedures involves the use of oxidants with high toxicity to the environment.[8,9] Thus, it is imperative to find new resources that makes those process more efficient, with low waste, and that produce lower environmental impact.

Among all the chemical reactions used in industry, oxidation of alcohols to aldehydes are crucial process for the synthesis of fine chemicals. Nevertheless, catalysts that selective transform alcohols to aldehydes are hard to found because most of them are inactive to certain alcohols as

alkyl group.[8] Therefore, development of greener heterogeneous catalysts that help to the oxidation of these alcohols either by using oxygen (O_2) or hydrogen peroxide (H_2O_2) are the scope of this research.[10] In these context, benzyl alcohol oxidation reaction has been widely used as a reference reaction because of their results in the production of fine chemicals, additives and more. Moreover, benzyl alcohol is a popular molecule due to its high reactivity and limited number of intermediates products (as benzaldehyde, a non-enolizable structure) which later are oxidized to acids as it is indicated in the Figure 1.5. [11,12]

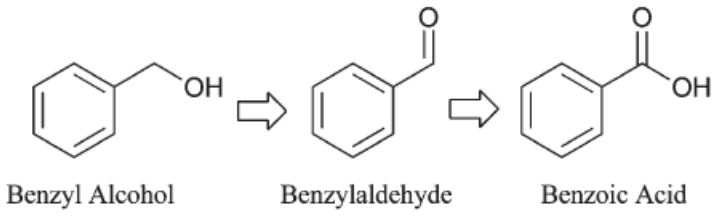

Figure 1.5 Reaction scheme for benzyl alcohol oxidation.[12]

Noble metals as platinum, palladium, gold and their respective alloys are popularly employed in alcohol oxidation reactions.[13] Most of the time, these noble metals are combined with non-noble metal from the transition group to reduce costs and obtain a synergistic effect of their catalytic properties. Other alternatives to boost their properties at low cost is involving the use of substrates as carbon, Al_2O_3, SiO_2, and SiO_2–Al_2O_3 mixed oxide.[12] For instance, Au-Ni bimetallic nanoparticles has been employed as an efficient catalyst for gas-phase selective oxidation of alcohols where the incorporation of Ni atoms significantly speed up the oxygen activation on gold nanoparticles, leading to a high selective in many alcohols oxidation reactions (Figure 1.6).[14]

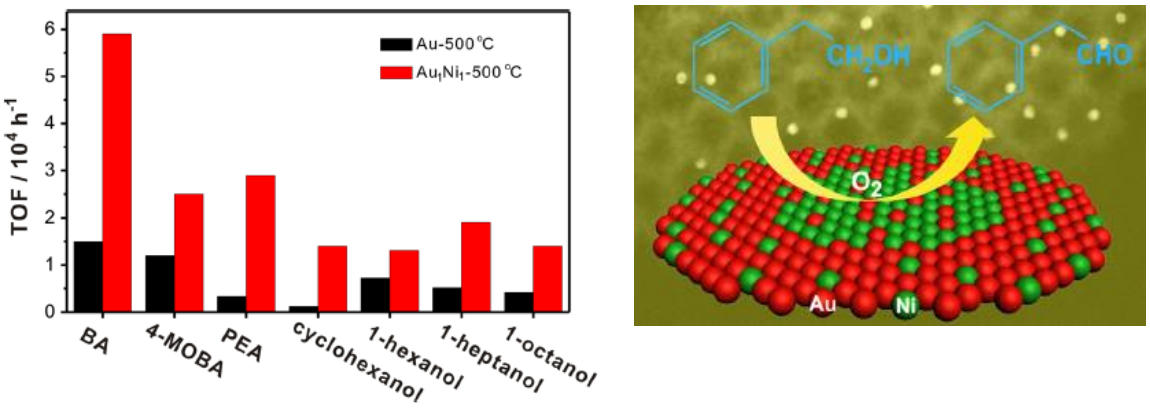

Figure 1.6 Catalytic performance over Au and Au1Ni1 in oxidations of a variety of alcohols, next diagram of the alcohol reaction to aldehydes on catalyst surface.[14]

1.2.3. Nanocatalyst for energy applications

The global increase in energetic consumption plus the environmental pollution associated with their main energetic source (fossil fuels) generates a call for actions towards the development of innovative and cleaner energy sources for the future. At the forefront of renewable energy technology development lies storage systems, water splitting and fuel cells, being the pivot for the success of this technology the development of highly efficient catalysts and electrocatalysts to improve processes as energy-fuel storage, and electrochemical reactions as hydrogen evolution reaction (HER), oxygen reduction reaction (ORR) and oxygen evolution reaction (OER).[15,16] Figure 1.7 exhibits an integrated system of sustainable energies without adding any carbon dioxide (CO_2) to the atmosphere.

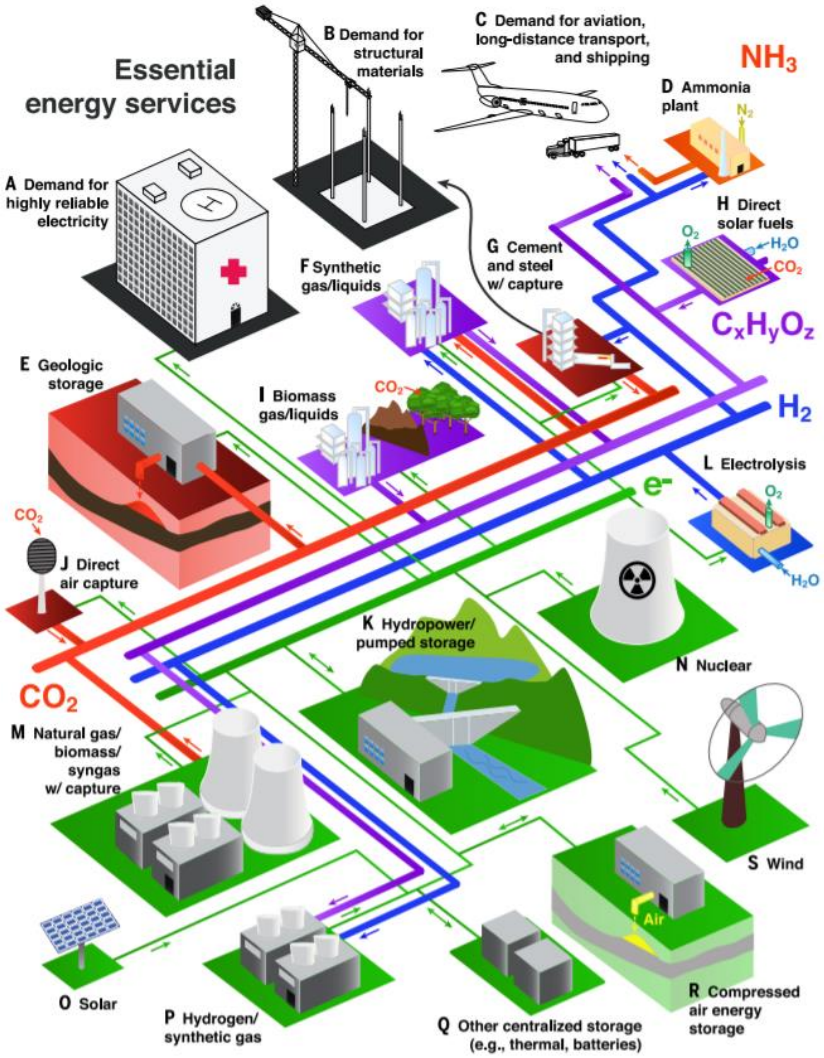

Figure 1.7 Schematic of an integrated system that can provide essential energy services without adding any CO2 to the atmosphere. (A to S) Colors indicate the dominant role of specific technologies and processes. Green, electricity generation and transmission; blue, hydrogen production and transport; purple, hydrocarbon production and transport; orange, ammonia production and transport; red, carbon management; and black, end uses of energy and materials.[16]

From all the energy sources established on Figure 1.7, we will be paying attention to Hydrogen as the next sustainable fuel which unlike fossil fuels, it mainly produces water as a

product. Hydrogen is considered one of the most promising energetic sources to overcome the carbon-based global demand due to its high energy content per unit of weight (120-143MJ/kg, or 30-40kWh/kg) which is much higher if compared to gasoline fuels (46.4MJ/Kg).[2,16]

However, there is still much to be solved in relation to the use of hydrogen as a green energy. For instance, hydrogen at a concentration of 4% or higher becomes highly flammable, and its storage and purity is also a matter of study. In addition, the production of hydrogen by water splitting, and it use as a fuel in fuel cells devices need the development of durable and active catalysts. This is illustrated in the next Figure 1.8.

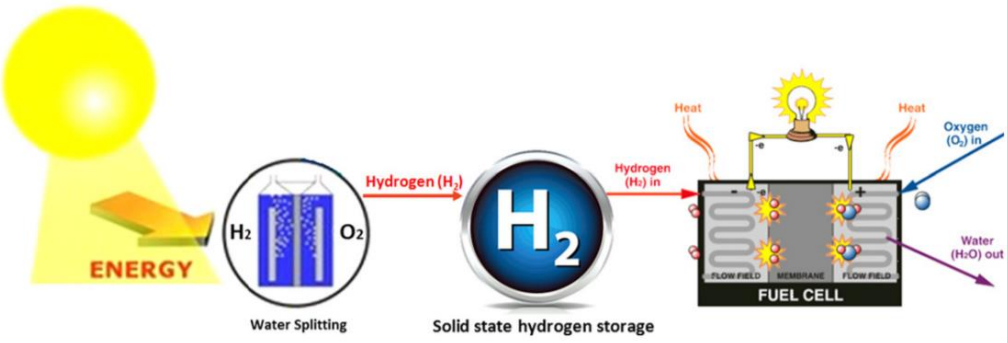

Figure 1.8 A scheme of renewable energy (e.g., hydrogen) based economy based on some selected technologies of renewable energy conversion and utilization.[17]

Consequently, the scope of the following research is associated with the development of highly active and efficient catalysts for their use in water splitting, hydrogen storage, and fuel cell or in other words their use for H_2 production, storage and delivery to boost greener energy technologies.

1.2.3.1. Hydrogen in palladium: storage, and its properties

The development of a safe and efficient system for hydrogen storage remains a challenge. Conventional liquid hydrogen is store in high pressure compressed gas cylinders. However, its low volumetric energy density makes it unsuitable for practical applications. For instance, in order to contain the same amount of energy as diesel, the system that contain liquid hydrogen would weight six times more and could be eight times larger than diesel systems (Figure 1.9).[1]

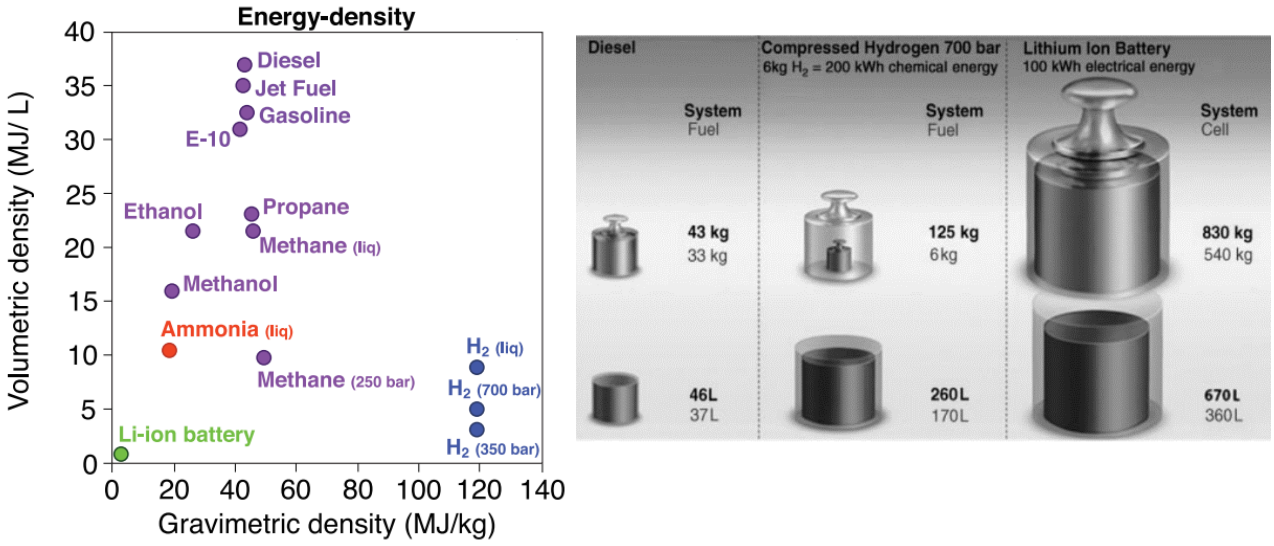

Figure 1.9 Comparisons of energy sources and technologies. A) The energy density of energy sources for transportation, including hydrocarbons (purple), ammonia (orange), hydrogen (blue), and current lithium ion batteries (green).[16] B) The weight and volume of various fuels and tank systems required for a 500 km range vehicle.[1]

Therefore, hydrogen system is a challenge but a necessary point of research. If we take as an example the automobile industry, two major renewable energy technologies are in competition: fuel cell based on hydrogen and Li-ion batteries. However, as it is illustrated in Figure 1.9, Li-ion

batteries exhibit poor energy content per unit weight and per unit volume. Thus, vehicles based on batteries are mostly suitable for small urban vehicles while cars based on hydrogen as a fuel can run much longer distances. Nevertheless, both technologies lack of sufficiently space for energy storage.[1]

Different strategies have been approached on the last decades for hydrogen storage known as physical and chemical-materials methods. The first type is referred to physically adsorption of hydrogen in its liquid or gas state without involving chemical bonds while material-based methods involves the storage of hydrogen by chemical bonding and dissociation of H_2 molecules at the surface of the material as in the case of metal hydrides.[1,18]

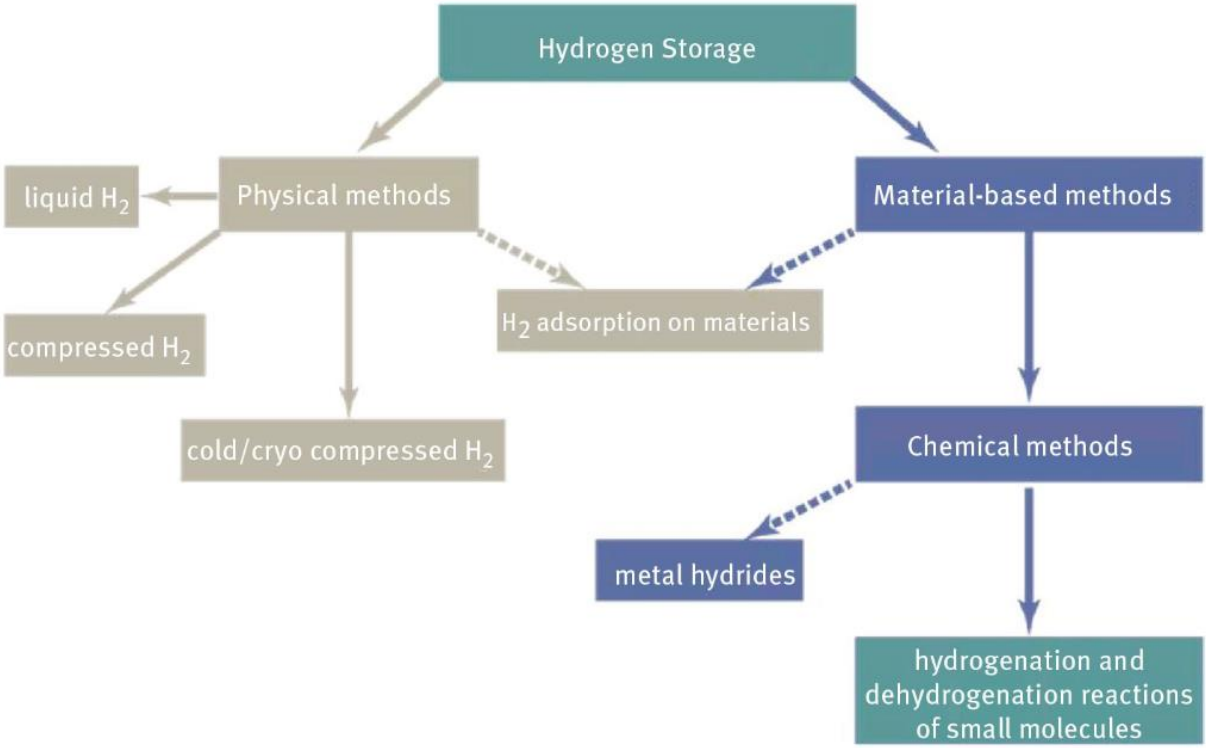

Figure 1.10 Methods for hydrogen storage.[18]

Besides compressed and liquid hydrogen storage in gas tanks with problems in terms of low volumetric density, other physical methods have been employed in the storage of hydrogen. Many porous materials as zeolites, carbon and metal organic frameworks (MOFs) which physically adsorb hydrogen on its porous structure have been employed, achieving high hydrogen storage. However, the storage of hydrogen into this structures are only possible under low temperatures and/or under high pressures due to a weak interaction between hydrogen and the host material.[7]

Thus, chemical methods based on transition metals as palladium which strongly interacts with hydrogen have gained attention because of their high density of states (DOS) at the Fermi level, giving an electronegativity value close to that of hydrogen. In addition, some metal hydrides have the ability to reversible absorb/desorb hydrogen at ambient temperature.[7]

Palladium is a well-known noble metal used mainly for hydrogen storage and as an effective catalyst. Palladium, with FCC structure, is estimated to absorb up to 900 times its own volume of hydrogen. More interesting, upon hydride formation the electronic states of palladium are affected directly giving rise to different properties than pure palladium.[19–21] For instance, palladium hydride with high hydrogen concentration ($x>1.0$) can exhibit superconductor properties, which is not observed in pure palladium since it performs as pure paramagnetic material. In addition, palladium hydride (Pd-H) storage and properties can also be tuned by alloying palladium to other transition metals as Ag, Au, Ru, Rh.[19] Therefore, Pd-H system is of great importance for fundamental studies and to advance in applications as hydrogen sensor, hydrogen storage, hydrogen purification, and fuel cells.

Palladium hydride presents phase transitions (Figure 1.11) upon increase of hydrogen concentration into the metal lattice known as α-phase at low hydrogen concentration ($x<0.01$) and β-phase rich in hydrogen ($x>0.7$), having also a co-existence of phases region α- β ($0.01<x<0.7$) in bulk palladium at temperatures below 298°C and pressures below 2MPa (above 298°C only α phase can exist).[5,22,23]

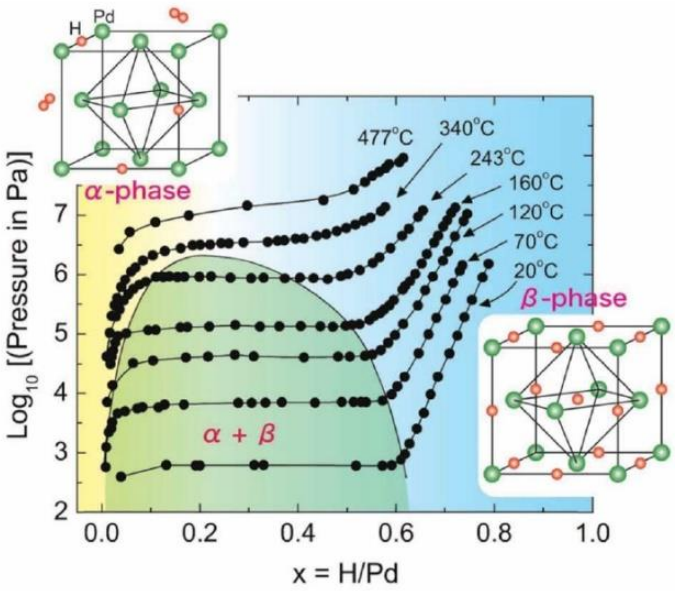

Figure 1.11 Pressure-composition isotherms (PCT) curves of bulk Pd-H on desorption process. H/Pd is the number of absorbed H atoms per Pd atom.[7]

Palladium hydride formation starts when the hydrogen molecule gets in contact with the surface of the metal as palladium where dissociation into hydrogen atoms take place. The hydrogen atoms are then rapidly absorbed and diffused into its lattice. Neutron diffraction studies have proved that at ambient temperature and H_2 pressure, hydrogen atoms randomly occupy the octahedral interstices in the FCC lattice where it can be found one octahedral hole per palladium atom (Figure 1.12).[24] However, at high pressures or high temperatures, tetrahedral sites are found

partially occupied. [24] Due to absorption of hydrogen into palladium, a lattice expansion is observed. The increase of the lattice is generally studied by powder X-ray diffraction (PXRD) technique where it is determined that the lattice parameter increases linearly with the increase of hydrogen concentration.[25]

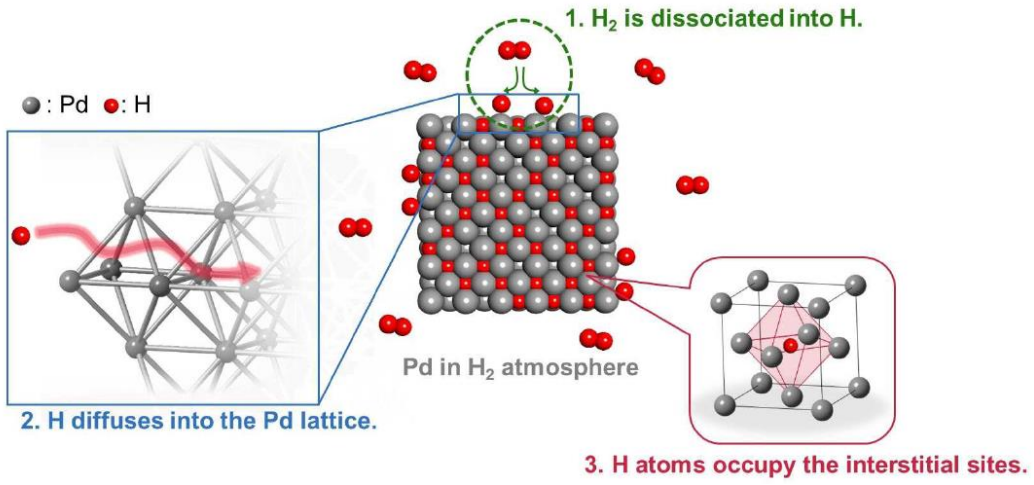

Figure 1.12 Schematic illustration of the hydrogen sorption process in the bulk Pd-H system.[7]

Despite of the findings on bulk materials, nanomaterials behave in a different way. In fact, palladium nanocrystals materials undergo abruptly to α-phase or β-phase, being the coexistence of faces almost null at nanosizes.[5] Moreover, morphology of nanoparticles plays a major role in the formation of palladium hydride with high hydrogen content, known as β-palladium hydride phase. In fact, studies have proved that different shapes present a critical role in the formation of β-PdHx at different ratios, and also affecting the capacity to store hydrogen.[5,20,21,26–28] Li et al. have demonstrated that palladium nanoparticles with octahedrons and cubes morphologies play a role in its uptake, absorption, and diffusion.

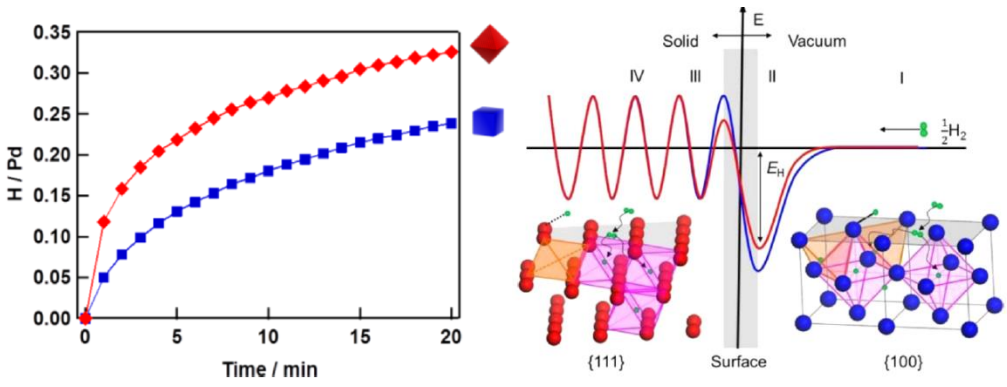

Figure 1.13 (a) Isothermal hydrogenation profiles of Pd octahedrons (red) and cubes (blue) at 303K after introducing hydrogen pressure of 101.3 kPa. (b) Schematic potential energy diagrams of the Pd octahedrons {111}/H (red) and the cubes {100}/H (blue) systems.

Based on the collected information, there is still much debate about the optimal morphology for palladium hydride formation because absorption and desorption should both be fast enough. For instance, different studies has proved a higher hydrogen content in octahedral morphologies.[27] However, nanocubes are found to have a faster transformation upon hydrogen absorption because of higher number of vertices than octahedral shapes which at the end accelerates the rate of β -phase nucleation. In the same manner, the desorption has reported much faster in (100) facets than (111) facets (Figure 1.14).[5,27]

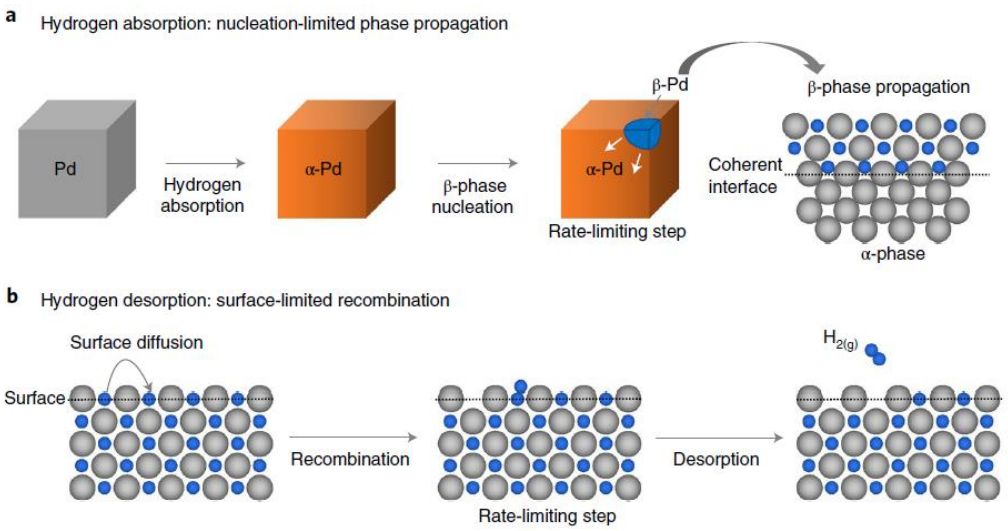

Figure 1.14 Hydrogen absorption and desorption in palladium nanocrystals. **a**, Schematic representation of the phase transformations that occur in a single cubic nanocrystal as hydrogen is absorbed. The facile formation of the α-phase precedes the rate-limiting nucleation of the β-phase at a vertex and then propagates coherently through the nanocrystal. **b**, Schematic representation of the surface-limited recombination process for hydrogen desorption. Surface hydrogen atoms diffuse from one neighboring site to another to mediate recombination prior to desorption as $H_2(g)$. Subsurface hydrogen then diffuses to the surface to maintain further hydrogen recombination. The surface-recombination step is rate limiting and dependent on the diffusion barrier from one occupied hydrogen site to another.[5]

Nevertheless of these findings, most of the recent studies are focused on in-situ monitoring studies being a lack of studies for direct chemical synthesis. Thus, there is still room for research in terms of palladium hydride system, and an urgent necessity for the development of stable β-palladium hydride with controllable shapes, and at different ratios Pd:Hx to tune its properties, obtaining a better understanding of its mechanism.

1.2.3.2. Electrocatalysts and their use in water splitting and fuel cells applications

Recently, research focused on nanomaterials for electrocatalyst had led to important discoveries and understanding in terms of controlled growth and fundamental principles of catalysis, maturing a path towards rational catalyst design.[29–31] For instance, surface engineering and/or induction of tensile/compressive strain at the surface of the nanomaterials have been used as key strategies to boost the catalytic properties of the materials in electrochemical reactions, allowing them to modulate the electronic structure at the surface and the corresponding energies of intermediates compounds of the reactions.[29,31,32]

Electrochemical reactions such as oxygen reduction reaction (ORR), oxygen evolution reaction (OER), and hydrogen evolution reaction (HER) are widely studied as the principal reactions to target in order to improve the process of hydrogen generation in water splitting systems and energy in fuel cells systems.

HER is the cathodic reaction in electrochemical water splitting in which catalysts are proved necessary to improve the kinetics of the reaction for the effective generation of hydrogen at low overpotential and with high faradaic efficiency.[33,34] On the other hand, fuel cells are devices that uses hydrogen or hydrogen rich fuel (e.g. methanol, formic acid) and oxygen to create electricity. When hydrogen is employed as a fuel, the fuel cell only produces vapor water and heat as byproducts, thus, eliminating the generation of pollutants. In the same way as in the electrolyzers, fuel cells devices also require catalyst materials for the reaction to happen effectively. The reactions associated with both devices are discussed deeply on chapter 4. The next Figure 1.15 illustrates a normal electrolyzer and fuel cell devices.

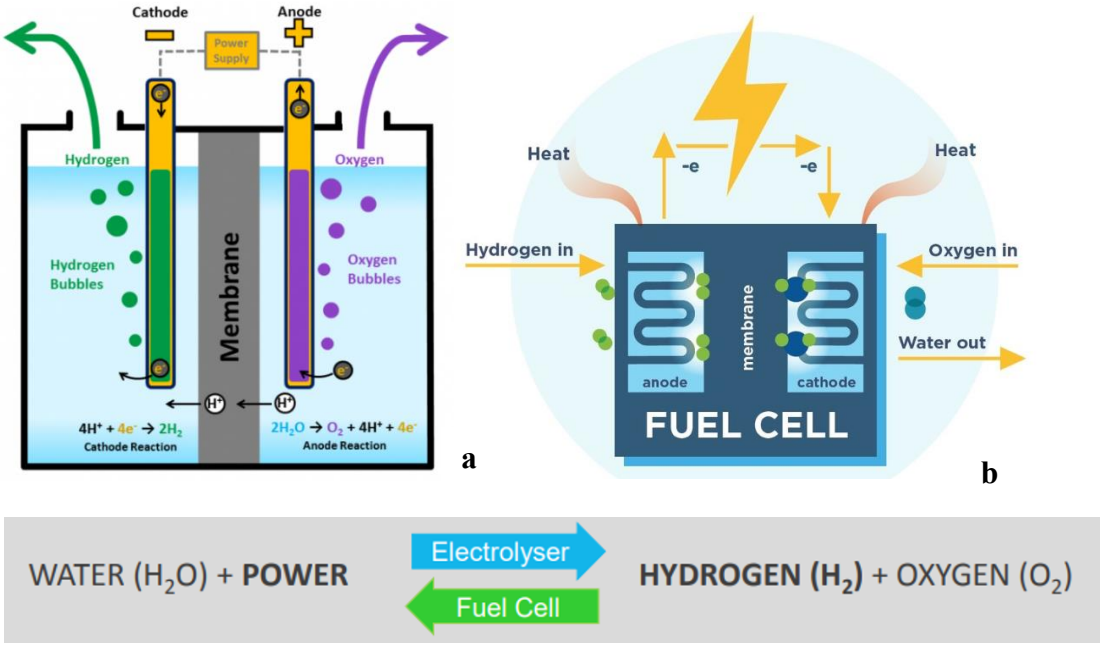

Figure 1.15 a) Electrolyzer representation[35] and b) Fuel cell device[36]

Other forms to storage hydrogen have also been studied as in the case of organic molecules. Formic acid, for instance, is studied as a safer option for hydrogen storage and fuel source because of its low flammability and low toxicity under ambient conditions. Besides, gasoline infrastructure could be potentially adapted to formic acid distribution. In addition, the low storage capacity of formic acid (around 4.4 wt%) is overcome by its high density, reaching a volumetric capacity of around 53 g H_2/L. Moreover, formic acid as hydrogen storage present an advantage over some chemical hydride structures in terms of reversibility which is found to be lower in metal hydrides even though of their high gravimetric hydrogen storage (around 20%).[2] To clarify these numbers for real applications, it is determined that the volumetric capacity of formic acid seems equivalent to an energy density of about 1.77 KWh/L which is higher than the technology used in the Toyota Mirai (e.g. 1.4 KWh/L).[2]

Formic acid oxidation reaction is the anodic reaction in direct formic acid fuel cells (DFACFC). In this system, the organic molecule is dissociated at the surface of the electrocatalyst followed by an oxidation process to obtain carbon dioxide and hydrogen as the byproducts. Hydrogen will be used as the energy to the system, and the carbon dioxide can be used to produce formic acid, therefore closing the cycle.[37,38]

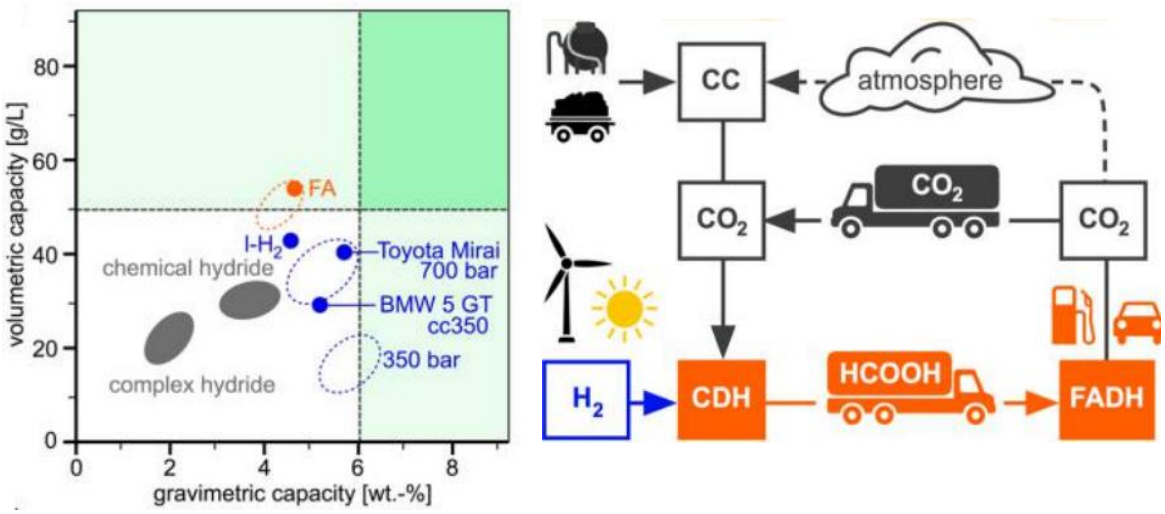

Figure 1.16 Case for FA as a hydrogen carrier. (A) FA competes well with other reversible hydrogen storage options. (B) FA as a H_2 carrier for the transport sector. 8 CDH: carbon dioxide hydrogenation; FADH: FA dehydrogenation.[2]

Although hydrogen introduce a new set of greener options as an energy source for the future, still much have to be done in terms of catalysts. Nanocatalysts need to be prepared to support extreme conditions (e.g. acidic and alkaline environments, multiple cycling), meaning that they need to be robust, and at the same time exhibit high catalytic activity and at a low cost to be

practically viable. Nobel metals and its alloy are known for effectively catalyzed the reactions of the systems mentioned before. At the nanocatalyst layer, many processes take place as mass transport, interfacial reactions at the active sites of the electrocatalyst, proton transfer in the electrolyte media, and electron conduction in the electronic phase.[1] For instance, anodic (oxidation reaction) and cathodic (oxygen reduction) reactions require catalytic active sites to dissociate the molecules to their respective ions and free the electrons to produce energy. Platinum and platinum group has been used for decades as nanocatalysts for these applications. In fact, the state-of-art for electrochemical reaction is based on Pt. However, several disadvantages are associated in Pt catalysts as slow kinetics, low efficiency and lifetime, high cost and low percentage abundance.

Palladium and its alloy on the other hand, make a more attractive choice for electrocatalytic reactions because they exhibit higher catalytic activity and higher abundancy than pure Pt. In addition, palladium based materials show low carbon monoxide (CO) poisoning effect, a problematic found in Pt based materials. [37,39–46] Furthermore, addition of non-noble metals as transition metals (e.g. Ni, Cu, Co, Ru, Fe) allow the formation bimetallic compounds with synergetic effects which make them much approachable nanocatalyst candidates with high activities and at a lower cost.

For instance, Wang and co-workers have successfully synthesized two-dimensional palladium nanosheets which exhibited surface strain at the surface, thus tailoring the reactivity of the metal catalysts for two important reactions as HER and ORR. Researchers were able to have an atomic control of the thickness of palladium nanosheets, and they were also able to introduce intrinsic strain that overall enhanced the catalytic activity up to more than an order of magnitude if compared with nanoparticle counterparts.[29]

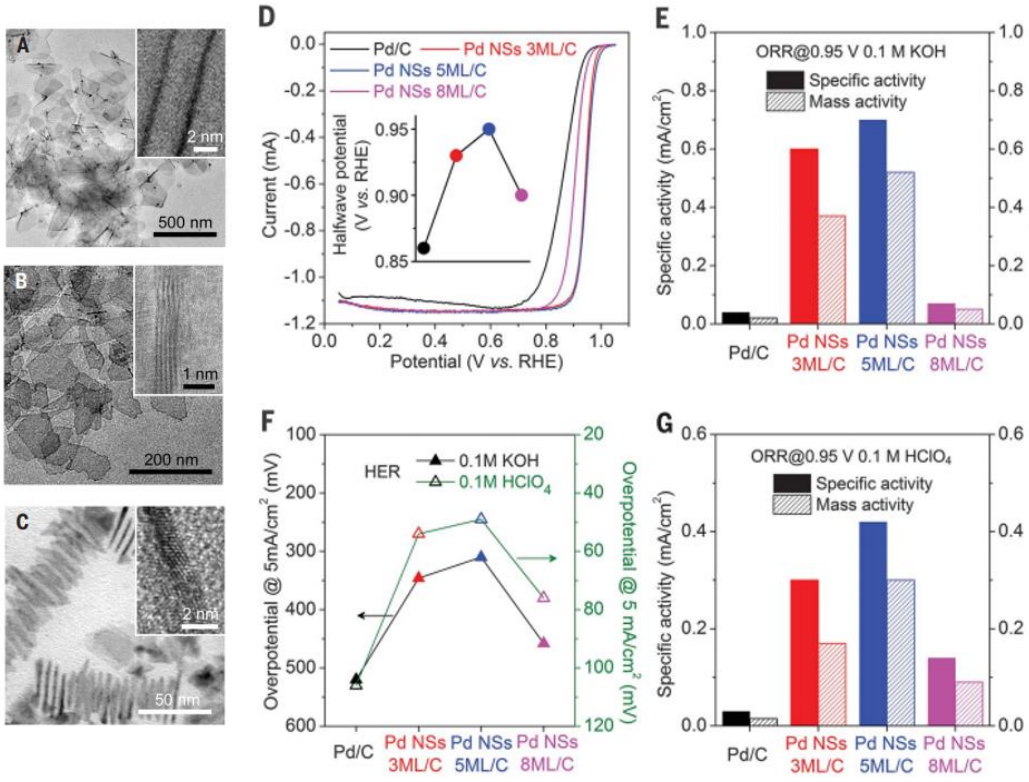

Figure 1.17 Structural characterization of Pd nanosheets. (A to C) TEM images of as-prepared Pd nanosheets (NSs) with average thicknesses of 3 ML (A), 5 ML (B), and 8 ML (C), with insets depicting typical structures. (D-G) Electrochemical activity of Pd nanosheet catalysts on carbon. (D) ORR polarization curves of Pd nanoparticles, as well as Pd nanosheets with average thickness of 3 ML, 5 ML, and 8 ML in 0.1 M KOH (inset shows the halfwave potential). RHE, reversible hydrogen electrode. (E) Specific activity and mass activity of ORR at 0.95 V (versus RHE) in 0.1 M KOH. (F) HER overpotential of Pd nanoparticles, as well as Pd nanosheets with average thickness of 3 ML, 5 ML, and 8 ML at 5 mA/cm2 in 0.1 M KOH or 0.1 M $HClO_4$. (G) Specific activity and mass activity of ORR at 0.95 V (versus RHE) in 0.1 M $HClO_4$.

Besides monometallic (pure metal) and bimetallic (combination of two different metals) alloys, other compounds as intermetallic nanoparticles have gained great attention around researchers.

Alloy compounds are better known for their disordered structure in which atoms of a bimetallic compound are distributed randomly. As a result, alloy materials present catalytic limitations because their active sites are not found identical structured. Some of the problems associated to alloys are in terms of particle growth which affects directly the stability and durability, besides dissolution of transition metals can happen decreasing the activity of the material. On the other hand, atomically ordered phases as intermetallic compounds have a inimitable geometrical ordered structure in which effects as lattice strain at the surface could potentially cause a shift in the d-band center of the material which cause a change in the electronic effects of the nanocatalyst, and therefore their activity and stability are found to increase if compared with their alloy counterparts.[47] Nonetheless, synthesis remain a major challenge because their intermetallic-ordered structure is highly depended on conditions as atomic concentration ratio and temperature.

For instance, Sun and co-workers have been able to stabilize iron (Fe) in an intermetallic core/shell structure of $L1_0$-FePt/Pt which is surrounded by two atomic layers of Pt shell. The mentioned intermetallic structure allowed the protection of Fe against etching process during ORR measurements due to presence of layers of Pt shell. The sum of all these features resulted in a superior mass activity, better durability, and overall higher efficiency in their catalytic properties which make them suitable for fuel cell applications.[48] Other intermetallic approaches can be found

in the literature as in the case of intermetallic PdCu nanoparticles that showed practical purposes in ORR as well. Skrabalak and co-workers were able to transform PdCu nanoparticles with disordered phase into an ordered phase by using a seed-mediated co-reduction method. In the same manner, the synthesize intermetallic B2-PdCu nanoparticles showed superior activity and durability for ORR in comparison with their alloy A1-PdCu phase, opening a door for Pd-based intermetallic nanocatalyst to substitute Pt-based catalyst for fuel cell applications.[49]

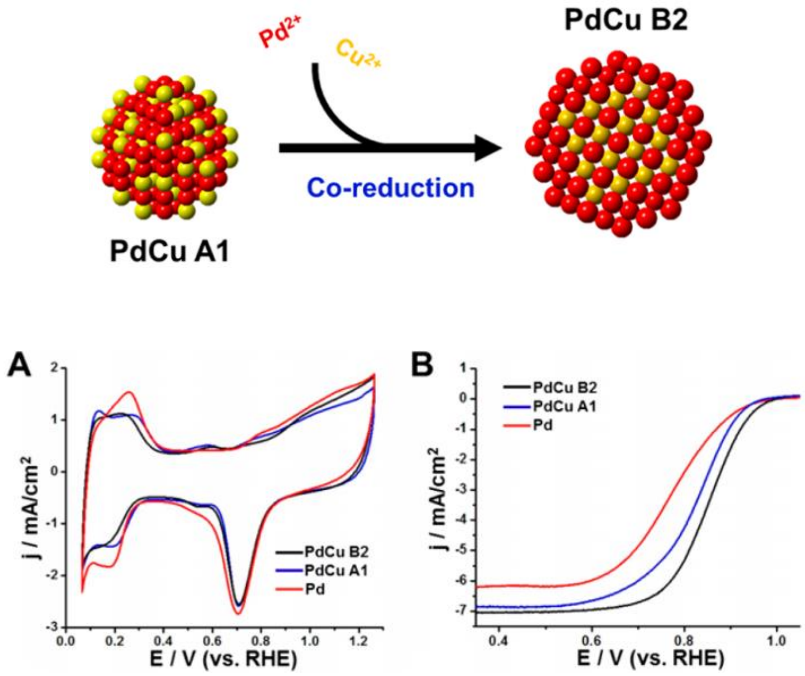

Figure 1.18 (A) CVs recorded at room temperature in Ar-saturated 0.1 M HClO4 solution with a sweep rate of 50 mV s−1; (B) ORR polarization curves recorded at room temperature in O2-saturated 0.1 M HClO4 aqueous solution with a sweep rate of 10 mV s−1 and a rotation rate of 1600 rpm.[49]

In particular, the use of bimetallic alloys and intermetallic nanomaterials in electrolyzers and fuel cells are significantly enhancing the catalytic performance of the electrochemical reactions while reducing manufacturing costs. Nonetheless, there is still much more to be understood in terms of size, shape, structure and surface defects to mention a few. Thus, nanoengineering approaches are in need to be implemented.

1.3 References

1. Serp, P.; Philippot, K. *Nanomaterials in Catalysis*; Serp, P., Philippot, K., Eds.; Wiley-VCH Verlag & Co. KGaA, **2013**.
2. Eppinger, J.; Huang, K. Formic Acid as a Hydrogen Energy Carrier. *ACS Energy Lett.* **2017**, No. 2, 188–195.
3. Bäumer, M.; Sonström, P. Supported Colloidal Nanoparticles in Heterogeneous Gas Phase Catalysis : On the Way to Tailored Catalysts. *Phys. Chem. Chem. Phys.* **2011**, No. 13, 19270–19284.
4. Owens, F. J.; Poole, C. P.; Wiley, A. J. *The Physics and Chemistry of Nanosolids*; Wiley-Interscience: Hoboken, New Jersey, **2008**.
5. Johnson, N. J. J.; Lam, B.; Macleod, B. P.; Sherbo, R. S.; Moreno-gonzalez, M.; Fork, D. K.; Berlinguette, C. P. Facets and Vertices Regulate Hydrogen Uptake and Release in Palladium Nanocrystals. *Nat. Mater.* **2019**, *2*.
6. Ruditskiy, A.; Choi, S.; Peng, H.; Xia, Y. Shape-Controlled Metal Nanocrystals for Catalytic Applications. *MRS Bull.* **2014**, *39* (8), 727–737.
7. Dekura, S.; Kobayashi, H.; Kusada, K.; Kitagawa, H. Hydrogen in Palladium and Storage Properties of Related Nanomaterials : Size , Shape , Alloying , and Metal-Organic Framework Coating Effects. *ChemPhysChem* **2019**, No. 20, 1–20.
8. Enache, D. I. Solvent-Free Oxidation of Primary Alcohols to Aldehydes Using Au-Pd/TiO2 Catalysts. *Science (80-.).* **2006**, *311* (5759), 362–365.
9. Ciriminna, R.; Pandarus, V.; Xu, Y.; Pagliaro, M. Heterogeneously Catalyzed Alcohol Oxidation for the Fine Chemical Industry. *Org. Process Res. Dev.* **2015**, No. 19, 1554–1558.

10. Hazen, R. M.; Finger, L. W.; Castex, J.; Peyronneau, J.; Ringwood, A. E.; Suzuki, T.; Akaogi, M.; Sharp, T. G.; Goresy, A. El; Wopenka, B.; et al. Green , Catalytic Oxidation of Alcohols in Water. **2000**, *287* (March), 1636–1640.
11. Gligorich, K. M.; Sigman, M. S.; Sigman, M. Recent Advancements and Challenges of Palladium II -Catalyzed Oxidation Reactions with Molecular Oxygen as the Sole Oxidant. *ChemComm* **2009**, 3854–3867.
12. Davis, R. J.; Davis, S. E.; Ide, M. S.; Davis, R. J. Selective Oxidation of Alcohols and Aldehydes over Supported Metal Nanoparticles. *Green Chem.* **2013**, *15* (1), 17–45.
13. Galvanin, F.; Sankar, M.; Cattaneo, S.; Bethell, D.; Dua, V.; Hutchings, G. J.; Gavriilidis, A. On the Development of Kinetic Models for Solvent-Free Benzyl Alcohol Oxidation over a Gold-Palladium Catalyst. *Chem. Eng. J.* **2018**, *342*, 196–210.
14. Yi, W.; Yuan, W.; Meng, Y.; Zou, S.; Zhou, Y.; Hong, W.; Che, J.; Hao, M.; Ye, B.; Xiao, L.; et al. A Rational Solid-State Synthesis of Supported Au-Ni Bimetallic Nanoparticles with Enhanced Activity for Gas-Phase Selective Oxidation of Alcohols. *ACS Appl. Mater. Interfaces* **2017**, *9* (37), 31853–31860.
15. Park, J.; Kwon, T.; Kim, J.; Jin, H.; Kim, H. Y.; Kim, B.; Joo, S. H.; Lee, K. Hollow Nanoparticles as Emerging Electrocatalysts for Renewable Energy Conversion Reactions. *Chem. Soc. Rev.* **2018**, No. 47, 8173–8202.
16. Davis, S. J.; Lewis, N. S.; Shaner, M.; Aggarwal, S.; Arent, D.; Azevedo, I. L.; Benson, S. M.; Bradley, T.; Brouwer, J.; Chiang, Y.; et al. Net-Zero Emissions Energy Systems. *Science (80-.).* **2018**, No. 360, 1–9.
17. Mao, S. S.; Shen, S.; Guo, L. Nanomaterials for Renewable Hydrogen Production , Storage and Utilization. *Prog. Nat. Sci. Mater. Int.* **2012**, *22* (6), 522–534.

18. Zell, T.; Langer, R. *Hydrogen Storage: Based on Hydrogenation and Dehydrogenation Reactions of Small Molecules*; Zell, T., Langer, R., Eds.; De Gruyter: Berlin/Boston, **2019**.
19. Fujii, K.; Ishimatsu, N.; Maruyama, H.; Shishidou, T.; Hayakawa, S.; Kawamura, N. Relationship between Element-Selective Electronic States and Hydrogen Absorption Properties of Pd- M (M = Ru , Rh , Ag , and Au) Alloys. *Phys. Rev. B* **2017**, No. 95, 024116(1)-024116(7).
20. Lu, Y.; Wang, J.; Peng, Y.; Fisher, A.; Wang, X. Highly Efficient and Durable Pd Hydride Nanocubes Embedded in 2D Amorphous NiB Nanosheets for Oxygen Reduction Reaction. *Adv. Energy Mater.* **2017**, *7* (21), 1–7.
21. Chen, Y.; Sakata, O.; Nanba, Y.; Singgappulige, L.; Kumara, R.; Yang, A.; Song, C.; Koyama, M.; Li, G.; Kobayashi, H.; et al. Electronic Origin of Hydrogen Storage in MOF-Covered Palladium Nanocubes Investigated by Synchrotron X-Rays. *Commun. Chem.* **2018**, *61*, 1–8.
22. Soldatov, A. V.; Della Longa, S.; Bianconi, A. Relevant Role of Hydrogen Atoms in the XANES of Pd Hydride: Evidence of Hydrogen Induced Unoccupied States. *Solid State Commun.* **1993**, *85* (10), 863–868.
23. Lewis, F. A. *The Palladium/Hydrogen System*; Academic Press: New York, 1967.
24. Akiba, H.; Kofu, M.; Kobayashi, H.; Kitagawa, H.; Ikeda, K.; Otomo, T.; Yamamuro, O. Nanometer-Size Effect on Hydrogen Sites in Palladium Lattice. *J. Am. Chem. Soc.* **2016**, *138* (32), 10238–10243.
25. Zhao, Z.; Huang, X.; Li, M.; Wang, G.; Lee, C.; Zhu, E.; Duan, X.; Huang, Y. Synthesis of Stable Shape-Controlled Catalytically Active β-Palladium Hydride. *J. Am. Chem. Soc.* **2015**, *137* (50), 15672–15675.
26. Li, G.; Kobayashi, H.; Dekura, S.; Ikeda, R.; Kubota, Y.; Kato, K.; Takata, M.; Yamamoto,

T.; Matsumura, S.; Kitagawa, H. Shape-Dependent Hydrogen-Storage Properties in Pd Nanocrystals: Which Does Hydrogen Prefer, Octahedron (111) or Cube (100)? *J. Am. Chem. Soc.* **2014**, No. 111, 10222–10225.

27. Zalineeva, A.; Baranton, S.; Coutanceau, C.; Jerkiewicz, G. Octahedral Palladium Nanoparticles as Excellent Hosts for Electrochemically Adsorbed and Absorbed Hydrogen. *Sci. Adv.* **2017**, *3*, 1–11.
28. Sytwu, K.; Hayee, F.; Narayan, T. C.; Koh, A. L.; Sinclair, R.; Dionne, J. A. Visualizing Facet-Dependent Hydrogenation Dynamics in Individual Palladium Nanoparticles. *Nano Lett.* **2018**, *18*, 5357–5363.
29. Wang, L.; Zeng, Z.; Gao, W.; Maxson, T.; Raciti, D.; Giroux, M.; Pan, X.; Wang, C.; Greeley, J. Tunable Intrinsic Strain in Two-Dimensional Transition Metal Electrocatalysts. *Science (80-.).* **2019**, No. 363, 870–874.
30. Coc, C. Ultralow-Loading Platinum-Cobalt Fuel Cell Catalysts Derived from Imidazolate Frameworks. *Science (80-.).* **2018**, *362*, 1276–1281.
31. Yao, Y.; Hu, S.; Chen, W.; Huang, Z.; Wei, W.; Yao, T.; Liu, R.; Zang, K.; Wang, X.; Wu, G.; et al. Engineering the Electronic Structure of Single Water Oxidation Electrocatalysis. *Nat. Catal.* **2019**, *2* (April), 304–313.
32. Zhao, Z.; Liu, H.; Gao, W.; Xue, W.; Liu, Z.; Huang, J.; Pan, X.; Huang, Y. Surface-Engineered PtNi-O Nanostructure with Record-High Performance for Electrocatalytic Hydrogen Evolution Reaction. *J. Am. Chem. Soc.* **2018**, *140*, 9046–9050.
33. Mahmood, J.; Li, F.; Jung, S.; Okyay, M. S.; Ahmad, I.; Kim, S.; Park, N.; Jeong, H. Y.; Baek, J. An Efficient and PH-Universal Ruthenium-Based Catalyst for the Hydrogen Evolution Reaction. *Nat. Nanotechnol.* **2017**, *12* (5), 441–446.

34. Cao, L.; Luo, Q.; Liu, W.; Lin, Y.; Liu, X.; Cao, Y.; Zhang, W.; Wu, Y.; Yang, J.; Yao, T.; et al. Identification of Single-Atom Active Sites in Carbon-Based Cobalt Catalysts during Electrocatalytic Hydrogen Evolution. *Nat. Catal.* **2019**, *2*, 134–141.
35. Office of Energy Efficiency and Renewable Energy. Hydrogen Production: Electrolysis https://www.energy.gov/eere/fuelcells/hydrogen-production-electrolysis.
36. Association, F. C. and H. E. Fuel Cell Basics http://www.fchea.org/fuelcells.
37. Mazumder, V.; Chi, M.; Mankin, M. N.; Liu, Y.; Metin, Ö.; Sun, D.; More, K. L.; Sun, S. A Facile Synthesis of MPd (M = Co, Cu) Nanoparticles and Their Catalysis for Formic Acid Oxidation. *Nano Lett.* **2012**, *12* (2), 1102–1106.
38. Gunji, T.; Noh, S. H.; Tanabe, T.; Han, B.; Nien, C. Y.; Ohsaka, T.; Matsumoto, F. Enhanced Electrocatalytic Activity of Carbon-Supported Ordered Intermetallic Palladium − Lead (Pd 3 Pb) Nanoparticles toward Electrooxidation of Formic Acid. *Chem. Mater.* **2017**, *29*, 2906–2913.
39. Zalineeva, A.; Baranton, S.; Coutanceau, C.; Jerkiewicz, G. Octahedral Palladium Nanoparticles as Excellent Hosts for Electrochemically Adsorbed and Absorbed Hydrogen. **2017**, 1–11.
40. Wu, D.; Xu, H.; Cao, D.; Fisher, A.; Gao, Y.; Cheng, D. PdCu Alloy Nanoparticle-Decorated Copper Nanotubes as Enhanced Electrocatalysts : DFT Prediction Validated by Experiment. *Nanotechnology* **2016**, *27*.
41. Li, J.; Li, F.; Guo, S.; Zhang, J.; Ma, J. PdCu @ Pd Nanocube with Pt-like Activity for Hydrogen Evolution Reaction. *ACS Appl. Mater. Interfaces* **2017**, *9*.
42. Wen, C.; Wei, Y.; Tang, Di.; Sa, B.; Zhang, T.; Chen, C. Improving the Electrocatalytic Properties of Pd-Based Catalyst for Direct Alcohol Fuel Cells: Effect of Solid Solution. *Sci.*

Rep. **2017**, *7* (1), 1–11.

43. Li, S.; Cheng, D.; Qiu, X.; Cao, D. Synthesis of Cu@Pd Core-Shell Nanowires with Enhanced Activity and Stability for Formic Acid Oxidation. *Electrochim. Acta* **2014**, *143*, 44–48.
44. C. Li, Q. Yuan, B. Ni, T. He, S. Zhang, Y. Long, L. Gu, X. W. Dendritic Defect-Rich Palladium-Copper-Cobalt Nanoalloys as Robust Multifunctional Non-Platinum Electrocatalysts for Fuel Cells. *Nat. Commun.* **2018**, *9* (3702), 1–9.
45. Bin, D.; Yang, B.; Ren, F.; Zhang, K.; Yang, P.; Du, Y. Facile Synthesis of PdNi Nanowire Networks Supported on Reduced Graphene Oxide with Enhanced Catalytic Performance for Formic Acid. *J. Mater. Chem. A* **2015**, *3*, 14001–14006.
46. Liu, Z.; Fu, G.; Li, J.; Liu, Z.; Xu, L.; Sun, D.; Tang, Y. Facile Synthesis Based on Novel Carbon-Supported Cyanogel of Structurally Ordered Pd3Fe / C as Electrocatalyst for Formic Acid Oxidation. *Nano Res.* **2018**, *11* (9), 4686–4696.
47. Xiao, W.; Lei, W.; Gong, M.; Xin, H. L.; Wang, D. Recent Advances of Structurally Ordered Intermetallic Nanoparticles for Electrocatalysis. *ACS Catal.* **2018**, *8* (4), 3237–3256.
48. Li, J.; Xi, Z.; Pan, Y.; Spendelow, J. S.; Duchesne, P. N.; Su, D.; Li, Q.; Yu, C.; Yin, Z.; Shen, B.; et al. Fe Stabilization by Intermetallic L10 - FePt and Pt Catalysis Enhancement in L10 - FePt/Pt Nanoparticles for Efficient Oxygen Reduction Reaction in Fuel Cells. **2018**, *140*, 2926–2932.
49. Wang, C.; Chen, D. P.; Sang, X.; Unocic, R. R.; Skrabalak, S. E. Size-Dependent Disorder-Order Transformation in the Synthesis of Monodisperse Intermetallic PdCu Nanocatalysts. *ACS Nano* **2016**, *10* (6), 6345–6353.

Chapter 2

2 Surface Controlled Catalysts with High Performance Towards Benzyl Alcohol Oxidation

2.1 Introduction

Noble metal nanostructures with controllable morphology possess multiple catalytic, electronic and optical properties which are indispensable for global industrial applications.[1-2] Among them, dendritic nanostructures, have been widely attracted due to their highly branched and hierarchical structure ensuing large surface areas and unique catalytic, electronic and magnetic properties.[3] As a result of their high catalytic activity, nanodendritic structures with different compositions have been extensively studied in multiple oxidation-reduction reactions such as electrocatalytic oxidation of alcohols[4-5] and oxidation of toxic compounds including benzene, toluene, and o-xylene in fuel.[6] Additionally, they have also been employed for oxygen-reduction reactions in fuel cells,[7] reduction of 4-nitrophenol.[8] Beside those reactions, the selective oxidation reaction of primary alcohols to aldehydes is highly important for research at a laboratory and industrial scale as aldehydes are widely used in pharmaceutical industry and perfume business.[9-11] Specifically, tuning selectivity towards benzaldehyde is of great interest as it acts as an intermediate in the production of fine chemicals, and additives for flavoring and fragrance.[12] However, most of industrial alcohol oxidation reactions employ toxic chemicals as chromate, permanganate or peroxide components.[13-14] Instead, other approaches like using pure oxygen as an oxidant in heterogeneous catalysis,[15] providing a more green chemical process for the

mentioned reaction. Enhancing the catalytic performance of noble metal nanocatalyst is critical for the environmentally friendly route of alcohol oxidation.

Palladium and palladium alloy catalysts have been found to be active for the oxidation of alcohols to their corresponding aldehydes and ketones.[12, 15-16] Additionally, palladium hydrides present remarkable performance in hydrogen storage, sensing,[17-19] and as a catalyst in multiple reactions. For instance, $PdH_{0.43}$ nanostructures have been employed as an anode for direct formic acid fuel cells, exhibiting higher mass activity at lower potentials than commercial Pd.[20] In the same way, $PdH_{0.43}$ nanocubes have shown enhanced selectivity of photocatalytic reduction of CO_2 into CH_4.[21] Oxygen reduction reaction (ORR) has also been tested using palladium hydride nanocubes embedded in NiB nanosheets, showing an activity five times higher than Pt catalysts.[22] On the other hand, nickel has also been extensively used as a catalyst. For instance, interfaces created between Ni and CeO_2 on CNT have shown superior catalytic activity for hydrogen evolution reaction (HER) in alkaline solution, closest to the performance of Pt.[23] Gold-nickel bimetallic nanoparticles have also demonstrated enhanced activity for gas phase selective oxidation of alcohols.[24] Moreover, low cost and high hydrogen oxidation reaction (HOR) performance have been achieved with Ni@h-BN core-shell catalyst due to active h-BN/Ni interfaces formation.[25] Likewise, Pd-Ni nanostructures have been studied to achieve catalysts with lower cost and high performance for different chemical reactions. Recently bimetallic Pd-Ni icosahedra nanostructure with core rich in palladium and nickel decorating the surface showed a dramatic improvement for ORR.[26] The Pd_6Ni icosahedra with Ni surface rich yielded higher ORR than those icosahedral structures with alloy surfaces or Pd-rich surfaces, proving that there is a unique and outstanding interaction between Pd core and Ni surface.[26] Other studies on Pd-Ni

bimetallic structures have also considered high catalytic activity due to their interaction, for instance, in alcohol oxidation reactions as ethanol and formic acid oxidation.[27-28] Hence, surface engineering techniques, like controlling surface facet,[1, 15] or tuning surface composition,[11, 29] can be a key for improving oxygen activation on palladium based nanoparticles which promotes selective oxidation of alcohol through a green chemistry route.

Here, we introduce an advanced yet straightforward set of steps to synthesize a new class of stable nanodendrites of palladium hydride ($PdH_{0.43}$) and nickel palladium hydride ($Ni/PdH_{0.43}$) with Ni tailored on the surface of $PdH_{0.43}$, exhibiting high selectivity towards the desired benzaldehyde in an advanced chemistry method. When compared to commercial Pd/C and $PdH_{0.43}$ compound, our synthesized $Ni/PdH_{0.43}$ dendrites show a dramatic improvement of their catalytic activity towards benzyl alcohol oxidation with high selectivity to benzaldehyde at high conversion rate demonstrating their potential use in new green routes for the synthesis of fine chemicals and organic intermediates.[11]

2.2 Results and Discussion

Palladium hydride ($PdH_{0.43}$) nanodendrites were first synthesized in one step method (for more details, see the Methods section). The material was then collected by centrifuge and washed several times with acetone/isopropanol mixture for further characterization (Figure 2.1). Scanning transmission electron microscopy (STEM) image (Figure 2.1A) and transmission electron microscopy (TEM) image of the as-synthesized $PdH_{0.43}$ material (Figure 2.1C bottom left insert) confirms the formation of uniform dendrites. Additionally, selected area electron diffraction

(SAED) pattern (Figure 2.1B) of the selected dendrite $PdH_{0.43}$ (Figure 2.1B top insert) shows clear concentric diffraction rings which can be indicated a face center cubic (fcc) crystalline structure. Further high resolution (HRTEM) images (Figure 2.1C) show an average {111} interplane distance of 0.231 nm, again consistent with an fcc structure with a lattice parameter of around 0.400 nm. Powder X-ray diffraction (XRD) (Figure 2.1D) pattern indicates an fcc structure with a lattice parameter of 0.3996 nm, consistent with SAED and HRTEM observations. HRTEM results and XRD pattern also indicate the formation of β-palladium hydride phase, corresponding to an H:Pd ratio of 0.43 as it was established in our earlier work,[30] and in accordance with previous literature.[31-34]

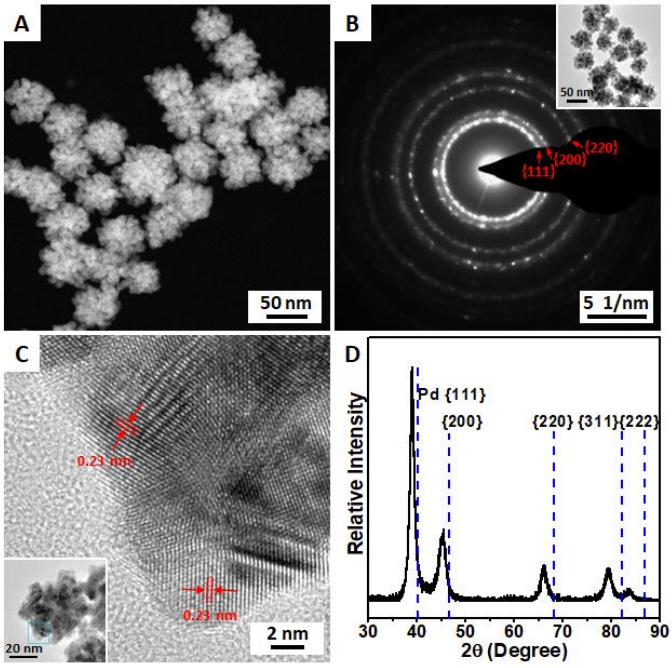

Figure 2. 1 (A) STEM of dendrite $PdH_{0.43}$, (B) SAED of dendrite $PdH_{0.43}$, insert: TEM of dendrite $PdH_{0.43}$ showing the area for SAED, (C)HRTEM of dendrite $PdH_{0.43}$, insert: zoom out image with blue rectangle showing where image was taken(D) powder XRD of dendrite $PdH_{0.43}$, blue perpendicular lines indicating the diffraction pattern position of Pd.

Meanwhile, time tracking studies (Figure 2.2A) suggest that specific modification of different contents of hydrogen can be achieved by controlling the reaction time. In fact, after only 15 min of reaction, palladium hydride formation begins. XRD spectrum of the product collected at this time indicates a lattice parameter of 0.3942 nm, corresponding to an H:Pd ratio of about 0.22. At 30 min of the reaction, the XRD pattern confirms a higher H:Pd ratio around 0.30 with a lattice parameter of 0.3962 nm, which is consisted with the XRD peaks shift to a lower angle. As the synthesis time increases, the H:Pd ratio increases as well as it is showed after 1 h where XRD peaks are shifted to even a lower angle with a lattice parameter of 0.3990 nm, corresponding to a H:Pd ratio around 0.41. After 2 hrs and 4 h, no significant shift of XRD peaks is observed, presenting a lattice parameter of 0.3996 nm and H:Pd ratio around 0.43 for both cases (Figure 2.2A, Table 2.1). The observed trend is consistent with our previous report.[30] In addition, the formation of $PdH_{0.43}$ phase is further confirmed by annealing test (Figure 2.2B). After annealing the material for 2 h at a temperature of 400 °C in the argon atmosphere, palladium hydride nanodendrites transform back to its original state of pure palladium (Pd) due to desorption of hydrogen, showing a lattice parameter of 0.3890 nm corresponding to the observed shift of XRD peaks (Figure 2.2B).

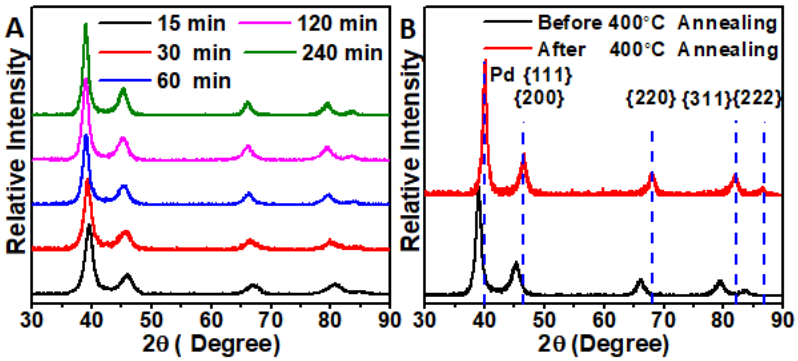

Figure 2.2 (A) powder XRD tracking of dendrite $PdH_{0.43}$ synthesis at different time points, (B) annealing dendrite $PdH_{0.43}$ in Ar at 400°C for 2 h showing powder XRD peaks shift from $PdH_{0.43}$ to palladium, blue perpendicular lines indicating the diffraction pattern position of Pd.

Table 2. 1 Reaction time related {111} peak positions and corresponded lattice parameters (extracted from XRD in Figure 2A)

Time Tracking	{111} Peak Position In 2θ (^{0})	Corresponding lattice parameter (nm)	Approximate composition
15 min	39.56	0.3942	H:Pd=0.22
30 min	39.36	0.3962	H:Pd=0.30
60 min	39.07	0.3990	H:Pd=0.41
120 min	39.01	0.3996	H:Pd=0.43
240 min	39.01	0.3996	H:Pd=0.43

Moreover, the synthesized nanodendrites are found to be highly branched stable structures (Figure 2.1A), and able to maintain composition and morphology when n-butylamine is introduced to the synthesis. In fact, our studies demonstrate that the lack of this primary amine results in the absence of dendritic morphology (Figure 2.3). TEM images (Figures 2.3A and 2.3C) of the synthesized materials without the primary amine showed a nanoflower-like shape instead without nanobranches. These observations are in agreement with previous studies where it was pointed out the importance of amine groups in their synthesis to develop stable nanostructures such as nanodendrites.[5, 35] In spite of their different morphology (with and without n-butylamine), the formation of β-palladium hydride phase is confirmed in both cases with SAED pattern (Figure 2.3B) which indicates an fcc packing structure with a lattice parameter around 0.400 nm which correspond to an H:Pd ratio of 0.43. HRTEM analysis of the same material (Figure 2.3C-D) also proves the formation of hydride compound showing a {111} interplane d-spacing of around 0.231 nm indicating an fcc structure with a lattice parameter around 0.400 nm. Our observations suggest that the formation of hydride is originated from the catalytic decomposition of DMF, forming in situ $PdH_{0.43}$ compound which transformation is independent of its morphology as established before.[30]

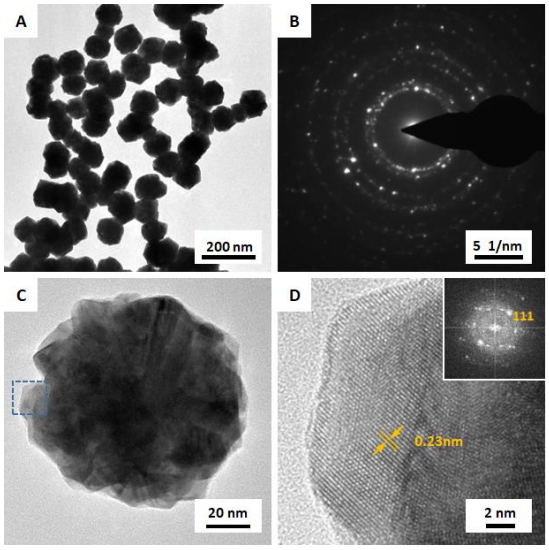

Figure 2.3 Control experiment without additional amine (A) TEM of $PdH_{0.43}$ nanoparticles obtained, (B) selected area electron diffraction (SAED) of $PdH_{0.43}$ nanoparticles showed in A, SAED pattern indicated an face center cubic (fcc) packing with a lattice constant of around 0.400 nm, confirmed β-palladium hydride phase and H: Pd ratio around 0.43, (C) TEM of $PdH_{0.43}$ nanoparticle, blue rectangle showed the area for HRTEM, (D) zoom in HRTEM of nanoparticle showed in C; upper inset: FFT of HRTEM.

In addition, we performed control experiments to replace our primary amine, n-butylamine, with ethylenediamine, triethylamine, or hydroxy-ethylamine while maintaining the other conditions the same. Our results show no formation of dendrites structure (Figure 2.4) when using other types of amines but still formation of β-palladium hydride phase (Figure 2.5) according to the XRD spectra, where XRD peaks are shifted to lower angles compared to those of pure Pd. These findings suggest that not all type of amines play a role for the successful development of dendritic morphologies. And the formation of palladium hydride phase is not impacted by the

different type of amines since the hydrogen comes from the decomposition of DMF as it was discussed before.[30] Yet, n-butylamine proves indispensable for the formation of stable nanodendrites showing characteristics nanobranches (Figure 2.1, 2.4A).

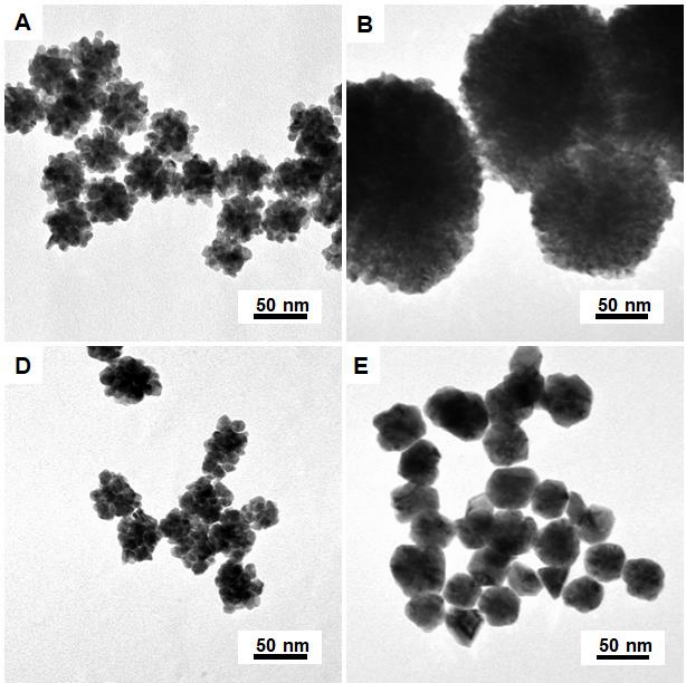

Figure 2.4 (A)TEM image of dendrite palladium hydride synthesized with n-butylamine; TEM image of control experiments with different kinds of amines, all rest conditions were kept same were showed in (B) ethylenediamine; (C) trimethylamine; (D) hydroxyethylamine.

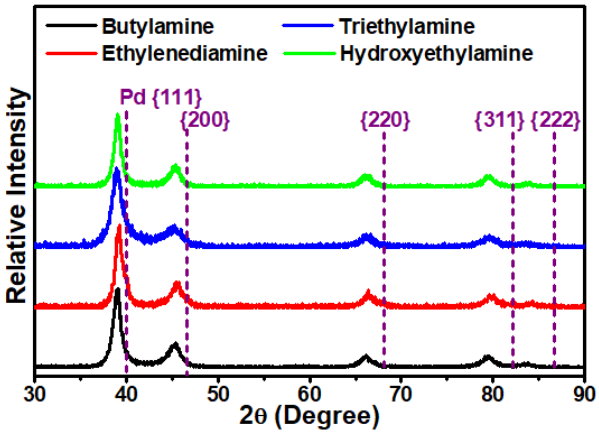

Figure 2.5 Corresponded XRD comparison with typical synthesis with n-butylamine and control experiments with different kinds of amine replace n-butylamine and all rest conditions were kept same.

Subsequent to the success of $PdH_{0.43}$ dendrites synthesis, we move forward to a design of one-step synthesis to achieve $M/PdH_{0.43}$ dendritic nanostructure where M represents a metal, nickel (Ni) in this study. Bimetallic Pd-Ni nanoparticles with Ni-rich surface proved enhanced catalytic activity.[26-28] As a matter of fact, our $Ni/PdH_{0.43}$ dendrites show a much-improved catalytic selectivity and high activity towards benzyl alcohol oxidation reaction if compared with their counterpart $PdH_{0.43}$ dendrites and commercial Pd/C. $Ni/PdH_{0.43}$ dendrites were synthesized by mixing $Pd(acac)_2$, nickel (II) acetylacetonate [$Ni(acac)_2$], and n-butylamine in DMF (for more details, see section 2.4 Experimental Methods). The products were collected by centrifuge and washed several times with acetone/isopropanol mixture as in the same way of $PdH_{0.43}$ dendrites. Further characterization was performed on the collected material (Figure 2.6). TEM images (Figure 2.6A) confirm the development of the uniform nanodendritic structures. Powder XRD (Figure 2.6B) pattern indicates an fcc packing structure with a lattice parameter of 0.3996 nm

indicating the presence of β-palladium hydride phase with an H:Pd ratio of around 0.43, same as the case of $PdH_{0.43}$ dendrites. The Ni:Pd ratio is found to be 0.17 based on the energy dispersive spectroscopy (EDS). Similarly, HRTEM analysis (Figure 2.6C) indicates an average {111} interplane distance of about 0.231 nm matching a lattice parameter of about 0.400 nm, confirming the presence of β-palladium hydride phase. It should be highlighted that, in powder XRD and HRTEM results, palladium hydride is the dominant phase. In this context, Ni content in the product seems not forming an alloy compound with palladium. Therefore, these findings suggest an initial development of $PdH_{0.43}$ seeds, followed by the reduction of Ni and growth onto $PdH_{0.43}$ surface, ending with a $Ni/PdH_{0.43}$ structure. In fact, EDS map image shows clearly a high concentration of palladium at the core whereas nickel is mostly enriched on the surface (Figure 2.6D and 2.7). Red arrows in HRTEM images (Figure 2.6C) indicate the formation of islands with different contrast from the internal structure suggesting a nickel content on the outmost surface on palladium hydride in accordance with previous evidence. To asses surface properties and oxidation states of the metals on both dendrites, which are $PdH_{0.43,}$ and $Ni/PdH_{0.43}$, x-ray photoelectron spectroscopy (XPS) was employed (Figure 2.11). The Pd 3d spectra of both dendrites (Figure 2.11A, C respectively) confirms the Pd is mainly in Pd^0 metallic state. In the case of Ni in $Ni/PdH_{0.43}$ nanodendrites, the Ni is found to be around 40.3% of metallic Ni^0, and a 59.7% of Ni^{2+} (Figure 2.11E). XPS results are explained in detail later in this section.

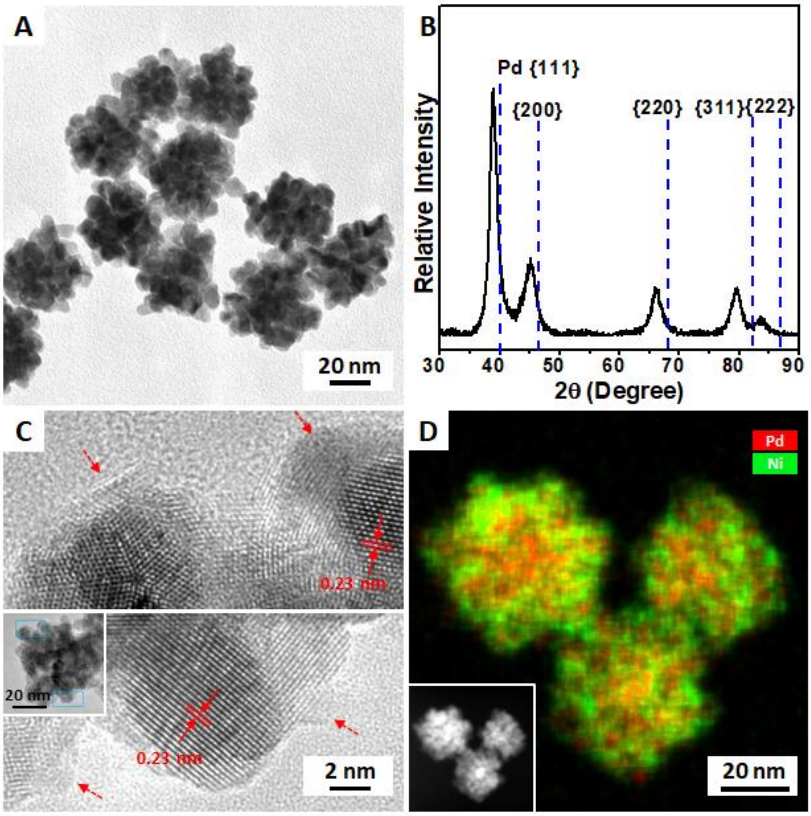

Figure 2.6 (A) TEM of dendriet Ni/$PdH_{0.43}$, (B) powder XRD of dendriet Ni/$PdH_{0.43}$, blue perpendicular lines indicating the diffraction pattern position of Pd, (C) HRTEM of Ni/$PdH_{0.43}$, bottom insert: zoom out image showing the area for HRTEM with blue rectangle, (D) EDS map of Pd (red) and Ni (green) distribution, bottom insert: STEM image of same area.

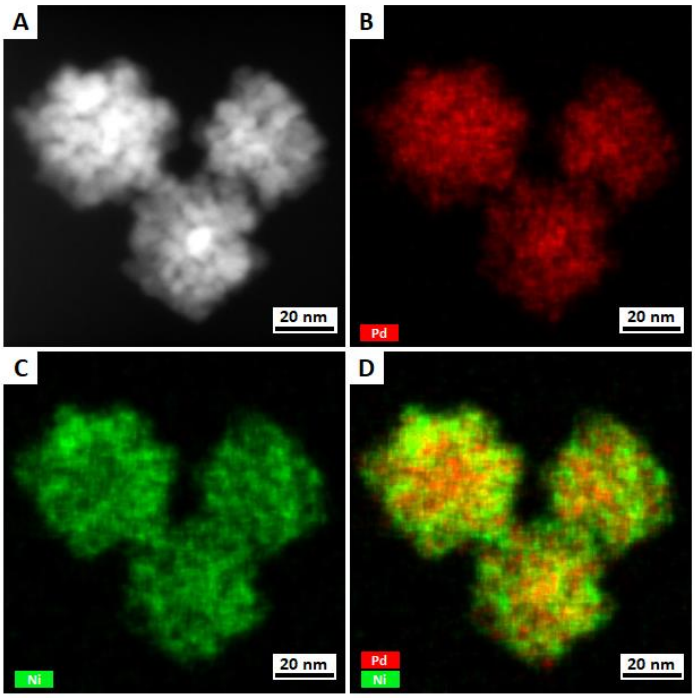

Figure 2.7 Individual and overlapped EDS element distribution corresponded to Figure 3D, (A) STEM of the same area for EDS mapping (B) Pd distribution, (C) Ni distribution, (D) Ni, Pd overlap.

Similar to $PdH_{0.43}$ nanodendrite studies, control experiment without n-butylamine is also performed for Ni/$PdH_{0.43}$ synthesis (Figure 2.8), confirming once again no formation of dendrites in the absence of the primary amine (Figure 2.8A) but still formation of β-palladium hydride phase as it is observed from the XRD pattern (Figure 2.8B). The above results also suggest that $PdH_{0.43}$ formation happens first, soon after the temperature of decomposition of DMF is reached, following by the surface coverage of nickel.

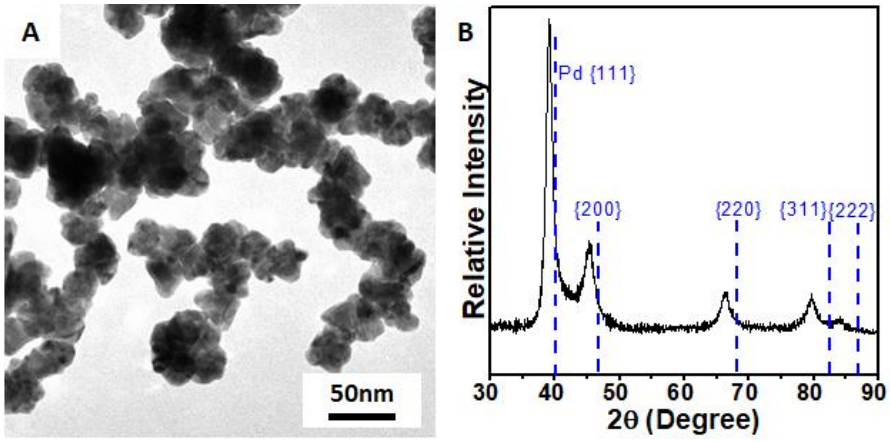

Figure 2.8 $Ni/PdH_{0.43}$ control experiment without n-butylamine, all rest conditions were kept same (A) TEM; (B) XRD.

Finally, to assess the catalytic activity of our synthesized dendrites nanomaterials, selective oxidation of benzyl alcohol reaction was used as the model reaction. The reaction was performed by dispersing 5 mg of Pd for as catalyst on 2 mL of benzyl alcohol. The reaction was kept at 100 °C in 2 atm of oxygen. We found that for the products of the benzyl alcohol oxidation reaction, that is, toluene, benzaldehyde, benzoic acid, and benzyl benzoate, (Table 2.2), $Ni/PdH_{0.43}$ dendrites exhibit the highest selectivity towards benzaldehyde with a value of 92 % and still at a high conversion rate of 95.4 % if compared with the selectivity of 71.8 % and 53.5 %, and conversion rate of 97 % and 96.4 % of $PdH_{0.43}$ dendrites and commercial Pd/C respectively. Considering that $Ni/PdH_{0.43}$ and $PdH_{0.43}$ nanodendrites are similar in morphology, size and hydride composition, it is reasonable to suggest that the excellent selectivity to benzaldehyde of $Ni/PdH_{0.43}$ is attributed to the nickel-rich surface onto the $PdH_{0.43}$ core.

Table 2.1 Performance comparison for Pd/C and dendrite $PdH_{0.43}$, and dendrite $Ni/PdH_{0.43}$. Benzyl alcohol oxidation conversion and product selectivity. The turnover frequency (TOF) calculation is based on 3 h of measurements.

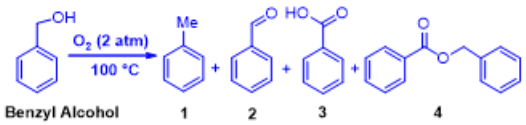

Catalyst	Conversion (%)	Selectivity (%)				TOF
		1	2	3	4	($/s^{-1}$)
Pd	96.4	37.4	53.5	1.3	7.8	0.11
$PdH_{0.43}$	97.0	28.1	71.8	0	0	0.76
$Ni/PdH_{0.43}$	95.4	7.2	92.0	0	0.8	0.74

After testing the model reaction, our catalysts were collected for further stability characterization (Figure 2.9 and 2.10). The outstanding stability of our dendrites is also confirmed by XRD spectra where palladium hydride and nickel/palladium hydride dendrites maintained the hydride phase, presenting a lattice parameter of about 0.3996 nm which correspond to the H:Pd ratio of 0.43 (Figure 2.10).

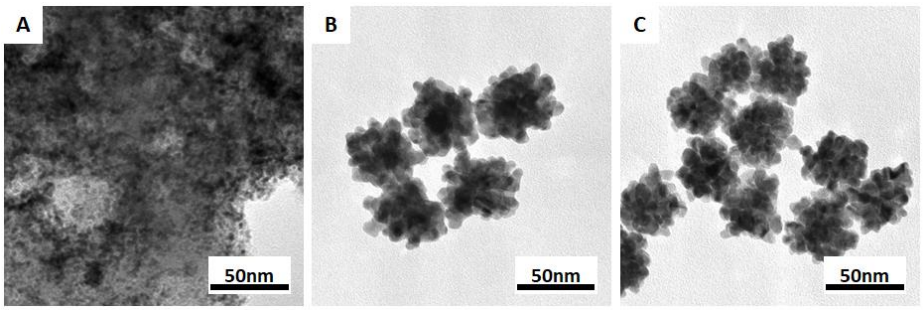

Figure 2.9 TEM of catalysts for benzyl alcohol oxidation (A) Pd/C (10% Pd), (B) dendrite $PdH_{0.43}$ (C) dendrite $Ni/PdH_{0.43}$.

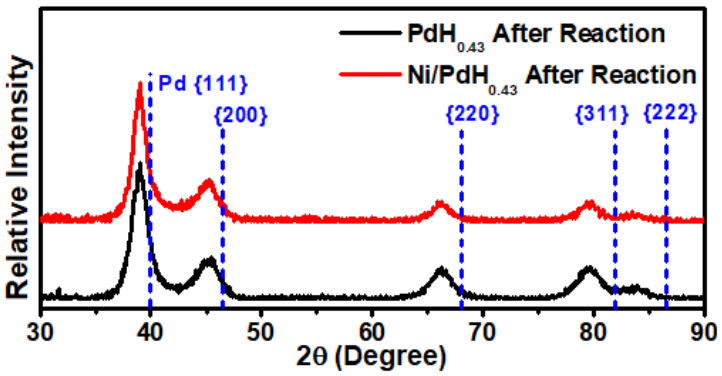

Figure 2.10 XRD of dendrite $PdH_{0.43}$ and dendrite $Ni/PdH_{0.43}$ collected after the catalytic reaction.

Additionally, XPS spectra of $PdH_{0.43}$ and $Ni/PdH_{0.43}$ dendrites before and after reaction (Figure 2.11) reveal no significant difference in their Pd and Ni chemical states. For instance, XPS of the initial $PdH_{0.43}$ dendrites exposes a Pd^0 metallic state of around 81.1 % (Figure 2.11A) versus a Pd^0 76.9 % after the catalytic reaction (Figure 2.11B). In a similar way, the initial $Ni/PdH_{0.43}$ dendrites showed an initial metallic state of 83.4 % Pd^0 and 40.3 % Ni^0 (Figure 2.11C, E respectively) versus an 83.8 % Pd^0 and 29.2 % Ni^0 after reaction (Figure 2.11D, F respectively). Thus, chemical states of the tested catalysts are not significantly changed even after the test in benzyl alcohol oxidation reaction.

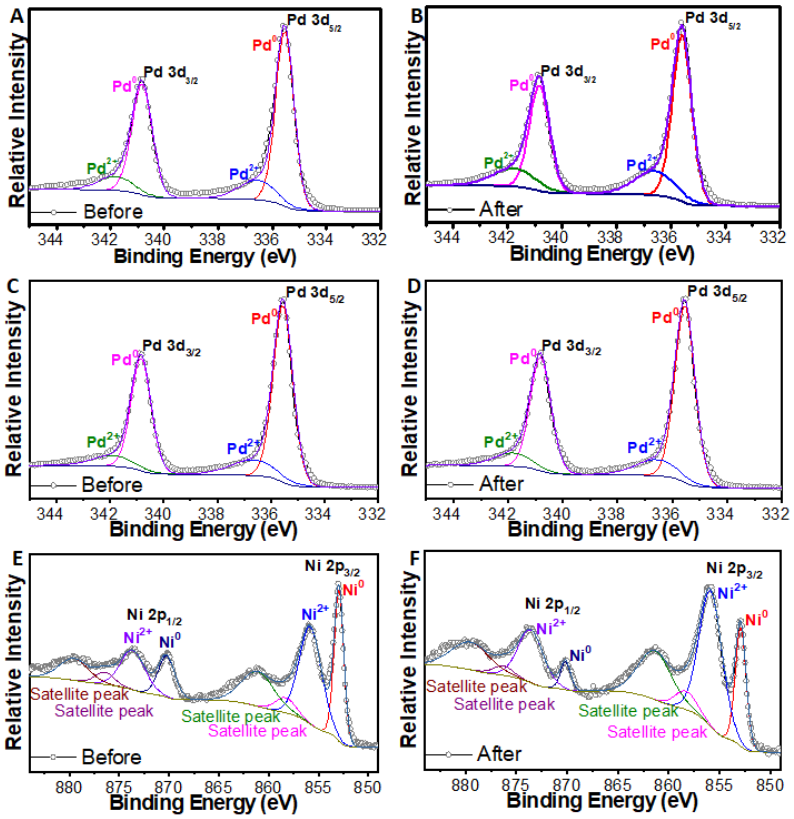

Figure 2.11 (A,B) XPS of dendrite $PdH_{0.43}$ before (A) and after (B) reaction. (C-F) XPS of dendrite $Ni/PdH_{0.43}$ before (C, E) and after (D, F) reaction.

To further confirm high selectivity towards benzaldehyde due to the unique interaction between the Ni-rich surface and $PdH_{0.43}$, we tested the benzyl alcohol oxidation reaction on $Ni/PdH_{0.43}$ and Pd-Ni alloy again with carbon black support. In a typical procedure, $Ni/PdH_{0.43}/C$ was synthesized first, washed and collected. Pd-Ni/C material was obtained by annealing $Ni/PdH_{0.43}/C$ powder at 400 °C in an argon atmosphere for 2 h (Figure 2.12A). Further characterization was performed on both nanostructures (Figure 2.12). TEM images of $Ni/PdH_{0.43}/C$ and Pd-Ni/C catalysts (Figure 2.12B, C) proved that both materials maintain similar size and morphology, therefore, serves as a comparison between hydride $Ni/PdH_{0.43}$ and non-hydride Pd-

Ni(alloy) materials. XRD spectrum (Figure 2.12D) also proves the complete transformation of $Ni/PdH_{0.43}/C$ (black line) to Pd-Ni/C (red line) where the peaks are shifted to higher angles, showing the formation of Pd-Ni alloy on carbon support.

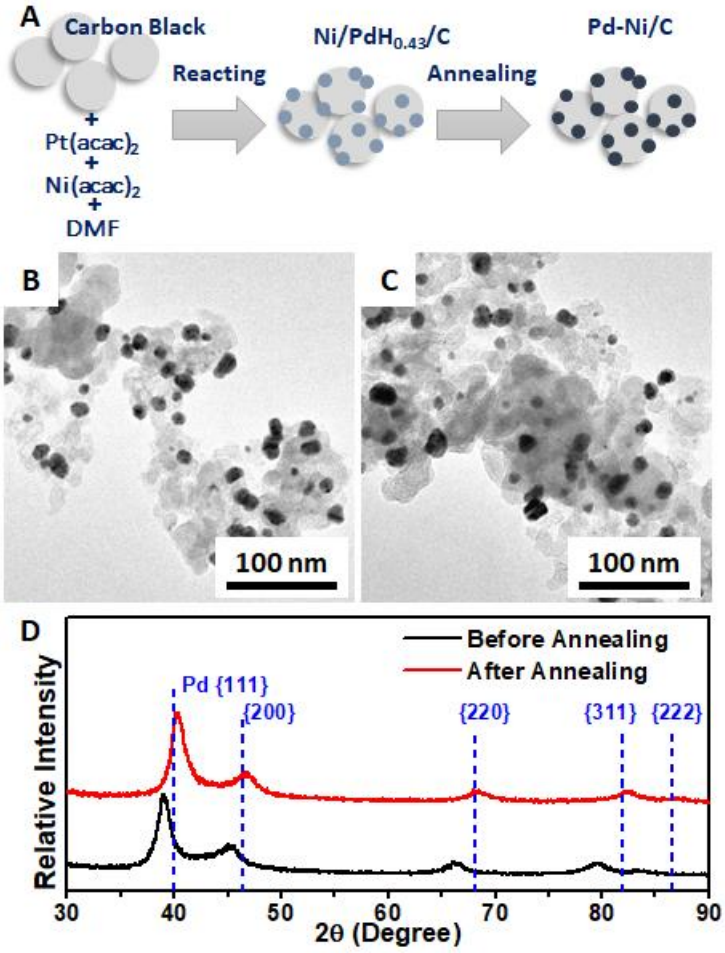

Figure 2.12 (A)Schematic of control experiment design of preparing nickel palladium hydride on carbon ($Ni/PdH_{0.43}/C$) and palladium nickel on carbon (Pd-Ni/C) for comparing selectivity of benzyl alcohol oxidation. Pd-Ni/C was prepared by annealing $Ni/PdH_{0.43}/C$, so similar size and morphology maintained. TEM of (B) $Ni/PdH_{0.43}/C$, (C) Pd-Ni/C, (D) XRD comparison of $Ni/PdH_{0.43}/C$ and Pd-Ni/C formed after annealing of $Ni/PdH_{0.43}/C$.

Lastly, benzyl alcohol oxidation reaction of the developed catalysts (Table 2.3) confirmed higher catalytic activity for the hydride compound （$Ni/PdH_{0.43}/C$）than non-hydride compound (Pd-Ni/C). This is also attributed to the fact that Pd-Ni/C is forming an alloy rather than a Ni surface rich on $PdH_{0.43}$, once again proving the unique feature of our synthesized $Ni/PdH_{0.43}$ nanodendrites. For instance, $Ni/PdH_{0.43}/C$ material exhibited a superior selectivity towards benzaldehyde of 90.2 % and a conversion rate of 95.1 %, whereas the non-hydride alloy Pd-Ni/C showed a lower selectivity of 82.9 % and conversion rate of 94.3 %. These results suggest that Ni modified the $PdH_{0.43}$ surface presents advantages over Pd-Ni alloy, which agrees with our previous observations (Figure 2.6, 2.7, Table 2.2).

Table 2.2 Comparison of selectivity of benzyl alcohol oxidation between $Ni/PdH_{0.43}/C$ and Pd-Ni/C.

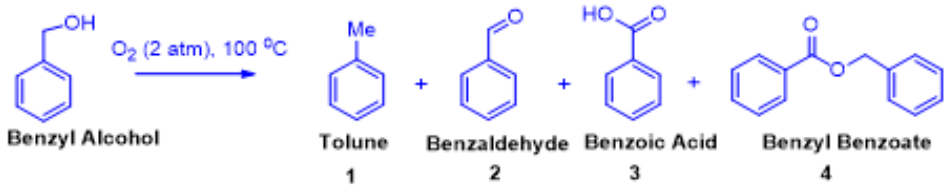

Catalyst	Time (min)	Conversion (%)	Selectivity (%)				TOF ($/s^{-1}$)
			1	2	3	4	
$Ni/PdH_{0.43}/C$	180	95.1	2.2	90.2	1.1	6.5	0.28
Pd-Ni/C	360	94.3	12.3	82.9	0	4.8	0.13

2.3 Conclusion

In summary, we have successfully developed $PdH_{0.43}$ and $Ni/PdH_{0.43}$, a new class of stable nanodendritic hydride materials. $PdH_{0.43}$ and $Ni/PdH_{0.43}$ are found to be good nanostructures showing remarkable stability in what refers to composition and phase. In terms of catalytic activity, both nanostructures exhibited outstanding catalytic activity, higher than commercial Pd/C due to its composition and dendritic structure. In fact, our synthesized $Ni/PdH_{0.43}$ nanodendrites showed the highest selectivity and conversion rate of all of them. The experimental evidence revealed that the enhancement of selectivity to benzaldehyde of $Ni/PdH_{0.43}$ was mainly attributed to the synergistic of the Ni-rich surface and the $PdH_{0.43}$. The newly developed $Ni/PdH_{0.43}$ nanodendrites demonstrate their potential in applications towards greener process in benzyl alcohol oxidation reactions through the combined morphology and controlled surface composition to tune selectivity towards benzaldehyde.

2.4 Experimental Methods

2.4.1 Chemicals and materials. palladium(II) acetylacetonate, $[Pd(acac)_2]$, nickel(II) acetylacetonate, $[Ni(acac)_2]$sodium tetrachloropalladate(II) (Na_2PdCl_4), n-butylamine, ethylenediamine, trimethylamine, hydroxyethylamine, Pd/C (10% Pd) were purchased from Sigma Aldrich. N, N-Dimethylformamide (DMF), acetone and isopropanol were purchased from Fisher Scientific. Ethanol was purchased from Decon Labs, Inc. Vulcan XC-72 carbon black was obtained from Cabot Corporation. Water used was Ultrapure Millipore (18.2 MΩ·cm).

2.4.2 Synthesis of $PdH_{0.43}$ nanodendrites. 8 mg of $Pd(acac)_2$, 100 μL of n-butylamine was dissolved in 10 mL of DMF within 25 mL vial was heated at 160 ºC in an oil bath for 4 h. The obtained nanomaterials were separated from solvent through centrifugation and then washed with acetone/isopropanol three times. Time tracking studies during synthesis of hydride dendrites were performed from 15 min to 240 min.

2.4.3 Control experiments for replacing small molecules. 8 mg $Pd(acac)_2$ and 100 μL of small molecules (ethylenediamine, triethylamine or hydroxyethylamine) were dissolved in 10 mL DMF within a 25 mL glass vial. The sealed vial was kept at 160 ºC for 4 h. The obtained nanomaterials were separated from solvent through centrifugation and then washed with acetone/isopropanol three times.

2.4.4 Synthesis of Ni/$PdH_{0.43}$ nanodendrites. 10 mg of $Pd(acac)_2$, 5 mg $Ni(acac)_2$, 50 μL of n-butylamine was dissolved in 10 mL of DMF within 25 mL vial was heated at 160 ºC in an oil bath for 12 h. The obtained nanomaterials were separated from solvent through centrifugation and then washed with acetone/isopropanol three times.

2.4.5 Synthesis of nanoparticle Ni/$PdH_{0.43}$/C. 14 mg carbon black was dissolved in 9 mL of DMF. Then, 8 mg of $Pd(acac)_2$, 4 mg $Ni(acac)_2$, was dissolved in 1 mL of DMF and mixed with 9 mL DMF solution, which contained carbon black, within a 25 mL vial. The vial was heated at 160 ºC in an oil bath for 12 h. The obtained nanomaterials were separated from solvent through centrifugation and then washed with acetone/isopropanol three times.

2.4.6 Synthesis of nanoparticle Pd-Ni/C. The obtained nanoparticle Ni/$PdH_{0.43}$/C powder was annealed in Ar atmosphere for 2 h at 400˚C. Through the annealing, the Ni/$PdH_{0.43}$/C was converted to nanoparticle Pd-Ni/C.

2.4.7 Characterization. Transmission electron microscopy (TEM) images were taken on an FEI T12 transmission electron microscope operated at 120 kV. High-resolution transmission electron microscopy (HRTEM) images, selected area electron diffraction (SAED) were taken on an FEI Titan transmission electron microscope operated at 300 kV. EDS mapping and high angle annular dark field HAADF-STEM image was taken on a Titan X operated at 200 kV. The samples were prepared by dropping ethanol dispersion of samples onto carbon-coated copper TEM grids (Ladd Research, Williston, VT) using pipettes and dried under ambient condition. X-ray powder diffraction patterns were collected on a Panalytical X'Pert Pro X-ray Powder Diffractometer with Cu-Kα radiation. X-ray photoelectron spectroscopy (XPS) tests were done with Kratos AXIS Ultra DLD spectrometer.

2.4.8 Catalysis Study. For benzyl alcohol catalytic oxidation study, the Pd loading in each catalysis study was maintained to be 5 mg (commercial Pd/C, dendrite $PdH_{0.43}$, or dendrite Ni/$PdH_{0.43}$ used as a catalyst) and the amount of benzyl alcohol was maintained to be 2 mL for each catalytic test. The catalyst is dispersed in 2 mL benzyl alcohol, and no additional solvent is needed. The catalysis was carried out at 100 ˚C in oxygen with a pressure of 2 atm.

When particle Ni/$PdH_{0.43}$/C or particle Pd-Ni/C used as a catalyst, the Pd loading in each catalysis

study was maintained to be 10 mg for each catalysis study. After catalysis, the catalyst was separated from the product by centrifugation. Then the product was diluted with acetone for further composition analysis. Chemical composition analysis was done by gas chromatography-mass spectroscopy (GC-MS; Shimadzu GCMS-QP2010 Plus).

2.5 References

1. Tian, N.; Zhou, Z.-Y.; Sun, S.-G.; Ding, Y.; Wang, Z. L., Synthesis of Tetrahexahedral Platinum Nanocrystals with High-Index Facets and High Electro-Oxidation Activity. *Science* **2007,** 316, 732-735.
2. Wu, Z.; Zhang, Y.; Wang, B.; Qian, G.; Tao, T., Synthesis of palladium dendritic nanostructures on amidoxime modified polyacrylonitrile fibers through a complexing-reducing method. *Mater. Sci. Eng., B* **2013,** 178, 923-929.
3. Zhu, G.; Jiang, Y.; Lin, F.; Zhang, H.; Jin, C.; Yuan, J.; Yang, D.; Zhang, Z., In situ study of the growth of two-dimensional palladium dendritic nanostructures using liquid-cell electron microscopy. *Chem. Commun.* **2014,** 50, 9447-9450.
4. Eid, K.; Ahmad, Y. H.; Yu, H.; Li, Y.; Li, X.; AlQaradawi, S. Y.; Wang, H.; Wang, L., Rational one-step synthesis of porous PtPdRu nanodendrites for ethanol oxidation reaction with a superior tolerance for CO-poisoning. *Nanoscale* **2017,** 9, 18881-18889.
5. Lu, L.; Chen, S.; Thota, S.; Wang, X.; Wang, Y.; Zou, S.; Fan, J.; Zhao, J., Composition Controllable Synthesis of PtCu Nanodendrites with Efficient Electrocatalytic Activity for Methanol Oxidation Induced by High Index Surface and Electronic Interaction. *J. Phys. Chem. C* **2017,** 121, 19796-19806.
6. da Silva, A. G. M.; Rodrigues, T. S.; Slater, T. J. A.; Lewis, E. A.; Alves, R. S.; Fajardo, H. V.; Balzer, R.; da Silva, A. H. M.; de Freitas, I. C.; Oliveira, D. C.; Assaf, J. M.; Probst, L. F. D.; Haigh, S. J.; Camargo, P. H. C., Controlling Size, Morphology, and Surface Composition of AgAu Nanodendrites in 15 s for Improved Environmental Catalysis under Low Metal Loadings. *ACS Applied Materials & Interfaces* **2015,** 7, 25624-25632.

7. Fu, S.; Zhu, C.; Shi, Q.; Xia, H.; Du, D.; Lin, Y., Highly branched PtCu bimetallic alloy nanodendrites with superior electrocatalytic activities for oxygen reduction reactions. *Nanoscale* **2016,** 8, 5076-5081.
8. Zhang, X.-F.; Zhu, X.-Y.; Feng, J.-J.; Wang, A.-J., Solvothermal synthesis of N-doped graphene supported PtCo nanodendrites with highly catalytic activity for 4-nitrophenol reduction. *Appl. Surf. Sci.* **2018,** 428, 798-808.
9. Pillai, U. R.; Sahle-Demessie, E., Sn-exchanged hydrotalcites as catalysts for clean and selective Baeyer–Villiger oxidation of ketones using hydrogen peroxide. *J. Mol. Catal. A: Chem.* **2003,** 191, 93-100.
10. Meng, C.; Yang, K.; Fu, X.; Yuan, R., Photocatalytic Oxidation of Benzyl Alcohol by Homogeneous CuCl2/Solvent: A Model System to Explore the Role of Molecular Oxygen. *ACS Catalysis* **2015,** 5, 3760-3766.
11. Enache, D. I.; Edwards, J. K.; Landon, P.; Solsona-Espriu, B.; Carley, A. F.; Herzing, A. A.; Watanabe, M.; Kiely, C. J.; Knight, D. W.; Hutchings, G. J., Solvent-Free Oxidation of Primary Alcohols to Aldehydes Using Au-Pd/TiO2 Catalysts. *Science* **2006,** 311, 362-365.
12. Galvanin, F.; Sankar, M.; Cattaneo, S.; Bethell, D.; Dua, V.; Hutchings, G. J.; Gavriilidis, A., On the development of kinetic models for solvent-free benzyl alcohol oxidation over a gold-palladium catalyst. *Chem. Eng. J.* **2018,** 342, 196-210.
13. Pillai, U. R.; Sahle-Demessie, E., Oxidation of alcohols over Fe3+/montmorillonite-K10 using hydrogen peroxide. *Applied Catalysis A: General* **2003,** 245, 103-109.
14. Sheldon, R. A.; Kochi, J. K., *Metal-catalyzed oxidations of organic compounds : mechanistic principles and synthetic methodology including biochemical processes*. Academic Press: New York, 1981.

15. Long, R.; Mao, K.; Ye, X.; Yan, W.; Huang, Y.; Wang, J.; Fu, Y.; Wang, X.; Wu, X.; Xie, Y.; Xiong, Y., Surface Facet of Palladium Nanocrystals: A Key Parameter to the Activation of Molecular Oxygen for Organic Catalysis and Cancer Treatment. *J. Am. Chem. Soc.* **2013,** 135, 3200-3207.
16. Mori, K.; Hara, T.; Mizugaki, T.; Ebitani, K.; Kaneda, K., Hydroxyapatite-Supported Palladium Nanoclusters: A Highly Active Heterogeneous Catalyst for Selective Oxidation of Alcohols by Use of Molecular Oxygen. *J. Am. Chem. Soc.* **2004,** 126, 10657-10666.
17. Liang, H.-P.; Lawrence, N. S.; Wan, L.-J.; Jiang, L.; Song, W.-G.; Jones, T. G. J., Controllable Synthesis of Hollow Hierarchical Palladium Nanostructures with Enhanced Activity for Proton/Hydrogen Sensing. *J. Phys. Chem. C* **2008,** 112, 338-344.
18. Yamauchi, M.; Ikeda, R.; Kitagawa, H.; Takata, M., Nanosize Effects on Hydrogen Storage in Palladium. *J. Phys. Chem. C* **2008,** 112, 3294-3299.
19. Kumara, L. S. R.; Sakata, O.; Kobayashi, H.; Song, C.; Kohara, S.; Ina, T.; Yoshimoto, T.; Yoshioka, S.; Matsumura, S.; Kitagawa, H., Hydrogen storage and stability properties of Pd–Pt solid-solution nanoparticles revealed via atomic and electronic structure. *Scientific Reports* **2017,** 7, 14606.
20. Zhang, J.; Chen, M.; Li, H.; Li, Y.; Ye, J.; Cao, Z.; Fang, M.; Kuang, Q.; Zheng, J.; Xie, Z., Stable palladium hydride as a superior anode electrocatalyst for direct formic acid fuel cells. *Nano Energy* **2018,** 44, 127-134.
21. Zhu, Y.; Gao, C.; Bai, S.; Chen, S.; Long, R.; Song, L.; Li, Z.; Xiong, Y., Hydriding Pd cocatalysts: An approach to giant enhancement on photocatalytic CO2 reduction into CH4. *Nano Research* **2017,** 10, 3396-3406.

22. Lu, Y.; Wang, J.; Peng, Y.; Fisher, A.; Wang, X., Highly Efficient and Durable Pd Hydride Nanocubes Embedded in 2D Amorphous NiB Nanosheets for Oxygen Reduction Reaction. *Adv. Energy Mater.* **2017,** 7, 1700919.

23. Weng, Z.; Liu, W.; Yin, L.-C.; Fang, R.; Li, M.; Altman, E. I.; Fan, Q.; Li, F.; Cheng, H.-M.; Wang, H., Metal/Oxide Interface Nanostructures Generated by Surface Segregation for Electrocatalysis. *Nano Lett.* **2015,** 15, 7704-7710.

24. Yi, W.; Yuan, W.; Meng, Y.; Zou, S.; Zhou, Y.; Hong, W.; Che, J.; Hao, M.; Ye, B.; Xiao, L.; Wang, Y.; Kobayashi, H.; Fan, J., A Rational Solid-State Synthesis of Supported Au–Ni Bimetallic Nanoparticles with Enhanced Activity for Gas-Phase Selective Oxidation of Alcohols. *ACS Applied Materials & Interfaces* **2017,** 9, 31853-31860.

25. Gao, L.; Wang, Y.; Li, H.; Li, Q.; Ta, N.; Zhuang, L.; Fu, Q.; Bao, X., A nickel nanocatalyst within a h-BN shell for enhanced hydrogen oxidation reactions. *Chemical Science* **2017,** 8, 5728-5734.

26. Feng, Y.; Shao, Q.; Ji, Y.; Cui, X.; Li, Y.; Zhu, X.; Huang, X., Surface-modulated palladium-nickel icosahedra as high-performance non-platinum oxygen reduction electrocatalysts. *Science Advances* **2018,** 4, eaap8817.

27. Obradović, M. D.; Stančić, Z. M.; Lačnjevac, U. Č.; Radmilović, V. V.; Gavrilović-Wohlmuther, A.; Radmilović, V. R.; Gojković, S. L., Electrochemical oxidation of ethanol on palladium-nickel nanocatalyst in alkaline media. *Applied Catalysis B: Environmental* **2016,** 189, 110-118.

28. Jiang, S.; Yi, B.; Zhao, Q.; Yu, H.; Shao, Z., Palladium–nickel catalysts based on ordered titanium dioxide nanorod arrays with high catalytic peformance for formic acid electro-oxidation. *RSC Advances* **2017,** 7, 11719-11723.

29. Dimitratos, N.; Lopez-Sanchez, J. A.; Morgan, D.; Carley, A. F.; Tiruvalam, R.; Kiely, C. J.; Bethell, D.; Hutchings, G. J., Solvent-free oxidation of benzyl alcohol using Au-Pd catalysts prepared by sol immobilisation. *PCCP* **2009,** 11, 5142-5153.
30. Zhao, Z.; Huang, X.; Li, M.; Wang, G.; Lee, C.; Zhu, E.; Duan, X.; Huang, Y., Synthesis of Stable Shape-Controlled Catalytically Active β-Palladium Hydride. *J. Am. Chem. Soc.* **2015,** 137, 15672-15675.
31. Wolf, R. J.; Lee, M. W.; Davis, R. C.; Fay, P. J.; Ray, J. R., Pressure-composition isotherms for palladium hydride. *Phys. Rev. B* **1993,** 48, 12415-12418.
32. Flanagan, T. B.; Oates, W. A., The Palladium-Hydrogen System. *Annu. Rev. Mater. Sci.* **1991,** 21, 269-304.
33. Eastman, J. A.; Thompson, L. J.; Kestel, B. J., Narrowing of the palladium-hydrogen miscibility gap in nanocrystalline palladium. *Phys. Rev. B* **1993,** 48, 84-92.
34. Schirber, J. E.; Morosin, B., Lattice constants of β-PdHx and β-PdDx with x near 1.0. *Phys. Rev. B* **1975,** 12, 117-118.
35. Xue, Z.; Li, M.; Rao, H.; Yin, B.; Zhou, X.; Liu, X.; Lu, X., Phase transformation-controlled synthesis of CuO nanostructures and their application as an improved material in a carbon-based modified electrode. *RSC Advances* **2016,** 6, 12829-12836.

Chapter 3

3 Surface decoration of β-Palladium hydride catalyst and the effects on its properties

3.1 Introduction

Metal hydrides are well known systems with environmental friendly applications in terms of storage and use of energy, having specific relevance in hydrogen storage, fuel cell, batteries, kinetics reversibility studies, and their role as possible candidates for high temperature superconductors.[1,2] Solid solution metal hydride nanoparticles exhibit excellent charging/discharging and/or absorption/desorption of hydrogen gas which is significance for energy related subjects involving hydrogen generation, storage, purification, fuel cell technologies and among others.[3,4] From these, palladium hydride system (PdHx) has been of great interest primarily due to the high solubility of hydrogen on the palladium fcc (Pd-face centered cubic) lattice where they occupy the octahedral vacancies sites leading to a rock salt structure based on neutron diffraction studies of bulk materials (Figure 3.2).[1,2,5,6] Nevertheless, studies have showed that at the right conditions of temperature, composition and morphology, a substantial amount of hydrogen atoms are transferred to the tetrahedral interstices after full coverage of surface which lead to a posterior diffusion into the core of the nanostructures, emerging to a zincblende structure type.[2,7,8]

Moreover, among bulk noble metals, palladium is the only metal that can absorb and desorb hydrogen at near-ambient conditions of temperature and pressure.[9] Palladium hydride properties do not only include adsorption and desorption of hydrogen, but they are also effective for electrocatalytic applications. Overall, palladium hydride and its alloys properties are strongly correlated with their electronic and crystal structure changes.[3] As a matter of fact, electrons from hydrogen dissolution on the host metal lattice, and the subsequent formation of palladium hydride perturb the outer shell electrons of palladium atom which lead to different properties observed in the PdH system.[5] Theoretically, hydrogen concentration in palladium is associated with the number of holes available in the 4d band of palladium because the transfer from H 1s electrons into Pd 4d holes favorer Pd–H bonds.[10] As the concentration of the hydrogen is increased, palladium hydride compound transition from α-phase at low H concentration ($x<0.01$) to co-existence of phases α- β ($0.01<x<0.7$), to finally β-phase rich in H concentration ($x>0.7$) in bulk palladium.[5,11,12] However, palladium hydride nanocrystals materials undergo abruptly to α-phase or β-phase, being the coexistence of phases almost null at nanosizes.[12]

On these basis, palladium hydride system promote its interest as a model system for the rational design of hydrogen storage materials, catalysts, sensors and among others based on their outstanding electronic, magnetic and catalytic properties which are highly dependent on particle size, composition and morphology.[3–5,12]

Even though palladium hydride system has been widely studied for centuries, their mechanism and properties remain ambiguous specially at nano and atomic scale. Several studies, most of them in-situ studies have been presented for a better understanding of its diffusion mechanism related

to size and morphology of nanocrystals, still there has been a lack of agreement in terms of which morphologies perform better during adsorption/desorption of hydrogen. For instance, whereas some studies suggest that octahedral shape are optimal for hydrogen absorption,[13,14] other studies suggest that hydrogen absorption rate increases based on the number of vertices, in which case octahedral shape only possess six vertices which translate into a lower phase transformation from α to β phase, much lower if compared to nanocubes which transformation is faster due to the existence of eight vertices that provide lower-coordination-number sites that accelerate the rate of β-phase nucleation.[12] In similar manner, hydrogen desorption has reported much lower in octahedral shapes if compared to nanocubes.[12,15] For an optimal industrial applications both, absorption/desorption should be fast enough. Still, hydrogen loading has been reported higher in (111) surfaces and lower for (100) surfaces.[15] In general, these studies demonstrates that the uptake and release of hydrogen are highly dependent on faces and vertices of the nanocrystals.

Most of the mentioned recent studies are in-situ monitoring studies where hydrogen uptake into palladium lattice and release out of it are registered simultaneously during the measurements. However, there is a lack of studies for direct but simple synthesis of palladium hydride with practical applications. Moreover, due to in-situ procedures, limitation of sample, stability and reproducibility are some of the major problems associated with them which also leads to a lack of studies related to their properties and how to tune them.

Herein, we reported a simple yet well designed method for the synthesis of stable β palladium hydride with different morphologies and decoration of its surface with organic ligands which lead to different effects in terms of nanocrystal sizes and the ability of tune of its properties. Upon the

use of different capping agents during the synthesis, diverse of properties as optical and magnetic ones have arises, as well as an increase in their hydrogen storage capacity. These properties are found to be different from their palladium and palladium hydride counterparts.

3.2 Results and Discussion

Palladium hydride nanoparticles were synthesized by first mixing palladium precursor (Pd^{2+}) with surfactants to develop the desired morphologies to later disperse their seeds in N,N-Dimethylformamide (DMF) to form the metal hydride compounds. Previously, it has been demonstrated that β-palladium hydride can be synthesized in one step method due to the in-situ decomposition of DMF after reaching its decomposition temperature of around 160 ºC.[16]

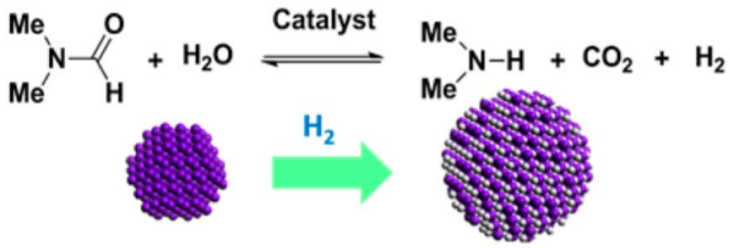

Figure 3. 1 Schematic formation of $PdH_{0.43}$ in DMF[16]

Nonetheless, after temperature tests, we proved that it is only necessary a temperature of 140 ºC to start with the decomposition process of DMF and further formation of $PdH_{0.43}$ (discussed in XRD analysis section) and explained with more details in the experimental methods section. Moreover, as it is well known, palladium is 4d transition metal that crystallizes in a face-centered cubic (FCC) structure with a lattice constant value of 0.389 nm at room temperature. Upon absorption of hydrogen into its structure and formation of palladium hydride (Pd-H), a lattice

expansion is observed which is experimentally confirmed by x-ray diffraction (XRD) studies. Thus, palladium hydride undergoes from a lattice constant of 0.389 nm in the α phase up to 0.410 nm in the β phase. These values can be expressed in terms of specific Pd:Hx ratio, where " x " takes values from $x < 0.017$ for pure α phase (low hydrogen content), up to $x > 0.58$ for pure β phase (rich in hydrogen), and intermediate x values correspond to α-β mixtures in bulk materials.[5,11,12] The next figure illustrate the lattice expansion of palladium to palladium hydride while still preserving its FCC crystal structure.

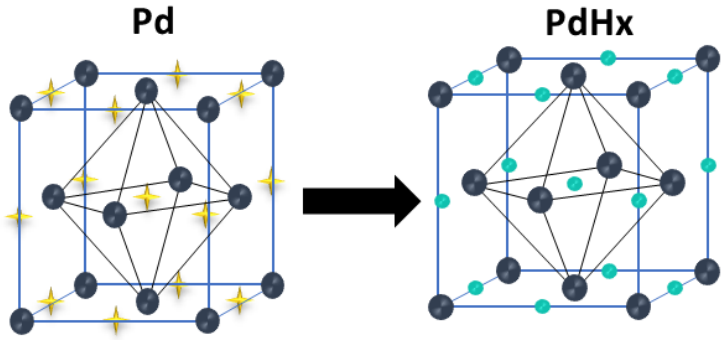

Figure 3. 2 Lattice expansion upon transformation from palladium to palladium hydride due to absorption of hydrogen into its FCC structure.

During this project, we target two facets in our synthesis: 111 and 100 facets which developed into nanotetahedra and nanocubes morphologies respectively. Fresh seeds of palladium tetrahedra and nanocubes are used for the posterior transformation to hydride compounds. Moreover, during our synthesis we added organic ligands to be attached to the surfaces of the nanocrystals. Amines and thiol groups were the chosen ones for this study to surface decorate palladium hydride nanocrystals. Therefore, we tried two different types of amines known as butylamine and octylamine (4 and 8 carbon chains), whereas in the case of thiols we tried five

different ligands as 1-butanethiol, 1-hexanethiol, 1-octanethiol, 1-decanethiol, and 1-dodecanethiol (4, 6, 8, 10, and 12 carbon chains). The following images illustrate the facets used (Figure 3.3) and surface decoration of the palladium hydride nanocrystals (Figure 3.4).

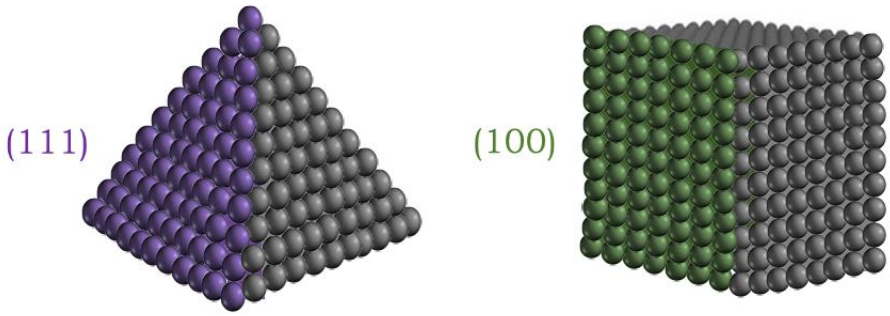

Figure. 3 Palladium nanocrystals with distinctive facets. Schematic representations of the two palladium nanocrystals, tetrahedra (111) and nanocubes (100) facets.

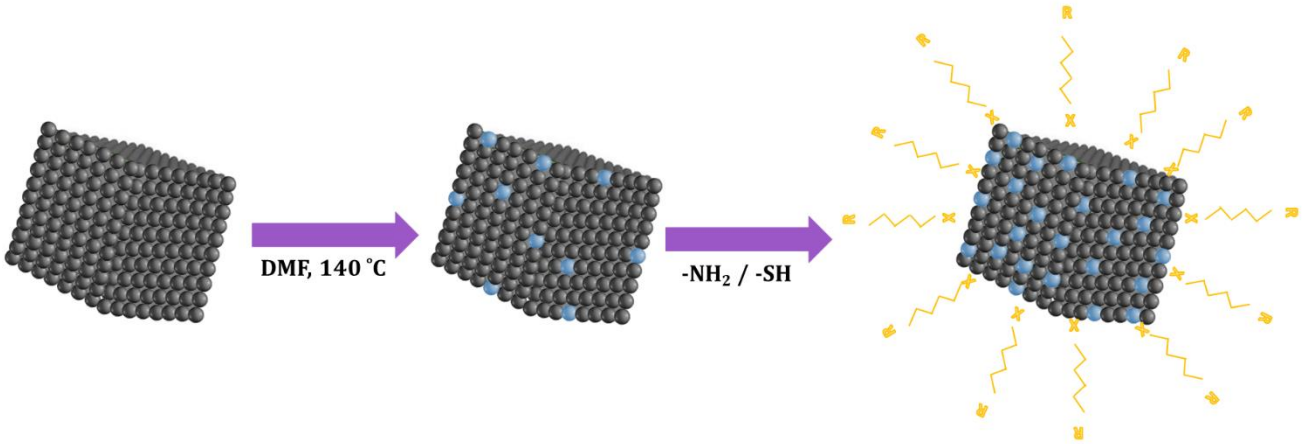

Figure. 4 Schematic presentation of the transformation process from freshly Pd nanocubes seeds to $PdH_{0.43}$ nanocubes and finally to $PdH_{0.58}$ nanocubes with organic molecules decorating its surface.

Transmission electron microscopy (TEM) images and high-resolution transmission electron microscopy (HRTEM) images in Figure 3.5 and 3.6 of the synthesized palladium hydride nanocubes and tetrahedra respectively, reveal consistent and stable morphologies of the nanocrystals with surface decoration upon absorption of hydrogen into its structure. Different conditions of temperature in the range of 140 ºC to 160 ºC, reaction time between 1-16 hours, and volume concentration of the organic ligands from 50 to 200 μL were studied, concluding with optimal conditions at a temperature of 140 ºC, 16 hours of reaction time, and 100 μL for the volume concentration for amines or thiols. For all the cases, stable β palladium hydride nanocrystals were successfully obtained, and displaying different hydrogen storage capacity and properties that are discussed in the following sections.

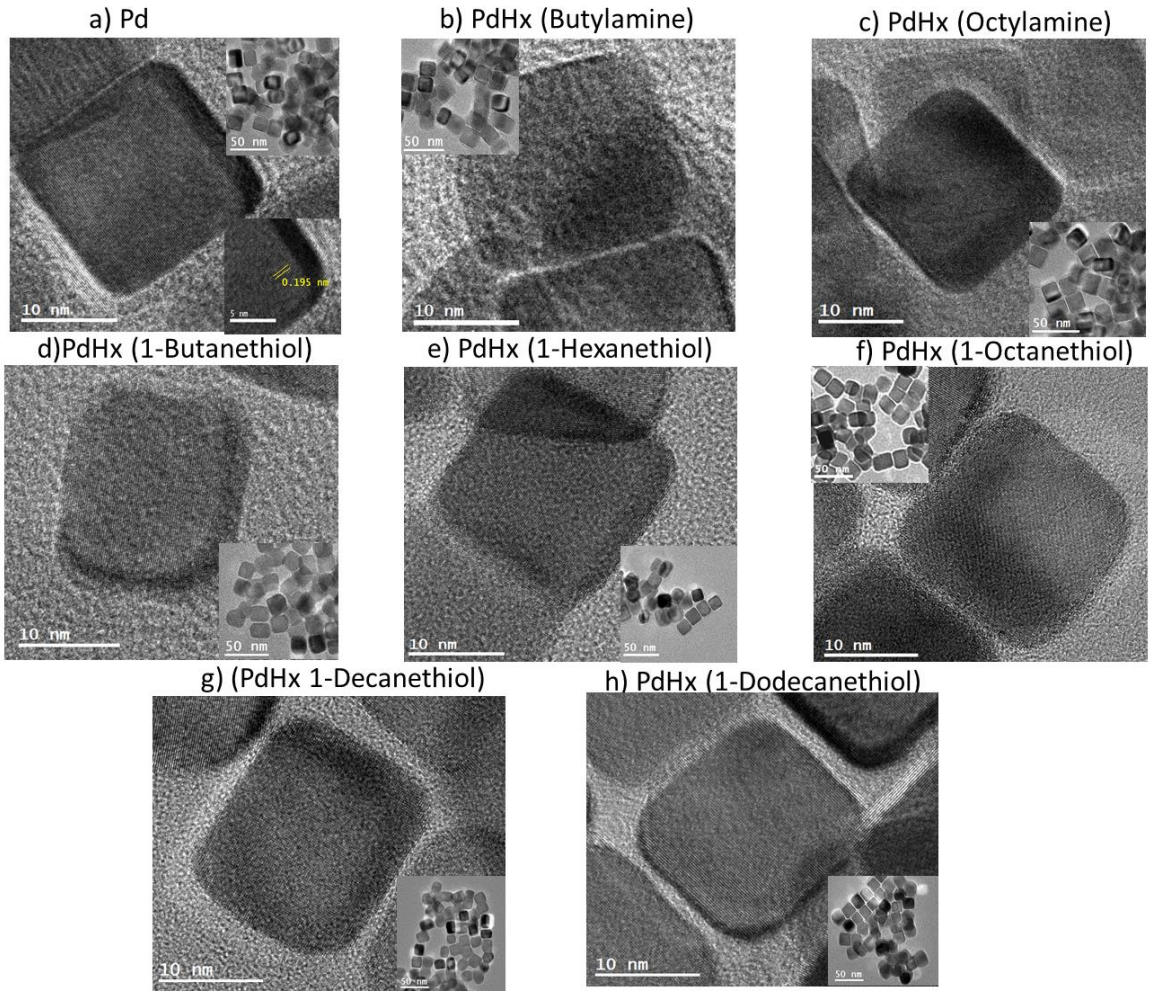

Figure 3. 5 Samples of synthetized PdHx Nanocubes capped with their respective amines or thiol compounds. All the samples have HRTEM images at 10 nm and TEM image at 50 nm. Samples are compared with their respective pure Pd Nanocube sample.

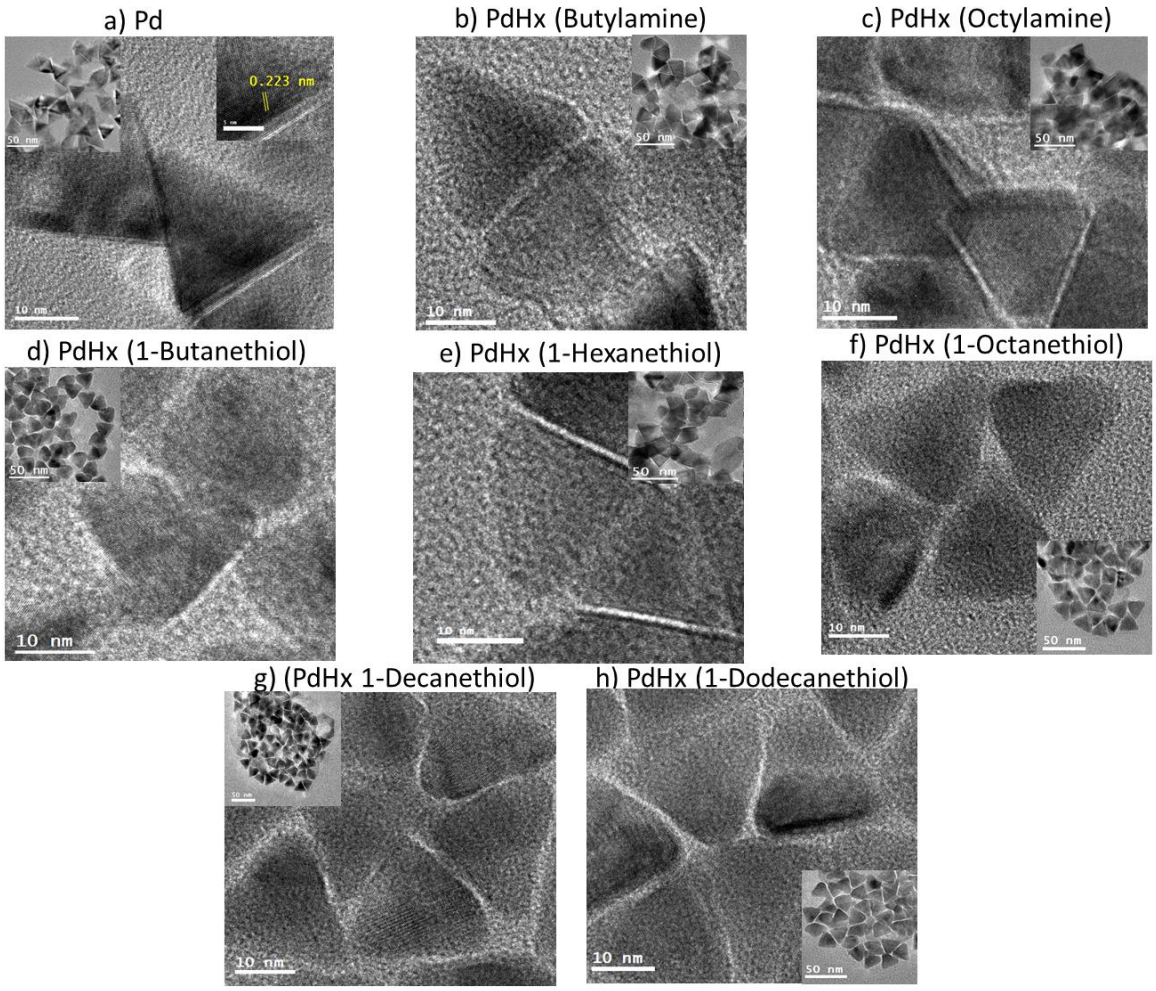

Figure 3. 6 Samples of synthetized PdHx tetrahedra capped with their respective amines or thiol compounds. All the samples have HRTEM images at 10 nm and TEM image at 50 nm. Samples are compared with their respective pure Pd tetrahedra sample.

From images 3.5a and 3.6a, pure palladium nanocubes and tetrahedra are presented as a comparison with the synthesized materials. As it is observed, all the samples remain identical as their initial seeds with no major deformation in terms of their morphologies. In addition, d-spacing of pure palladium nanocubes and tetrahedra samples are measured (right hand side HRTEM

images on figures 3.5a and 3.6a), exhibiting values of around 0.195 nm ± 0.001 and 0.223 nm ± 0.001 respectively. These d-spacing measurements correspond to a lattice parameter of around 0.389 nm based on face centered cubic (fcc) structure for pure palladium nanocubes and tetrahedra.

For a better understanding and comparison between surface decorated nanocrystals (100 and 111 facets), we present in the next Figure 3.7 one sample of each morphology and coated both of them with the same organic ligand (1-dodecanethiol). Figure 3.7a-c show palladium hydride nanocubes with a d-spacing value of 0.20 nm which is higher than the d-spacing of the corresponding seeds of 0.195 nm, proving a lattice expansion due to hydride formation, and an average size distribution of 15.7 nm with standard deviation of 2.3 nm. On the other hand, Figure 3.7d-f show nanotetrahedra hydrides with a d-spacing of 0.23 nm which is higher than the d-spacing of the corresponding seeds of 0.223 nm, evidencing as well a lattice expansion due to hydride formation, and an average size distribution of 18.8 nm with standard deviation of 2.3 nm.

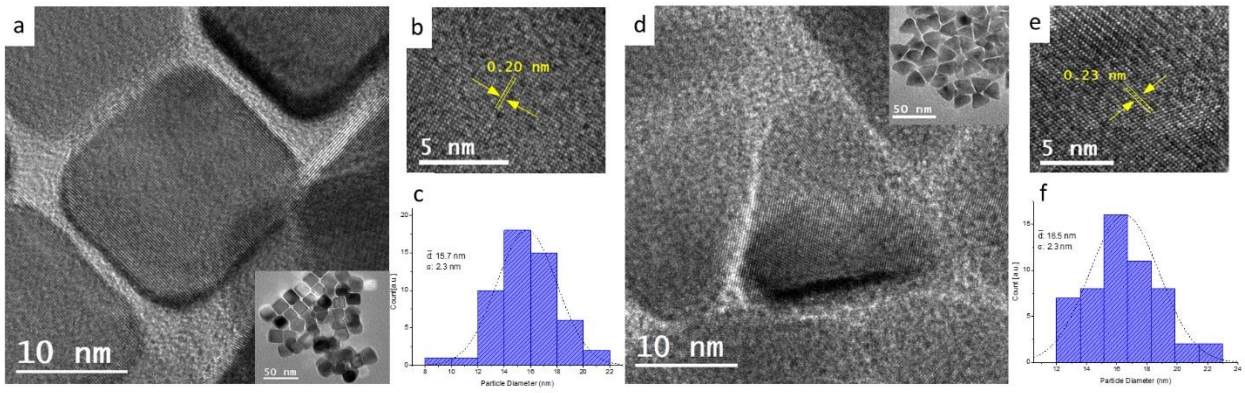

Figure 3. 7 HRTEM images of palladium hydride nanocrystals: a) PdHx Nanocubes capped with dodecanethiol at 10nm and 50nm (inset), b) HRTEM image at 5 nm with d-spacing of 0.20 nm, and c) nanoparticles size distribution based on TEM analysis with an average size of 15.7 nm and standard deviation of 2.3 nm; d) PdHx Nanotetrahedra capped with dodecanethiol at 10nm and

50nm (inset), e) HRTEM image at 5 nm with d-spacing of 0.23 nm, and f) nanoparticles size distribution based on TEM analysis with an average size of 18.8 nm standard deviation of 2.3 nm. Matlab was used for the size distribution analysis.

A complete size distribution of all the samples showed a decrease in their sizes while organic ligands are added to the surface of the nanocrystals. In fact, it is founded an inverse relation between crystal size and number of carbons chains of the organic compounds. Figure 3.8 shows these tendencies. Whereas the number of carbons in the organic compound increases, there is a reduction in the size of the nanocubes and tetrahedra for both functional groups, amines and thiols. However, it is founded that thiol group will lead to a much smaller nanocrystal sizes if compared with the amine group. In addition, it is observed that thiol groups act more effectively reducing the sizes of 100 facets rather than 111 facets, showing an attaching preference for 100 facets.

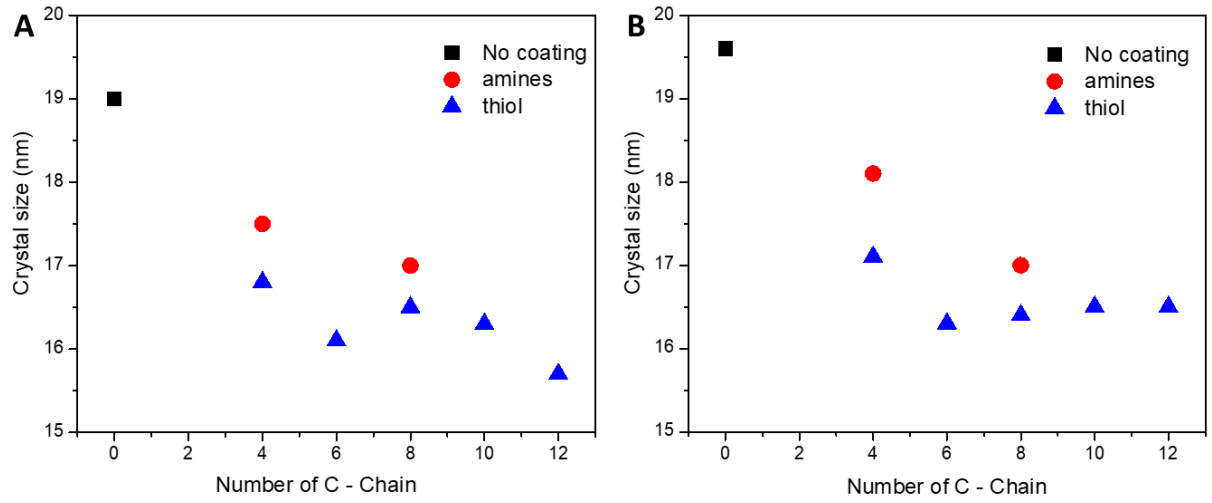

Figure 3. 8 Size distribution of A) Nanocubes and B) Nanotetrahedra of the synthesized samples coated with amine groups and thiol groups. Black squares represent palladium hydride samples without decorating the surface with the mentioned organic ligands.

Furthermore, to confirm β palladium hydride formation and as a mean to identify H:Pd ratio for all the synthesized samples, x-ray diffraction (XRD) analysis is employed as identification method of the phases and hydrogen concentration due to measurement of the lattice expansion as it has been stablished in previous literatures.[16–18] As shown in Figure 3.9 and Table 1, diffraction peaks of pure palladium nanocubes and tetrahedra appear at 40.0°, 46.5°, and 67.9° which are indexed as the (111), (200), and (220) planes of the Pd face-centered cubic (FCC) crystal structure. After DMF treatment and addition of the different organic ligands (amines and thiols) to their structures, lattice expansions are observed in all the samples. For instance, palladium hydride nanocubes surface decorated with 1-dodecanethiol exhibit a shift to lower angle of the (111) peak from 40.0° to 38.85°, indicating that the crystal lattice has increased suggesting that hydrogen was incorporated to its structure. These sample represent the higher hydrogen content achieved during this project and correspond to H:Pd ratio of around x = 0.58. The calculated H:Pd ratio are stablished due to comparison with previous literature values and in accordance with the Joint Committee on Powder Diffraction Standards (JCPDS) file, (JCPDS No. 18-0951).[16–18] Overall, nanocubes morphologies exhibit higher hydrogen storage capacity than their tetrahedra counterparts as it is observed in Figure 3.9 and Table 1.

Additionally, XRD analysis suggested that when amine group is used to surface decorate palladium hydride structure, its maximum H:Pd ratio values is of around x = 0.43, which is similar value as the sample obtained directly from the DMF treatment without no coating. Moreover, it is observed that as the number of carbon chain of amines is increased, there is a decrease in the hydrogen absorption capacity for both morphologies, nanocubes and tetrahedra.

Meanwhile, XRD analysis of thiol surface decorating nanocubes and tetrahedra showed that upon increase of carbon chain of the ligand, there is an increase in the hydrogen absorption capacity into palladium lattice. These observations are in accordance with the effect of thiols on nanocubes sizes as it was explained before. Besides, during the metallic hydride synthesis, thiol groups are added after 10 hours of DMF treatment of the samples, and then the reaction continue for the remaining 6 hours. Thus, a complete coverage of the surface is avoided from the beginning, allowing first the hydrogen uptake into the metal lattice to finally encapsulate the metallic hydride compound with thiol groups.

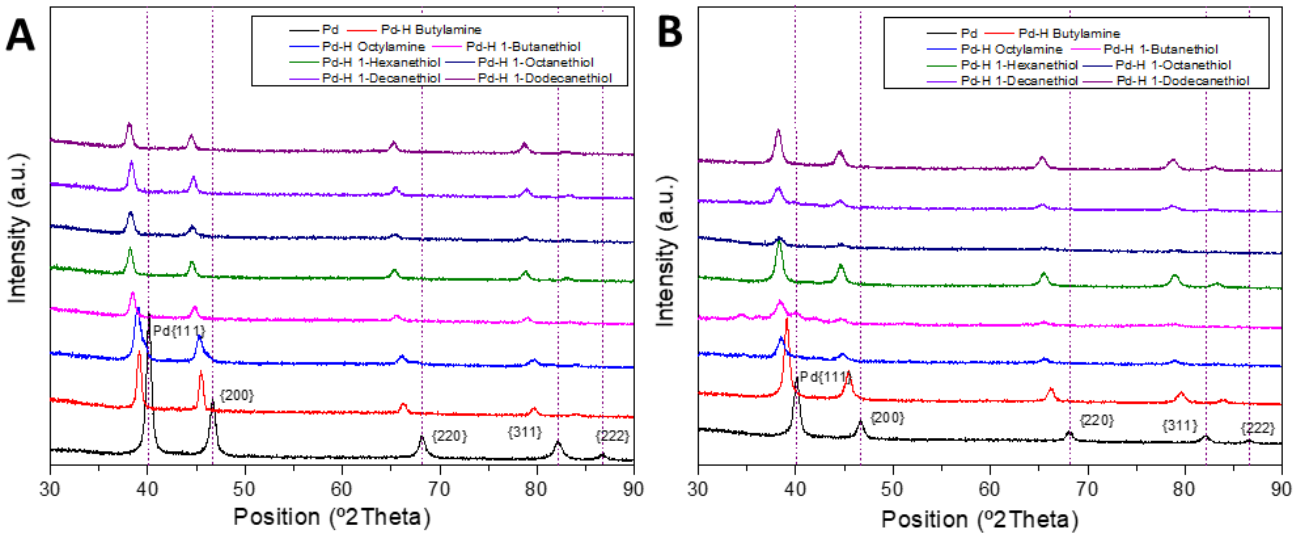

Figure 3. 9 XRD patterns of β Pd-Hx nanoparticles at different H/Pd ratios of (A) Nanocubes, and (B) Nanotetrahedra. Black lines represent pure palladium as a reference.

Table 3.1 XRD position, lattice parameter and H/Pd ratio data of nanocubes and tetrahedra hydride surface decorated samples

Morphology Type	Type of organic ligands	Position [°2Th.]	Lattice parameter	H:Pd ratio "x"
Pure Pd	----------	40.0	3.89	**0**
NC/Tetrahedra	----------	39.01	3.996	**0.43**
Nanocubes (100)	Butylamine	39.01	3.996	**0.43**
	Octylamine	39.08	3.989	**0.40**
	1-Buanethiol	38.91	4.006	**0.54**
	1-Hexanethiol	38.89	4.008	**0.55**
	1-Octanethiol	38.89	4.008	**0.55**
	1-Decanethiol	38.89	4.008	**0.55**
	1-Dodecanethiol	38.85	4.012	**0.58**
Tetrahedra	Butylamine	39.01	3.996	**0.43**
	Octylamine	39.15	3.982	**0.38**
	1-Buanethiol	39.17	3.980	**0.36**

(111)	1-Hexanethiol	39.17	3.980	**0.36**
	1-Octanethiol	39.15	3.982	**0.37**
	1-Decanethiol	39.14	3.983	**0.38**
	1-Dodecanethiol	38.99	3.998	**0.45**

Due to reduction of crystal sizes and higher hydrogen storage capacity observed in 100 facets, the following composition analysis and measurement of their properties are focused on nanocubes morphologies. In addition, samples of palladium hydride nanocubes synthesized with amines, thiol and no coating are presented in the following sections as comparison with thiol groups, and from all of them we take a special attention to PdH0.58 coated with 1-dodecanethiol.

X-ray photoelectron spectroscopy (XPS) was performed XPS on the samples. As mentioned before, we choose two types of nanocubes samples as examples of the determination of their oxidation states and as identification of the binding between amines and thiols onto palladium surface. Figure 3.10 shows two types of samples: the first sample is surface decorated with amine group (e.g. octylamine), and the second is surface decorated with thiol group (e.g. 1-dodecanethiol). From the next results, we can observe that peaks at the binding energy of palladium and nitrogen are presented when the nanoparticles are surface decorated with amines groups. Instead, when thiols groups are used as the capping agent, sulfur peak at its binding energy is observed; also, small peaks of nitrogen are also observed when thiols are used due to the

decomposition of the DMF during the synthesis of the nanoparticles. Therefore, it is possible to confirm the binding of sulfur and nitrogen to the surface of the palladium hydride.

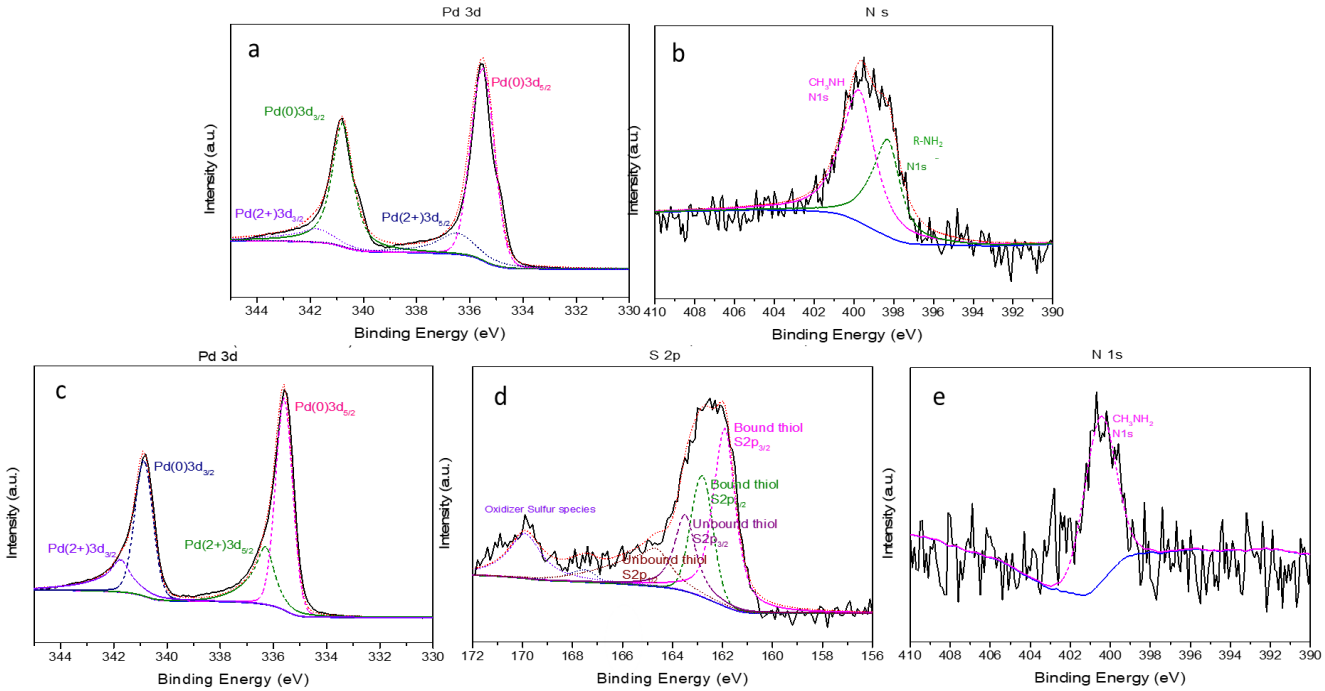

Figure 3. 10 XPS of a-b) PdH0.43 nanocubes capped with octylamine and showing (a) Pd 3d core lines (black line, red points, blue line, and pink, green, dark blue and purple segment lines correspond to raw data, sum, background, and $Pd^0(3d_{5/2})$, $Pd^{2+}(3d_{5/2})$, $Pd^0(3d_{3/2})$, $Pd^{2+}(3d_{3/2})$, correspondingly); (b) N 1s core lines presented on the sample due to existence of amine groups during the synthesis and surface decoration of PdHx nanoparticles (black, blue and segmented pink and green lines correspond to raw data, background, presence of methylamine CH_3NH_2 group on the surface of the metal hydride nanoparticles due to DMF solvent, and R-NH2 groups representing butylamine or octylamine used as capping agent during synthesis); (c-e) XPS of PdH0.58 capped with 1-dodecanethiol showing (c) Pd 3d core lines (black line, red points, blue line, and pink,

green, dark blue and purple segment lines correspond to raw data, sum, background, and $Pd^0(3d_{5/2})$, $Pd^{2+}(3d_{5/2})$, $Pd^0(3d_{3/2})$, $Pd^{2+}(3d_{3/2})$, respectively); (d) S 2p core lines presented on the sample due to surface coating with thiol group (black line, red points, blue line, and pink, green, purple, wine and brown segment lines correspond to raw data, sum, background, and bound thiol S ($2p_{3/2}$), bound thiol S ($2p_{1/2}$),oxidizer sulfur species, unbound thiol S ($2p_{3/2}$), and unbound thiol S ($2p_{1/2}$), respectively), and (e) N 1s core lines presented on the sample due to existence of amine groups during the synthesis of PdHx nanoparticles (black, blue and segment pink lines correspond to raw data, background and the presence of methylamine CH3NH2 group on the surface of the metal hydride nanoparticles).

Furthermore, if we compare core lines results of the palladium hydride decorated with amines and thiols with their corresponding palladium seeds (Figure 3.11a) is easy to observe a chemical shift of the palladium peaks $3d_{5/2}$ and $3d_{3/2}$ to a higher binding energy which indicates and confirms the formation of the palladium hydride alloy. In addition, valence band spectra is also analyzed with XPS and showed in Figure 3.11b where it is observed a decrease of the width of the peak upon an increase of hydrogen content which is also in agreement with previous research.[16] The valence band observed on the figure correspond to the electron-occupied d orbital of the metal.

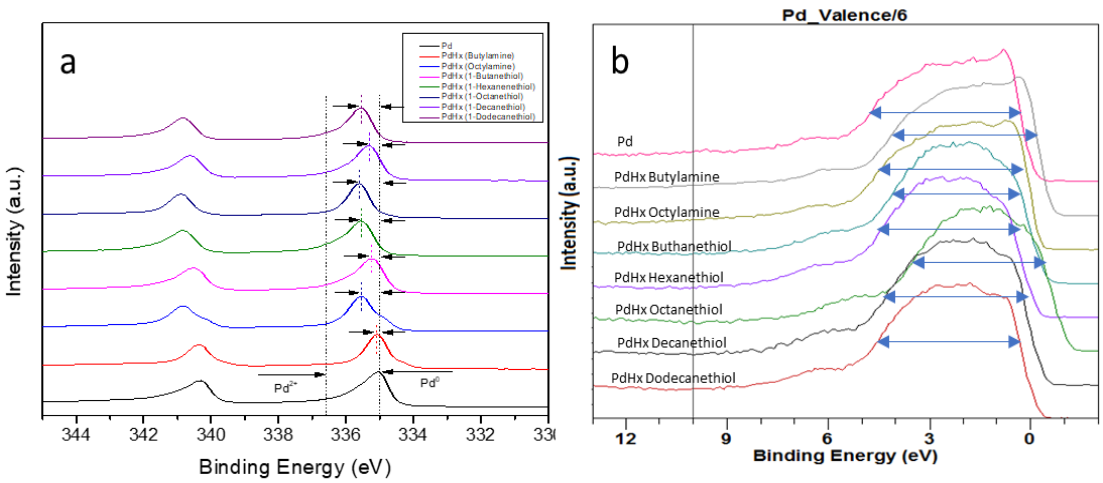

Figure 3. 11 XPS analysis data of PdHx Nanocubes (a) core lines and (b) valence band analysis respectively.

The following table summarizes the findings of the palladium hydride nanocube samples during XPS analysis.

Table 3.2 XPS Analysis of PdHx Nanocubes: core lines and valence band analysis

Surface Decoration (Type Amines/Thiol)	**Ratio H/Pd " x "**	**Core Lines Binding energy shift (eV)**	**Valence Band Structure (eV)**
Pd	----	0,00	4,19
Butylamine	0.43	0,25	3,78
Octylamine	0.40	0,24	3,77
1-Butanethiol	0.54	0,30	3,74
1-Hexanethiol	0.55	0,56	3,65
1-Octanethiol	0.55	0,60	3,62
1-Decanethiol	0.55	0,40	3,65
1-Dodecanethiol	0.58	0,60	3,58

Finally, it was found that PdHx nanocubes surface decorated with thiols exhibit ferromagnetic properties. Pure palladium and palladium hydride without coating agents behave as pure paramagnetic materials. Therefore, it is concluded that the properties of the hydrides can be tuned by adding certain organic molecules as thiol groups to the surface of the metal host. Thus, Superconducting Quantum Interference Device Magnetometer (SQUID) were used to analyze the magnetic properties of the material. M(H) measurements were used to analyze hysteresis curves by changing the applied magnetic field and maintaining constant the temperature. M(H) isotherms were taken at 25K, 50K, 65K, 75K, 100K, 150K, 200K, and 300K in the field range -2000

Oe≤H≤2000 Oe.. Figure 3.12 show the hysteresis curves during magnetization test of the palladium hydride nanocubes sample surface decorated with 1-dodecanethiol.

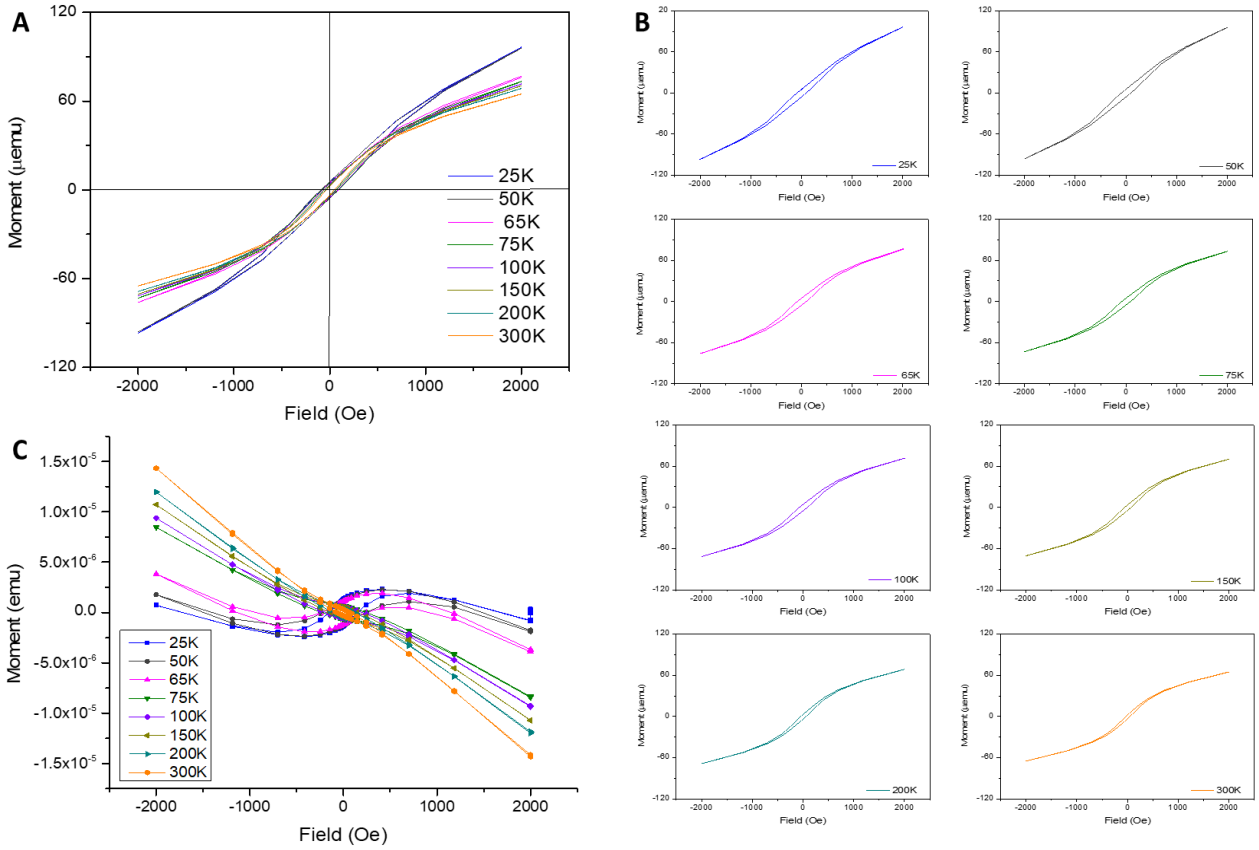

Figure 3. 12 Magnetization Measurements M(H) of Palladium hydride nanocube ($PdH_{0.58}$) with 1-dodecanethiol (DD-SH) as a capping agent. (A) at different temperatures 25K, 50K, 65K, 75K, 100K, 150K, 200K, 300K. The magnetization curves show typical ferromagnetic hysteresis. (B) individual curves of the temperatures tested in (A), and (C) raw data of the sample before the subtraction of the diamagnetic signal of the plastic holder (straw and plastic capsule).

Moreover, Figure 3.13 illustrate the extracted magnetization per mass from the data obtained in Figure 3.12. As a reference, Figure 3.13B shows the typical magnetizations for the different magnetic materials as ferromagnetic, paramagnetic and antiferromagnetic materials.

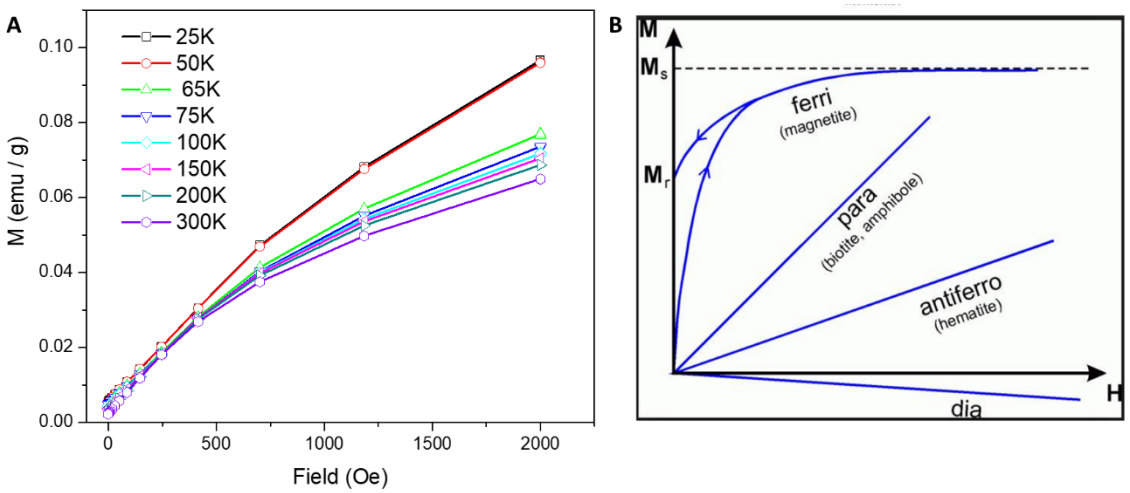

Figure 3. 13 (A) Magnetization (per mass) of palladium hydride nanocube sample ($PdH_{0.58}$) surface decorated with 1-dodecanthiol for all the temperatures tested, and (B) Reference of the magnetization for the typical materials.

The observed magnetic results are in accordance with previous studies of metals with surface decoration with thiol groups. For instance, studies of thiol capped gold nanoparticles have been performed previously, and were found to have intrinsic spin polarization arising from the interaction between the surface of gold atoms and the thiol ligands attached.[19] Similar behavior has been observed on Pd atoms using alkene-thiols as capping agents forming covalent bonding with Pd nanoparticles stabilizing permanently the ferromagnetic behavior by increasing the density of states near the Fermi level, leading to permanent magnetism in this nanoparticles even at 300K,[20,21] which is consistent with observations made on Pd nanoparticles where is claimed that

magnetic properties is strongly influence by interactions of surface atoms with ligands, forming covalent bond in a charge transfer mechanism that explains the increase of the density of states (DOS) in the 4d band of Pd, leading to a permanent magnetism for Pd nanoparticles.[21] Moreover, it has been claimed that ferromagnetic ordering occurs only on the (100) facets of their Pd nanoparticles, retaining permanent magnetism even above 300K which is in agreement with our observations where ferromagnetism is only observed in nanocubes and no in tetrahedra shapes.[22] Additionally, it has been reported a direct relation between the ratio of Pd:thiol as a mechanism to control the size of nanoparticles[20], which at the end will represent an increase in hydrogen storage due to increase of surface area. To explain these phenomena, a core/shell structure was proposed where the ferromagnetism is associated with surface atoms while the core still remains paramagnetic as it is stablished in previous reports.[21] Thus, our findings of ferromagnetic palladium hydride open a new exploration path towards tailoring magnetism properties of PdHx nanomaterials.

Moreover, the synthesized β palladium hydride nanocubes surface decorated with amines groups, as well as the nanocubes with no capping ligand do not exhibit ferromagnetism, but instead they present a paramagnetic behavior. For instance, Figure 3.14 (B) shows that palladium hydride ($PdH_{0.43}$) with no coating, remains mostly paramagnetic as in the same manner as pure palladium. Figure 3.14 (A) shows the diamagnetic signal obtained from the sampler holder which consist of a plastic straw, a plastic capsule for the sample and adhesive layer. The diamagnetic signal from the holder is analyzed for each temperature tested in the samples, and it is subtracted from the signal of the palladium hydride samples.

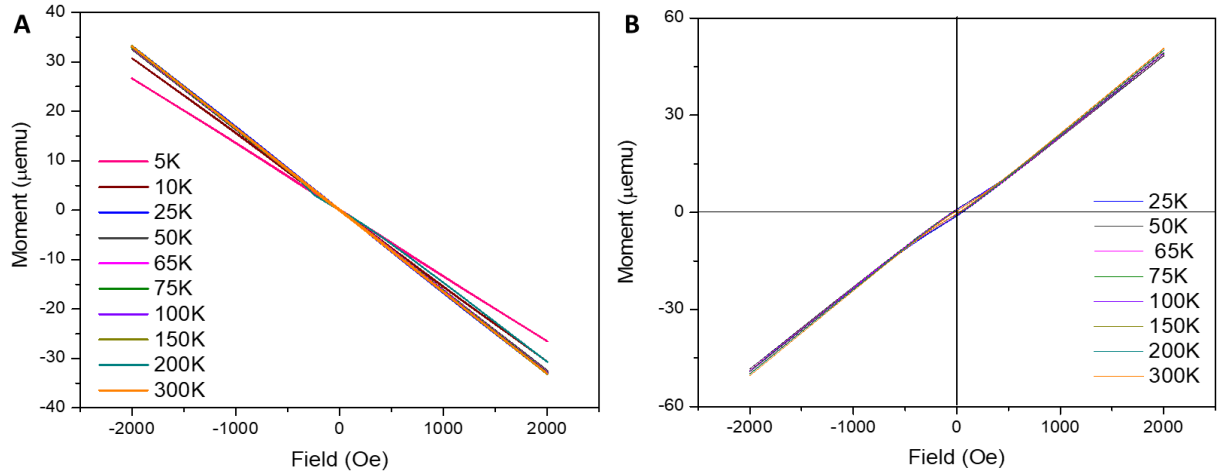

Figure 3. 14 Magnetization measurements M(H) of (A) sample holder (straw, plastic capsule and adhesive) and (B) palladium hydride nanocubes with no coating sample ($PdH_{0.43}$) at different temperatures 25-300K.

Finally, it can be concluded that palladium hydride surface decorated with thiol samples pass from a strong paramagnetic behavior of pure Pd to a ferromagnetic behavior. These particular behaviors can be explained in terms of a charge transfer mechanism due to a covalent bond of Pd atoms with the protective thiol ligands which will also increase the 4d density of states of Pd atoms as it was mentioned before. Materials showing permanent magnetism are of great interest in data storage devices due to their contribution in an increment in the memory density.[20] Thus, our nanocubes with magnetic properties are remarkable different from their bulk counterparts.

3.3 Conclusion

In Summary, we have developed in a simple way an efficient synthesis of palladium hydride nanoparticles with controllable size and ratios, being able to tune its properties. Based on the rational design, stable β-PdHx with hydrogen ratios, up to x~0.6 were obtained by utilizing the in situ produced hydrogen gas from the catalytic decomposition of the DMF, and surface decorating with capping agents as amines and thiols which are responsible of the multi-faceted properties of the materials.

Moreover, we found that hydrogen storage in the palladium nanoparticles increase with increasing chain length of organic ligands acting as capping agent for palladium surface, and subsequently decrease the size of the nanoparticles. In addition, we have investigated the magnetic properties of alkyl amines and alkyl thiol surface decorating β-Palladium hydride nanoparticles having different morphologies and compared them with their palladium hydride without surface decoration and Pd nanoparticles counterparts. These finds give hope to continue finding prospects to achieve hydrogen storage materials with the ability of tune of their properties at even room temperature and pressure.

3.4 Experimental Methods

Chemicals and materials. Palladium (II) acetylacetonate [$Pd(acac)_2$ (99%)], Molybdenum hexacarbonyl [$Mo(CO)_6$] was purchased from Alfa Aesar. N,N-Dimethylformamide(DMF), AND Acetone were purchased from Fisher Scientific. Sodium tetrachloropalladate [Na_2PdCl_4], n-Octylamine, n-Butylamine, 1-Buthanethiol, 1-Hexanethiol, 1-Octanethiol, 1-Decanethiol, 1-

Dodecanethiol, Formaldehyde (37% solution), L-ascorbic acid, Potassium bromide, and Poly (vinylpyrrolidinone) (PVP, Mw≈40000) were purchased from Sigma Aldrich. Ethanol was purchased from EMD chemical.

Synthesis of Nanostructures. For the synthesis of the nanoparticles seeds for nanocubes and nanotetrahedra, we followed and modified a previous method.[16] In a typical process, palladium nanotetrahedra and nanocubes were synthesized as follow:

Synthesis of palladium nano-tetrahedra. 30 mg $Pd(acac)_2$, 50 mg PVP were dissolved in 10 mL DMF in a 25 mL glass vial. Then, 0.1ml of formaldehyde solution (37%) was added into the solution with 2 mg $Mo(CO)_6$. The vial was kept at 160 ºC in oil bath for 4 h.

Synthesis of palladium nanocubes. 60 mg L-ascorbic acid, 600 mg KBr and 80 mg PVP were dissolved in 8.0 mL of water in a 25 ml vial. The mixture was heated in an oil bath at 80 ºC for 10 min. Separately, 57 mg Na_2PdCl_4 was dissolved in 3 ml water and then added into the first vial. The reaction was kept at 80ºC in an oil bath for 3h.

Synthesis of palladium hydride polycrystal nanoparticles. 8 mg $Pd(acac)_2$ were dispersed in 10 mL of DMF in a 25 mL glass vial. To this mixture, 100 μL of Amines (n-Butylamine, n-Octylamine) or Thiols (1-Buthanethiol, 1-Hexanethiol, 1-Octanethiol, 1-Decanethiol, 1-Dodecanethiol) were added to the vial. The reaction took place in an oil bath heated at 140 ºC for 4 h.

Synthesis of nanocubes palladium hydride particle. After the preparation of fresh palladium nanocubes seeds, the material was washed with ethanol, acetone and DMF several times. Finally, the seeds were collected by centrifuge and dispersed in DMF for next step.

Second step: 2 mg Pd nanocubes seeds were dispersed in 10 mL DMF, 100 μL Amines (n-Butylamine, n-Octylamine) were added to the solution, and then heated at 140 ºC for 16 h. In the case of thiol ligands, 100 μL of Thiols (1-Buthanethiol, 1-Hexanethiol, 1-Octanethiol, 1-Decanethiol, 1-Dodecanethiol) were added after 10 h of the reaction and kept at the same onditions for 6 h.

Synthesis of nanotetrahedra palladium hydride particle. In the same way of nanocubes, hydride nanotetrahedra were synthesized by using the fresh prepared nanotetrahedra seeds that were previously dispersed in DMF.

Second step: 2 mg Pd nanotetrahedra seeds were dispersed in 10 mL DMF, 100 μL Amines (n-Butylamine, n-Octylamine) were added to the solution, and then heated at 140 ºC for 16 h. In the case of thiol ligands, 100 μL of Thiols (1-Buthanethiol, 1-Hexanethiol, 1-Octanethiol, 1-Decanethiol, 1-Dodecanethiol) were added after 10 hours of the reaction and kept at the same conditions for 6 h.

Post Synthesis Treatment. The resulted products were collected, washed and centrifuged around 3 times with Acetone, DMF, and finally ethanol.

Characterization. Transmission electron microscopy (TEM) images were taken on a FEI T12 operated at 120 kV. High resolution TEM images (HR-TEM) was taken on a FEI TITAN operated at 300 kV. Samples for TEM measurements were prepared by dropping 10-20 μL of the respective

nano samples in ethanol dispersed onto a carbon coated copper grids (Ted Pella, Redding, CA) for TEM images. Powder X-ray diffraction patterns (PXRD) were collected on a Panalytical X'Pert Pro X-ray Powder Diffractometer with Cu-Kα radiation. The compositions and oxidation states were checked by X-ray photoelectron spectroscopy (XPS) on a K-Alpha XPS spectrometer (ThermoFisher, E.Grinstead, UK) with Al Kα X-ray radiation (1486.6 eV) for excitation.

Properties of the materials were analyzed by using UV-VIS measurements were recorded in the 200-1100 nm region on a Beckman Coulter DU 800, RAMAN spectroscopy data were collected using a 488 nm excitation laser, Superconducting Quantum Interference Device Magnetometer (SQUID) were used to analyze the magnetic properties of the material. Two measurement were performed using SQUID: a) M(T) curves were performed by using ZFC Zero Field Cooling and b) M(H) to perform the hysteresis curves by changed the applied magnetic field and maintaining constant the temperature.

3.5 References

1. Yang, X., Li, H., Ahuja, R., Kang, T. & Luo, W. Formation and electronic properties of palladium hydrides and palladium-rhodium dihydride alloys under pressure. *Sci. Rep.* **7,** (2017).
2. Houari, A., Matar, S. F. & Eyert, V. Electronic structure and crystal phase stability of palladium hydrides. *J. Appl. Phys.* **116,** (2014).
3. Kumara, L. S. R. *et al.* Hydrogen storage and stability properties of Pd–Pt solid-solution nanoparticles revealed via atomic and electronic structure. *Sci. Rep.* **7,** 14606 (2017).
4. Yamauchi, M., Ikeda, R., Kitagawa, H. & Takata, M. Nanosize effects on hydrogen storage in palladium. *J. Phys. Chem. C* **112,** 3294–3299 (2008).
5. Soldatov, A. V., Della Longa, S. & Bianconi, A. Relevant role of hydrogen atoms in the XANES of Pd hydride: Evidence of hydrogen induced unoccupied states. *Solid State Commun.* **85,** 863–868 (1993).
6. Klotz, E. & Mattson, B. Hydrogen and palladium foil: Two classroom demonstrations. *J. Chem. Educ.* **86,** 465–469 (2009).
7. Ferguson, G.A., Schindler, A.I., Tanaka, T., Morita, T. Neutron Diffraction Study of Temperature-Dependent Properties of Palladium Conatainінf Absorbed Hydrogen. *Phys. Rev.* **137,** A483–A487 (1965).
8. Zalineeva, A., Baranton, S., Coutanceau, C. & Jerkiewicz, G. Octahedral palladium nanoparticles as excellent hosts for electrochemically adsorbed and absorbed hydrogen. 1–11 (2017).
9. Schneemann, A. *et al.* Nanostructured Metal Hydrides for Hydrogen Storage. *Chem. Rev.* 10775–10839 (2018).

10. Chen, Y. *et al.* Electronic origin of hydrogen storage in MOF-covered palladium nanocubes investigated by synchrotron X-rays. *Commun. Chem.* **61,** 1–8 (2018).

11. Lewis, F. A. *The Palladium/Hydrogen System*. (Academic Press, 1967).

12. Johnson, N. J. J. *et al.* Facets and vertices regulate hydrogen uptake and release in palladium nanocrystals. *Nat. Mater.* **2,** (2019).

13. Huang, X. *et al.* Synthesis of PtPd bimetal nanocrystals with controllable shape, composition, and their tunable catalytic properties. *Nano Lett.* **12,** 4265–4270 (2012).

14. Li, G. *et al.* Shape-Dependent Hydrogen-Storage Properties in Pd Nanocrystals: Which Does Hydrogen Prefer, Octahedron (111) or Cube (100)? *J. Am. Chem. Soc.* 10222–10225 (2014).

15. Zalineeva, A., Baranton, S., Coutanceau, C. & Jerkiewicz, G. Octahedral palladium nanoparticles as excellent hosts for electrochemically adsorbed and absorbed hydrogen. *Sci. Adv.* **3,** 1–11 (2017).

16. Zhao, Z. *et al.* Synthesis of Stable Shape-Controlled Catalytically Active β-Palladium Hydride. *J. Am. Chem. Soc.* **137,** 15672–15675 (2015).

17. Lu, Y., Wang, J., Peng, Y., Fisher, A. & Wang, X. Highly Efficient and Durable Pd Hydride Nanocubes Embedded in 2D Amorphous NiB Nanosheets for Oxygen Reduction Reaction. *Adv. Energy Mater.* **7,** 1–7 (2017).

18. Fujii, K. *et al.* Relationship between element-selective electronic states and hydrogen absorption properties of Pd- M (M = Ru , Rh , Ag , and Au) alloys. *Phys. Rev. B* 024116(1)-024116(7) (2017).

19. Yamamoto, Y. & Hori, H. Direct observation of the ferromagnetic spin polarization in gold nanoparticles: A review. *Rev. Adv. Mater. Sci.* **12,** 23–32 (2006).

20. Hernando, A. *et al.* Room temperature permanent magnetism in thiol-capped Pd-rich nanoparticles. *Nanotechnology* **17,** 1449–1453 (2006).

21. Angappane, S., Park, J., Jang, Y., Hyeon, T. & Park, J. G. Magnetic Pd nanoparticles: Effects of surface atoms. *J. Phys. Condens. Matter* **20,** (2008).

22. Shinohara, T., Sato, T. & Taniyama, T. Surface Ferromagnetism of Pd Fine Particles. *Phys. Rev. Lett.* **91,** 197201 (2003).

Chapter 4

4 Palladium Copper Intermetallic Nanowires Enabling Enhanced Electrocatalysis

4.1 Introduction

Renewable energies for supplying high energy with low pollutant emissions are imperative for developing cleaner technologies to migrate from fossil fuel-based energies. Hydrogen is globally known as a future green fuel source leading to zero carbon dioxide emissions and higher energy content than carbon based fuels.[1] Hydrogen generation can be accomplished by natural gas reforming or electrochemically where hydrogen (H_2) is generated at an applied potential (U) in the presence of an electrocatalyst.[2–5] To enhance the kinetics toward the hydrogen evolution reaction (HER) the catalyst must induce proton reduction with minimal overpotential (η), high faradaic efficiency, and have fast kinetics.[6,7] HER, the cathodic reaction in electrochemical water splitting, is accompanied by adsorption of hydrogen (*H) on the electrode surface and its reaction to form H_2, which can be enhanced by metal alloy nanostructures. Likewise, formic acid is suggested as a fuel to be employed in direct formic acid fuel cells (DFACFC) operating at low temperatures. The Formic acid oxidation reaction (FAOR) is the anodic reaction in DFACFC that exhibits advantages in terms of lower crossover flux through Nafion membranes compared with methanol fuel cells providing a nontoxic and nonflammable alternative. Together offering additional routes for clean energies where a catalyst with enhanced electrocatalytic activity, durability, cost-efficiency, low overpotentials, and fast kinetics must be addressed to achieve practical applications.[6,8]

Pt based materials are optimal catalysts for reactions as HER. Nevertheless, their scarcity and lack of electrode stability under strongly acidic conditions make them unsuitable for large scale applications for different types of fuel cells.[1,3] Thus, other suitable catalysts pathways are needed with high catalytic activity for various energetic reactions over a wide pH range. Rational design with compositional and morphology tuning are needed to achieve the goal.[9,10] Palladium based materials and alloys with transition metals (e.g. Cu, Ni, Co, Fe, Ru) provide an attractive approach to find candidates for such catalytic reactions as HER and FAOR due to their higher or similar catalytic properties and higher abundancy than Pt based materials.[1,2,10–16] These properties plus low CO poisoning effects of Pd based materials combined with poison resistant transition metal hosts (e.g. Cu, Ag, Au, Ni)[15,17] make them feasible for cheaper effective use in various applications for fuel cells, and in other oxidation-reduction reactions.[1,3,11,18,19]

Nanoparticles Palladium and its alloys have been widely studied as the prefered form (zero dimension-0D) due to their high surface area. Yet, poor stability and sintering affect their catalytic performance.[2,11] One dimensional (1D) nanomaterials, on the other hand, present good stability while preventing agglomeration. Moreover, the interconnected nature of 1D nanostructures, increases electrical conductivity significantly compared with nanoparticle counterparts.[11,19,20] Yet, their synthesis remains a challenge because growing the atoms into nanowires does not have an intrinsic driving force.[9,11,14,20] Previous studies suggested complex combination of 0D and 1D nanomaterials to boost their catalytic activities. For instance, copper–platinum (Cu-Pt) alloy with one dimensional structure of palladium nanorings (Pd NRs) proved to be excellent catalysts for HER in acidic solution, exhibiting an overpotential of only 22.8 mV at a current density of 10 mA/cm^2 , which is comparable with commercial Pt.[21] Likewise, Li and coworkers proved

experimentally that Cu@Pd core shell nanowires with diameter around 30-40 nm, and CuPd nanoparticles on perovskite-type $WO_{2.72}$ nanorods showed enhanced activity and stability for FAOR with mass activities of around 2200 mA/mg_{Pd}, being superior than those from CuPd nanoparticles and commercial Pd.[9,14]

Beyond Pd-based alloy (disordered) materials, other compounds with high ordering as intermetallic compounds have been explored for higher efficiencies. Intermetallic compounds can exhibit ordering between atoms, in this case Pd with a transition metal (e.g. M = Cu), in which every crystallographic site is occupied by a specific atom.[16] Intermetallic compounds suggest electrochemically advantages against other materials, arising from the strong bonding between Pd and M to induce long term stability to avoid deactivation.[16,22] However, their synthesis remains a challenge. Different examples can be found in the literature for intermetallic nanostructures, yet most referring only to nanoparticles with little evidence for intermetallic nanowires.[22–27] Pt_3Co and Pd_3Pb intermetallic nanowires are among the few studies known, which indeed improved activities towards the oxygen reduction reactions (ORR) and alcohol oxidation reactions.[28,29] Nonetheless to the best of our knowledge, PdCu nanowires (1D) of alloy (A1) and compressed intermetallic (B2) phases have not previously been synthesized or explored for application in catalytic reactions such as HER and FAOR over a wide pH range to show enhanced catalytic activities.

Herein, we report the synthesis of ultrathin palladium copper alloy nanowires (PdCu NWs) with an average diameter of 5nm, followed by their transformation from alloy to intermetallic compound through electrochemical dealloying (leaching) to induce the rearrangement of Pd and

Cu atoms to form intermetallic nanowires, denoted as *PdCu NWs, that lead to high catalytic activity for HER at low overpotentials. On the other hand, the synthesized alloy PdCu NWs present superior electrochemical surface area (ECSA) and enhanced HER compared with pure palladium nanowires (Pd NWs). Nevertheless, their ordered counterpart, *PdCu NWs intermetallic compound exhibits superior performance for HER in acidic and alkaline media at lower overpotential, lower Tafel slope, and high ECSA compared with their alloy counterpart, Pd NWs and comparable to commercial Pt/C. Moreover, *PdCu nanowires present higher mass activities during FAOR among all the materials studied, which is almost seven times higher than Pd/C.

4.2 Results and Discussion

PdCu alloy nanowires networking is obtained from the reduction of dihydrogen tetrachloropalladate (H_2PdCl_4) and copper (II) chloride ($CuCl_2$) in the presence of $NaBH_4$, mixed in water solution containing Triton X-100 (0.2% v/v). Pd and Cu reduced species arise and aggregate together to form PdCu nuclei. Simultaneously, hydrogen bubbles are generated due to the hydrolysis of $NaBH_4$. The hydrogen generation directs the growth of PdCu nuclei towards metallic nanocrystals formation around the hydrogen bubbles in a diffusion controlled process where self-assemble and oriented growth of nanowires occur as in agreement with previous findings. [34,35] Finally, an interconnected nanowires network is created. Figure 4.1 describes the formation mechanism of the PdCu NWs network. The synthesized networking of PdCu alloy nanowires were collected by centrifuge and washed five times with ethanol/water.

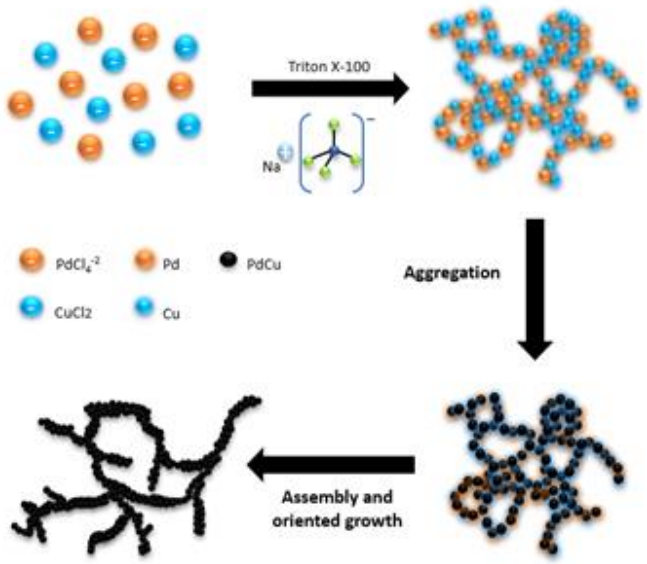

Figure 4. 1 Schematic illustration of the formation of PdCu nanowires

Transmission electron microscopy (TEM) images in Figure 4.2A shows the networking of PdCu nanowires created during their synthesis, while atomic resolution high angle annular dark field (HAADF) scanning transmission electron microscopy (STEM) images in Figure 4.2B and C suggest that Pd and Cu are forming an alloy of disordered structure or phase A1 indicated by a d-spacing of 0.222 nm ± 0.001 corresponding to the (111) interplanar distance which translate into a lattice parameter of around 0.3849 nm based on face centered cubic (fcc) structure. In the same standpoint, energy dispersive spectroscopy (EDS) mapping (Figure 1D-G) shows clearly the well distribution of Pd atoms along the nanowires structures as well as Cu atoms, being these concentrated at the junctions and tips of the nanowires. The alloy nanowires have an average of their body and tips/junctions diameter of 3.5 nm ± 0.8 and 5 nm ± 0.9 respectively, being wider at their tips and junctions overall. Pan powder x-rays diffraction (XRD) studies also confirm the alloy formation with a lattice parameter of about 0.3850 nm which match with reference pattern ICSD

A1: 628694 for PdCu alloy (Figure 4.2H). The overall atomic ratios extracted from the different characterization techniques as scanning electron microscopy – EDS plus approximation to Vegard's law from d-spacing of HR-TEM images and XRD studies suggest a composition of around $Pd_{85}Cu_{15}$. Inductively coupled plasma atomic emission spectroscopy (ICP-AES) confirms a weight percentage composition of 83.8% Pd and 16.2% Cu for the alloy nanowires. Furthermore, x-ray photoelectron spectroscopy (XPS) reveals a major signal for metallic palladium rather than oxidizer species whereas copper spectra presents metallic species only, having an absence of oxidation peaks for a final percentage composition of 83.9% Pd and 16.1% Cu which overall suggests that Cu atoms were incorporated into the Pd lattice to form PdCu alloy.[1,29]

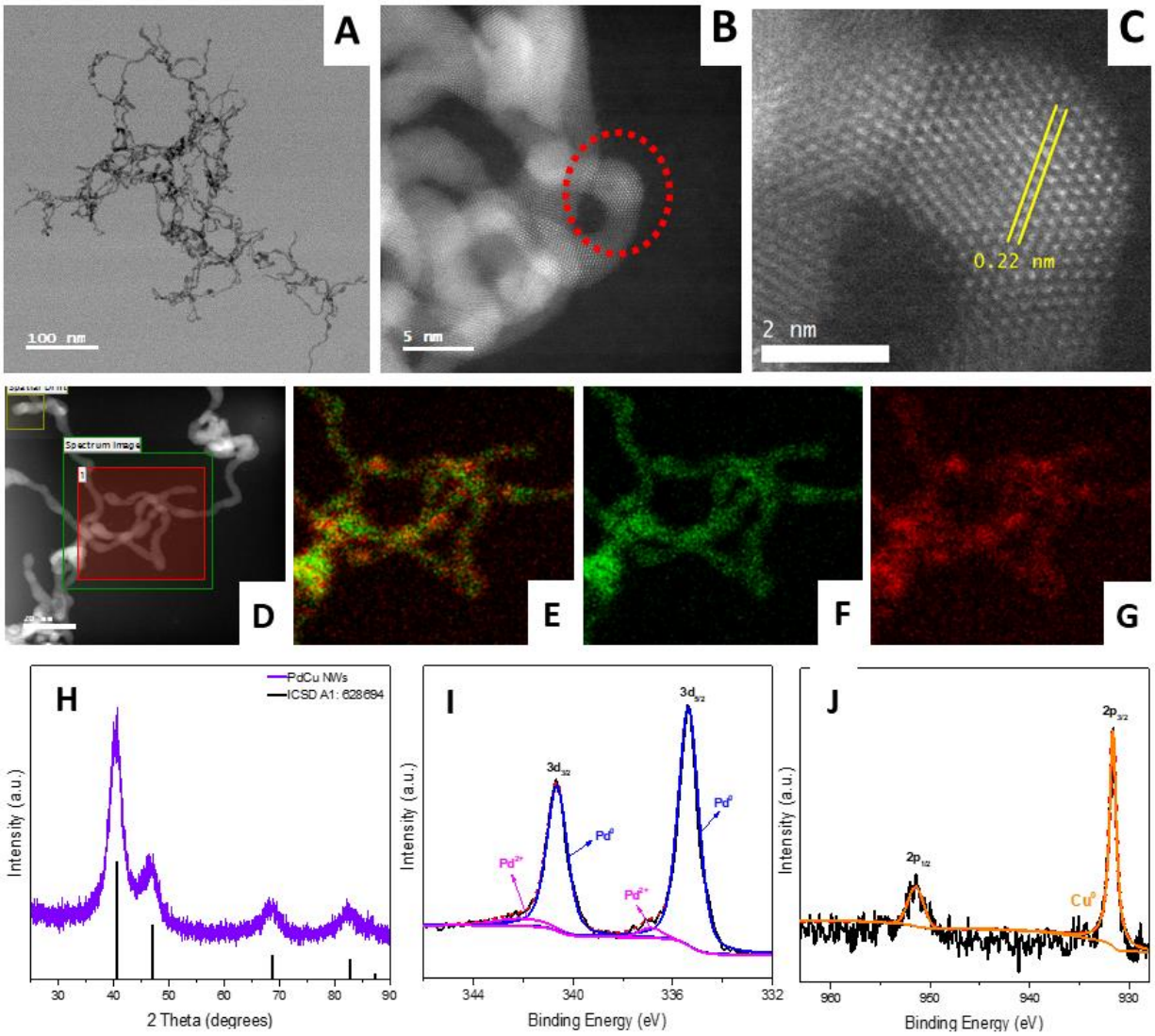

Figure 4. 2 PdCu alloy nanowires (A) TEM image. (B, C) HAADF STEM images, red circle showing the area zoomed in C. (D-G) HAADF STEM images taken for EDS mapping of (E) PdCu overlapping map, and individual mapping for (F) Pd and (G) Cu. (H) XRD spectra of PdCu alloy nanowires, black lines represent the standard peak positions of PdCu alloy phase A1 (ICSD A1: 628694). (I, J) XPS spectra showing palladium and copper binding energy of PdCu alloy nanowires respectively.

An electrochemical dealloying (leaching) process in acid media was used to gradually modify the structure of the alloy nanowires, which allowed the rearrangement of Pd and Cu atoms to a more ordered structure (B2 - intermetallic phase). We first conducted cyclic voltammetry (CV) in N_2-saturated 0.5M H_2S0_4 (0.05 V to 1.1 V versus RHE - reversible hydrogen electrode) with a sweep rate of 100 mVs^{-1} on PdCu alloy nanowires. Immediately after it, chronopotentiometry test was performed on the sample at a constant current of 2 mA and at a constant rotation disk of around 1600 r.p.m for 10 hours. Hydrogen evolution reaction was used to test the catalytic activity of the material after the dealloying process. Results showed a superior performance at lower overpotentials of the new material if compared with their initial sample, and even higher than Pt/C commercial. The new material showed an overpotential of 19.7 mV at 10 mA/cm^2 against 19.2 mV and 41.3 mV of Pt/C and PdCu alloy (vs. RHE) (Figure 4.6A–F, Table 4.1). All these results are discussed later in detail.

Further characterization studies on structure and composition were carried on the sample. Low-resolution TEM images in Figure 4.3A showed the preserved interconnected structure of nanowires, however, the overall longitude and diameter of the nanowires changed from the initial PdCu alloy nanowires. Size distribution analysis proved that the overall structure of the processed nanowires got wider in around 2 nm after the dealloying process if compared with their initial structure (Figure 4.3A, B) provoking swelling at the tips and junctions. Extraordinarily, HRTEM and HAADF STEM images in Figure 4.3B and C suggest the appearance of an ordered B2 phase with a typically d-spacing of around 0.205 nm ± 0.012 corresponding to (110) plane, and 0.289 nm ± 0.002 corresponding to (100) plane. Moreover, atoms rows with different contrast (Figures 4.3C) are clearly observed from the HRTEM and HAADF STEM images which confirms the

reordering of the Pd and Cu atoms during the electrochemical dealloying. This contrast observed in different rows, and which suggest the presence of intermetallic compound is in agreement with previous reports.[31,33,36] The ordered phase in our new material is mostly observed at the tips and junctions of the nanostructures (Figure 4.4).

EDS mapping (Figure 4.3D-G) of the processed sample shows a clearly well distribution of Pd atoms along the nanowires structure while Cu atoms were found to be more concentrated at the junctions and tips of the nanowires in a similar manner as the initial alloy sample. Further analysis was performed on the processed material. XRD studies in Figure 4.3H confirmed the presence of B2 phase and A1 phase in the structure of the nanowires which are compared to patterns cards ICSD 628694 (PdCu alloy A1 phase) and ICSD 181913 (PdCu intermetallic compound B2 phase). XRD peaks observed at around 30.2 and 44.1 degrees correspond to (100) and (110) planes of a typically B2-phase while a peak around 40.4 degrees suggest (111) plane for A1-phase.

We further performed a more detail study of the processed sample in which HRTEM and HAADF STEM images (Figure 4.4) proved that the ordered structure is mostly found at the tips and junctions of the nanowires while the body remains in A1 phase based on the d-spacing results. Moreover, EDX spectroscopy line scan and mapping analysis of the ordered areas (e.g. tips of nanowires) suggested a percentage composition of $Pd_{56}Cu_{44}$ which agrees with HRTEM and HAADF STEM studies. Finally, XPS analysis of the nanowires sample suggest that metallic Pd and Cu are the major species present in the new ordered structure as it is observed from their peaks in Figure 4.3I and J respectively. In fact, Pd metallic and oxidation species are around 96% Pd^0

and 4% Pd^{2+} showing less oxidize percentage if compared with their initial alloy sample of around 93% Pd^0 and 7% Pd^{2+}**.** Therefore, it is revealed more intermetallic state in the ordered phase based on the fitted curve implying that metallic Pd^0 is predominant. In the same way, Cu^0 metallic species are the only ones observed during the XPS analysis of the sample where absence of Cu oxidizer peaks is noted.[37] Additionally, binding energies of palladium for the disordered and ordered PdCu nanowires are shifted to higher energies than pure palladium reported in literature if we compared them based on metallic $Pd^0_{3d5/2}$ peak.[20] For instance, we observed that $Pd^0_{3d5/2}$ binding energy of PdCu intermetallic compound and PdCu alloy are around 335.4eV and 335.3eV respectively, compared to 335.1eV for bulk Pd which indicates that electrons in PdCu with ordered phase are a little more rich than those in PdCu alloy and both much richer than those in pure Pd and in agreement with previous literature.[8,20] On the bases of these observations, we designate the new ordered structure as *PdCu NWs (Figure 4.3).

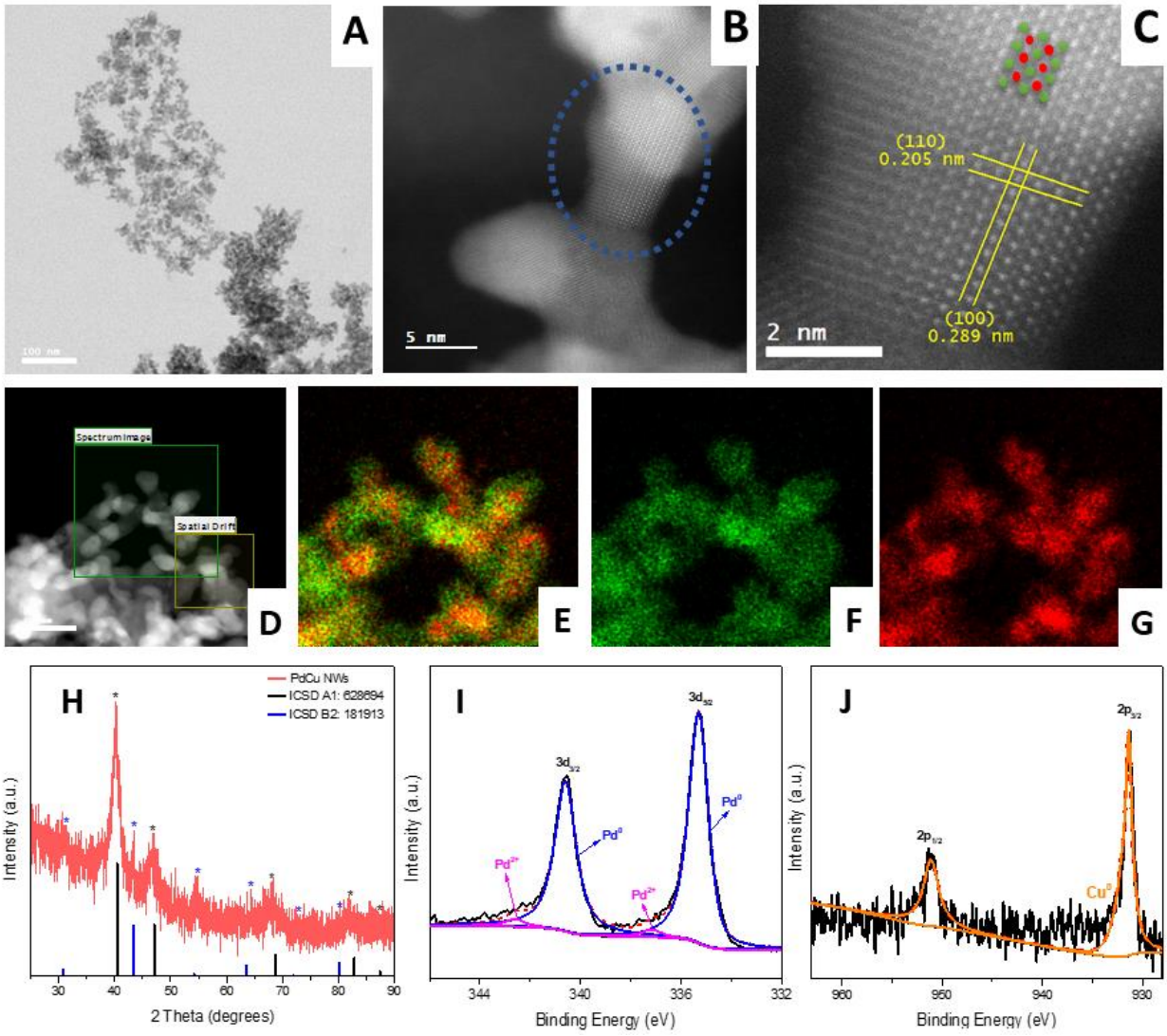

Figure 4. 3 *PdCu nanowires (A) TEM image. (B, C) HAADF STEM images, blue circle showing the area zoomed in C. (D-G) HAADF STEM images taken for EDS mapping of (E) PdCu overlapping map, and individual mapping for (F) Pd and (G) Cu. (H) XRD spectra of *PdCu nanowires, black lines represent the standard peak positions of PdCu alloy phase A1 (ICSD A1: 628694) whereas blue lines represent the standard peak position for PdCu intermetallic phase B2 (ICSD B2:181913). (I, J) XPS spectra showing palladium and copper binding energy of PdCu alloy nanowires respectively.

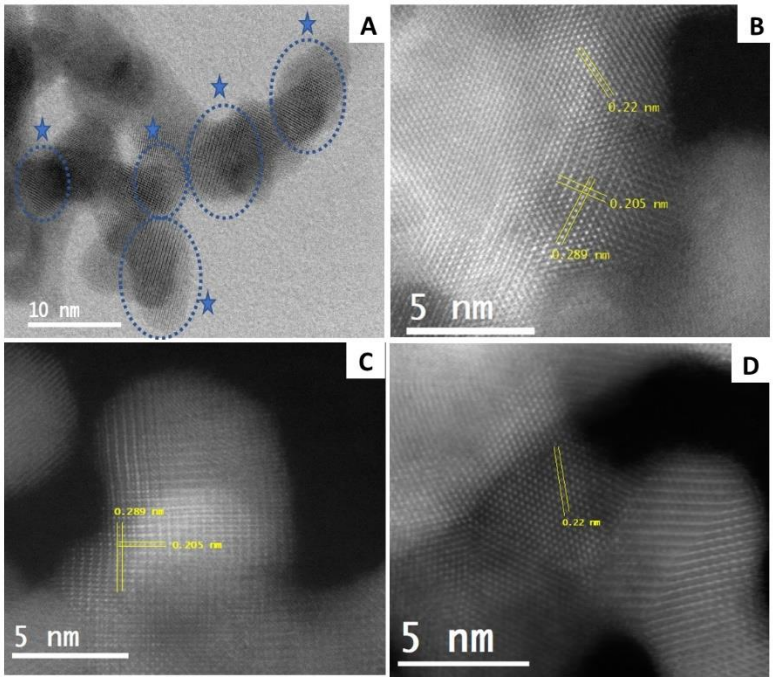

Figure 4. 4 (A) HRTEM *PdCu NWs showing the ordering structure mostly at the tips and junctions of *PdCu NWs. (B-C) HAADF STEM images of different areas of *PdCu. (B) showing d-spacing for B2-phase on the exterior area of the nanowires while d-spacing for A1 phase is observed at the inside area of *PdCu NWs. (C) Image exemplifying B2 phase at the tips with a d-spacing of around 0.205nm and 0.289nm corresponding to (110) and (100) planes respectively. (D) Image of A1 phase at the body of *PdCu NWs with a d-spacing of 0.22nm corresponding to (111) plane.

Finally, HRTEM and HAADF STEM studies of the *PdCu NW samples indicate the presence of planar defects showing incoherent twin boundaries as evidenced by the existence of screw dislocations (Figure 4.5A, B). In addition, we measured the strain on the samples (Figure 4.5B, C). The Data on Figure 4.5C correspond to an average over six data from different locations (next to the boundary, at a middle distance from the boundary, and far away from the boundary).

The strain measured on the sample correspond to a compressive strain based on its negative values of around -2.8, -1.1, -0.2 respectively (error bars are indicated on the graphic). Overall, the ordered structure of the *PdCu NWs plus its planar defects that leads to a compressive strain contribute to the catalytic performance of the material as in agreement with previous findings and with DFT calculations presented in this study.[35–37]

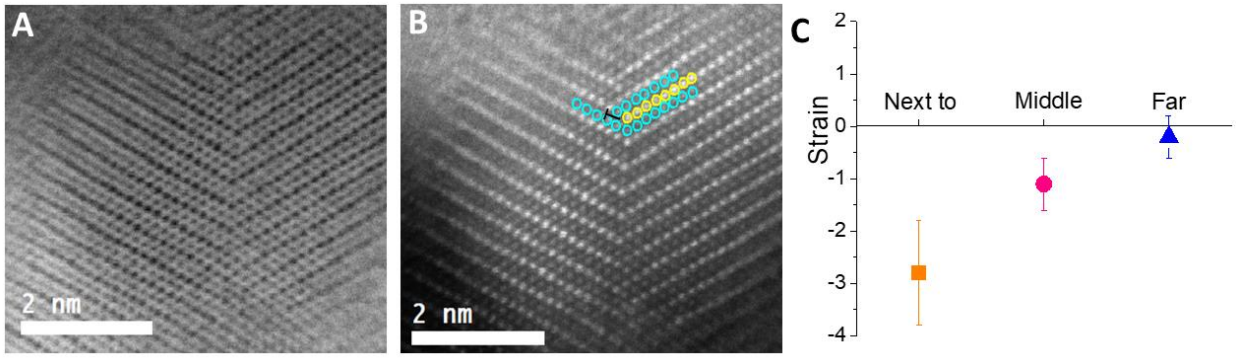

Figure 4. 5 (A) HRTEM *PdCu NWs showing the area of Twin defects within the ordered structure. (B) Same image than in (A) pointing out the screw dislocations and its respective Burgers vector. (C) Strain percentage measurement in 3 different locations related to the location of the twin boundary: next to, middle and far from the boundary.

4.2.1 Hydrogen Evolution Reaction

Considering the unique electronic properties of one-dimensional nanostructures, PdCu and *PdCu nanowires can therefore be used as active catalysts for diverse reactions. Hydrogen evolution reaction is the first reaction to be tested. The electrocatalytic activities of PdCu alloy NWs and *PdCu NWs were investigated in a standard three electrode electrochemical cell in acid

and alkaline media of a N2 saturated 0.5M H_2SO_4 or 1M KOH solution at a sweep rate of 20 mV/s. Representative linear sweep voltammetry (LSV) of geometric current density (mA/cm^2) vs RHE for the mentioned catalysts are shown in Figure 4.6 where they are also compared against our synthesized Pd nanowires and commercial Pt/C. HER performed in acid media are reported first in Figure 4.6A-F whereas results in alkaline media are shown in Figure 4.6G to I. HER activities of PdCu alloy NWs (Figure 4.6A) showed that to obtain a current density of 10 mA/cm^2 is required an overpotential of -41.3 mV which is much lower than that exhibit from Pd NWs and almost twice than Pt/C with takeover potentials of -231 and -19.2 mV, respectively (Figure 4.6B, Table 4.1). We compared catalyst results to their respective overpotentials (η) at 10 mA/cm^2 because it is a key parameter for practical purposes as in the construction of a fuel cells.[3] PdCu alloy NWs showed a similar tendency against Pd NWs and Pt/C at a current density of 50 mA/cm^2 (Table 4.1).

Tafel slope is another significant standard parameter used in HER because it helps to determine the exact mechanism as well as the rate-determining step. [3,6] Our catalyst PdCu alloy NWs present a Tafel slope close to Pt/C and much lower than Pd NWs with slopes of 33, 29, and 55 mV dec^{-1} respectively (Figure 4.6C). Therefore, the samples follow a Volmer-Tafel mechanism which is known typical for HER activity when exists very high H_{ads} coverage on Pt group surfaces.[3] iR correction was applied in all the figures if not specifically noted.

Additionally, stability test was performed on PdCu alloy nanowires and commercial Pt/C (4.7A, B). The tests were performed in 0.5M H_2SO_4, and it was proved that PdCu NWs present higher stability than commercial Pt/C as it is demonstrated from their potential drop in Figure

4.7B. After chronopotentiometry test, HER was tested for both materials, and surprisingly HER performed better for the cycled PdCu nanowires. In fact, their improvement was not only higher than the initial PdCu alloy NWs, but it also showed better performance than commercial Pt/C initial and after stability test *Pt/C.

As it was indicated previously based on the diverse characterization and analysis on Figure 4.3, the cycled sample went through a rearrangement of their atoms to a more ordered phase from A1 to B2 to form the newly processed material distinguish as *PdCu NWs. LSV curves for *PdCu NWs and their comparison with commercial *Pt/C are presented in Figure 4.6D-F. HER catalytic activity of *PdCu NWs showed to be superior than *Pt/C and initial Pt/C, exhibiting a small overpotential of -19.7 mV if compared to -37.9 mV of *Pt/C and comparable to -19.2 mV of Pt/C to obtain a current density of 10 mA/cm^2 (Figure 4.6D, E). In addition, to obtain a current density of 50 mA/cm^2 it was only necessary an overpotential of -90 mV which is lower than those for PdCu alloy NWs, Pd NWs and commercial *Pt/C. Tafel slope was also calculated for *PdCu NWs, showing a much lower Tafel slope than the rest of the samples (Pd NWs > PdCu alloy NWs > *Pt/C > Pt/C > *PdCu NWs) with a slope value of 27 mV dec^{-1} (Figure 4.6C, F; Table 4.1). These results suggest that *PdCu NWs display the best HER kinetics among all the electrocatalysts investigated, and in agreement with previous literature where a smaller Tafel slope and smaller overpotential signifies that the HER rate of *PdCu NWs would gain a faster increase towards a competitive potential for practical applications.[25] Additionally to these observations, LSV curves in Figure 4.6A and 4.6D suggest that both structures PdCu alloy and *PdCu nanowires present a strong H absorption which is observed in the curves around 0.0 and 0.05V vs RHE.

Finally, electrochemical active surface area (ECSA) was measured by CO stripping and compared with the ECSA measured by hydrogen desorption and Pd-O measurements obtained from the CV curves. The results demonstrate a superior ECSA for PdCu and *PdCu NWs if compared with the rest of the samples as it was expected due to their one-dimensional nature. Nonetheless, PdCu and *PdCu showed similar $ECSA_{CO}$ of around 83 and 81 m^2/g, and an $ECSA_H$ of around 72 and 79 m^2/g, respectively. Pt/C exhibited an $ECSA_{CO}$ and $ECSA_H$ of 45 and 41 m^2/g, respectively. A full comparison of the synthesized materials and state of art in acid media is showed on Table 4.1.

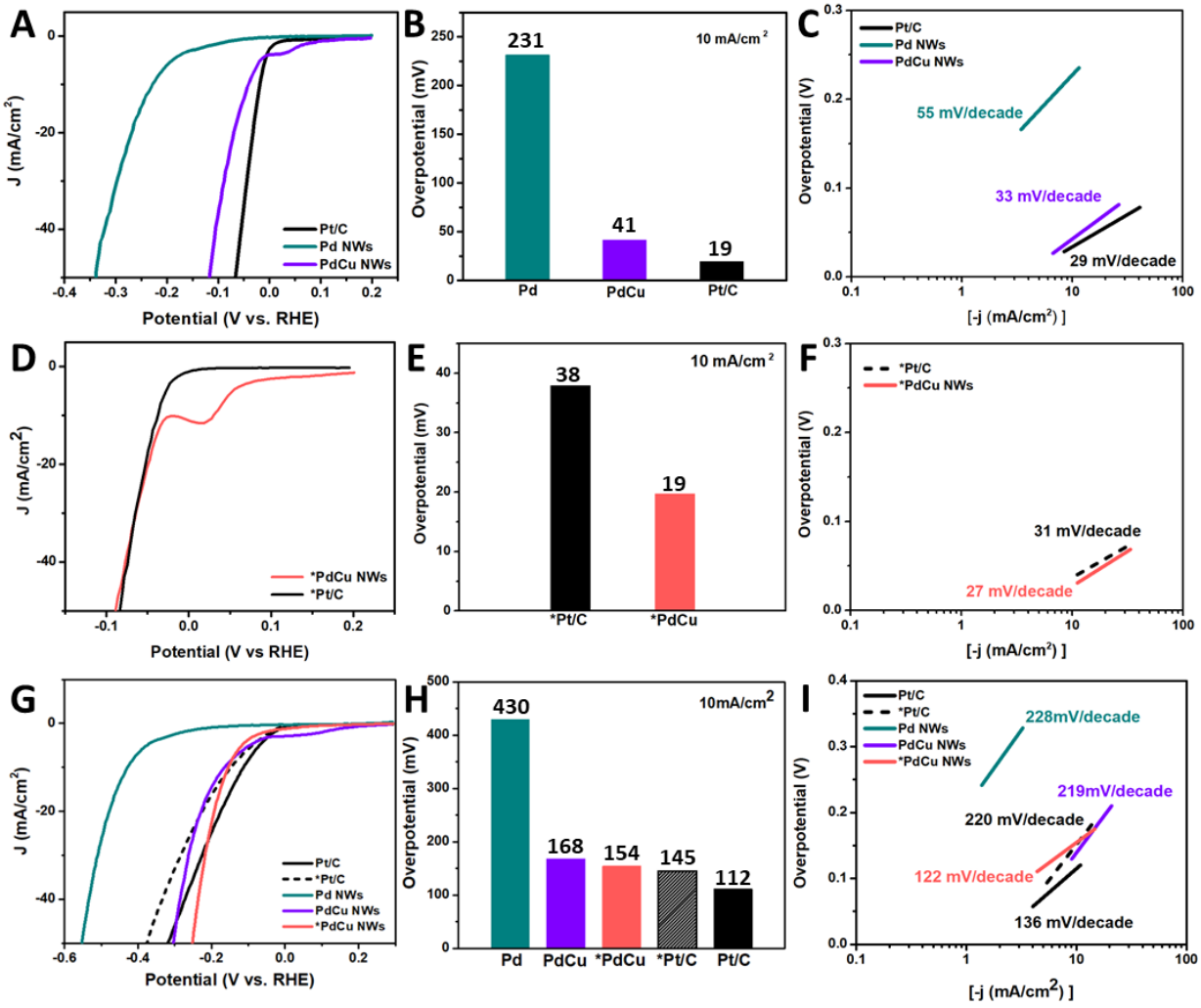

Figure 4. 6 HER electrochemical performance of the as-synthesized nanowires PdCu alloy NWs, *PdCu NWs and commercial Pt/C in acidic condition of 0.5M H_2SO_4 (A-F) and basic condition of 1M KOH (G-I). (A, D, G) HER polarization curves. (B, E, H) overpotential at 10 mA/cm^2. (C, F, I) corresponding Tafel plots. All the polarization curves were recorded with a scan rate of 5 mV/s, a rotation rate of 1600 r.p.m. and all the current densities were normalized to the geometric area of the working electrode.

The performance of the *PdCu NWs catalyst was also study under alkaline solution (1M KOH) and compared to their PdCu alloy NWs counterpart, Pd NWs and commercial Pt/C before and *Pt/C after stabilization test (Figure 4.6G-I). LSV curves in Figure 4.6G and overpotential bars in Figure 4.6H show that to obtain a current density of 10 mA/cm^2, *PdCu NWs needed an overpotential of -154.3 mV which is slightly higher than those overpotentials presented for *Pt/C, PdCu alloy NWs and Pt/C in that corresponding order. Nonetheless, in order to obtain a current density of 50 mA/cm^2, *PdCu NWs requires the lowest overpotential than the other catalysts. In fact, *PdCu NWs requires an overpotential of only -248 mV versus -280, -316, -374, and -547mV of PdCu alloy NWs, Pt/C, *Pt/C, and Pd NWs, respectively. Tafel slopes corroborate the results for *PdCu NWs showing a smaller slope of around 122 mV dec^{-1} while Pt/C exhibit a slope of 136 mV dec^{-1}. The rest of the catalysts exhibit much higher values for the Tafel slopes (Figure 4.6I). Once again, these results based on Tafel slope represent better kinetics for *PdCu NWs in alkaline media.

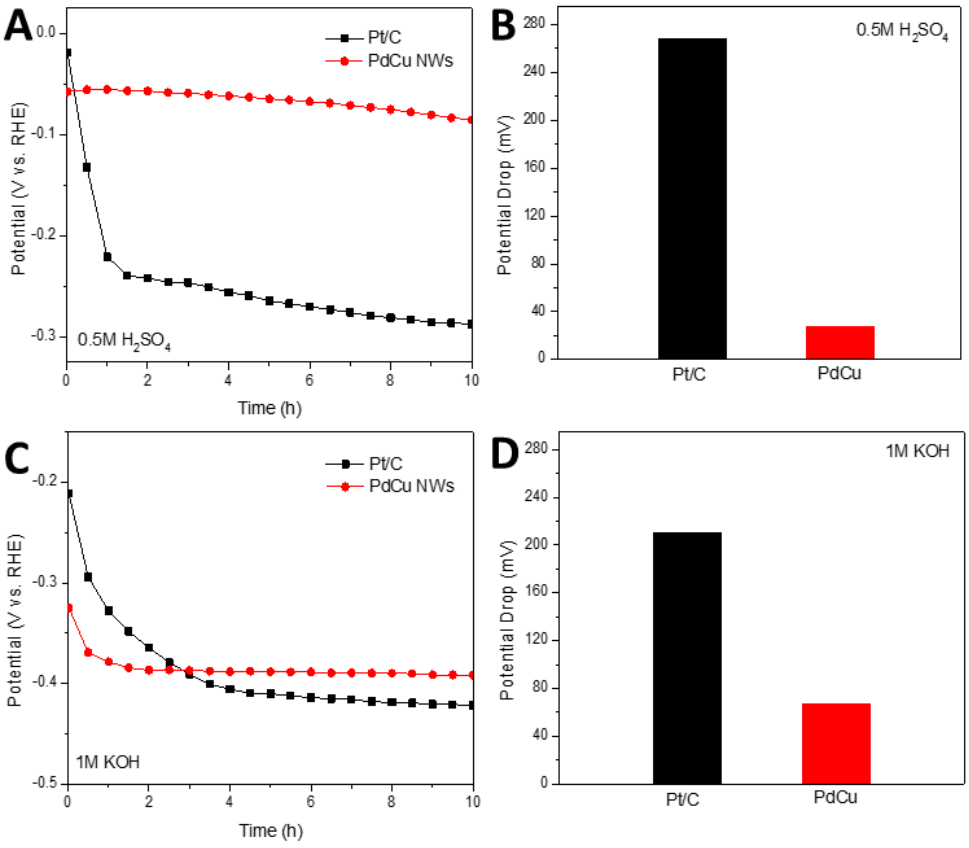

Figure 4. 7 Stability test comparing PdCu alloy nanowires with commercial Pt/C. The tests were performed in 0.5M H_2SO_4 (A, B) and in 1M KOH (C, D). (A,C) HER chronopotentiometry curves (B, D) Potential drop based on initial and end values.

Chronopotentiometry test was also evaluated in alkaline media for PdCu NWs catalyst and compared with commercial Pt/C. Surprisingly, it was observed that the ordered phase in *PdCu NWs is only found during cycling of the sample under acidic conditions, being basic conditions not optimal for the transformation of phases. Therefore, for chronopotentiometry test and HER curves, the PdCu NWs sample was first processed to *PdCu NWs in acid media and then the tests were performed. Lastly, Figure 4.7C and D showed PdCu NWs catalyst with better stability than Pt/C where the potential drop is only 65 mV versus 210 mV, respectively.

Table 4. 1 Comparison of the developed PdCu nanowires with state of art Pd and Pt based catalyst in acidic conditions

Sample	**Loading µg/cm^2**	**η at 10mA/cm^2 (mV)**	**η at 50mA/cm^2 (V)**	**ECSA (m^2/g)**	**Tafel Slope (mV/decade)**	**Reference**
PdCu nanowires	51	41.3	120	83	33	this work
*PdCu nanowires	51	19.7	90	81	27	this work
Pd nanowires	51	231.2	340	5	55	this work
Pt/C	51	19.2	66	45	29	this work
*Pt/C	51	37.9	90	-	31	this work
PdCu@PdNCs	140	68	~ 120	NA	35	ACS Appl. Mater. Interfaces. **2017**, 9, 8151−8160
Pd-Cu-S amorphous	~ 660	58	~ 120	NA	35	J. Mater. Chem. A. **2017**, 5, 18793
MWCNTs@Cu @MoS2	285	146	~ 260	NA	62	Journal of Power Sources. **2015**, 300 301-308
Pd-CNx np	43	55	90	63	35	ACS Catal. **2016**, 6, 1929−1941

To expand further understanding of our synthesized *PdCu nanowires, and how they can deliver higher HER activity in both acid and alkaline media we carried out DFT studies (Figure 4.8). We calculated the hydrogen binding energies (HBEs) of the experimentally invested systems,

including $Pd_{84}Cu_{16}$, PdCu-B_2, compressed PdCu-B2, Pt, Pd, and Cu. As shown in Figure 4.8a, the calculated HBEs are: -0.18 eV for $Pd_{84}Cu_{16}$, -0.13 eV for PdCu-B2, -0.02 eV for compressed PdCu-B2, -0.04 eV for Pt, -0.24 eV for Pd and 0.21 eV for Cu. Thus, the HBE of compressed PdCu-B2 is closest to zero, indicating that compressed PdCu-B2 provides the best performance at acidic conditions**.** This is consistent with experiment.

We calculated the reaction barrier for water dissociation ($E^a_{H2O\text{-}dissociation}$) (Figure 4.8b) of the experimentally invested systems, which includes $Pd_{84}Cu_{16}$, PdCu-B2, compressed PdCu-B2, Pt, Pd, and Cu. The calculated $E^a_{H2O\text{-}dissociation}$ are: 1.08 eV for $Pd_{84}Cu_{16}$, 0.94 eV for PdCu-B2, 0.98 eV for compressed PdCu-B2, 0.77 eV for Pt, 1.10 eV for Pd and 1.02 eV for Cu. Thus, the $E^a_{H2O\text{-}dissociation}$ of Pt is the lowest, and the PdCu-B2 is the second-lowest, indicating that Pt represents the best performance at alkaline condition and the PdCu-B2 represents the second-best performance at alkaline condition. This is consistent with experiment. Overall, the DFT calculations predict that the PdCu-B2 phase is responsible for the improved HER performance, as observed experimentally. Specifically, the improved HER performance at acidic condition is due to the decreased HBE of compressed PdCu-B2 phase, and the improved HER performance at alkaline condition is due to the reduced barrier for water dissociation at alkaline condition of PdCu-B2 phase.

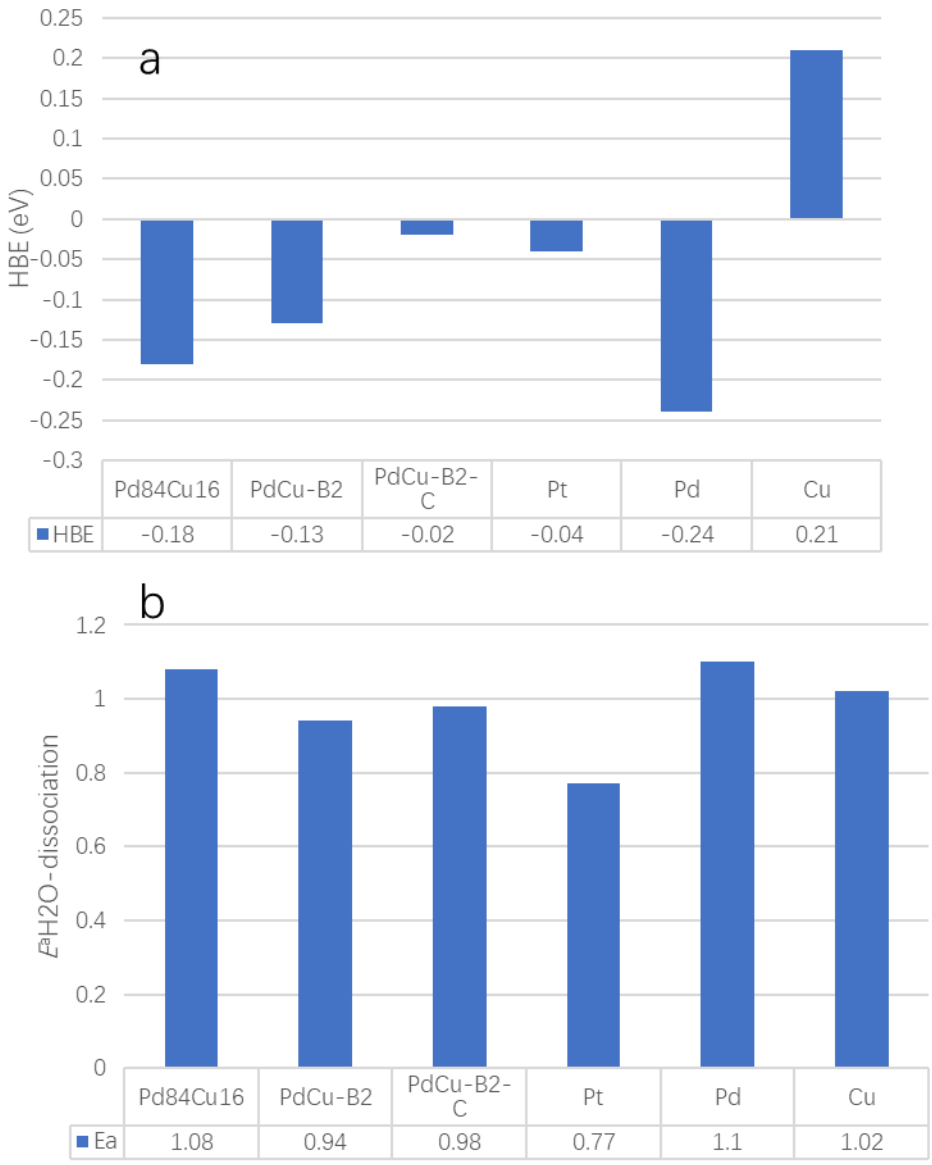

Figure 4. 8 (a) DFT calculated hydrogen binding energies (HBEs). (b) DFT calculated reaction barrier for water dissociation ($E^{a}_{H2O\text{-}dissociation}$).

4.2.2 Formic Acid Oxidation Reaction

An extra reaction was tested on PdCu alloy and *PdCu intermetallic nanowires which prove them as excellent catalysts for electron-oxidation reaction of small molecules like FAOR, the anodic reaction in DFACFC. Pd based catalysts are known as the optimum materials for this type of reaction since HCOOH is first adsorbed on Pd surface to promote its dissociation, followed by a 2 electron oxidation process to convert to CO_2 in a direct oxidation path eliminating undesired products as CO commonly observed in Pt based materials.[14,18,39]

$$HCOOH \rightarrow CO_2 + 2H+ + 2e^- \ (^{18,31})$$

Nonetheless, Pd catalytic performance can be improved if a transition metal is incorporated to the catalyst, promoting the HO formation, thus, oxidizing CO on Pd surface which will increase the CO tolerance of Pd suggesting an expected good performance for our PdCu materials.[14] Thus, CV measurements and FAOR tests were performed at room temperature in a three-electrode cell from Pine Research Instrumentation at room temperature. Silver/silver chloride (Ag/AgCl), a carbon rod and a glassy carbon rotating disk electrode (RDE) coated with corresponding catalyst were used as the reference, counter and working electrode respectively. All potentials are reported referenced to RHE. Loading was established to be the same (82 $\mu g_{Pd}/cm^2$) for all the palladium-based materials tested (Pd/C, PdCu NWs, *PdCu NWs). Estimation of Pd loading is based on overall Pd ratio within catalyst determined by ICP-AES.

First, CV measurements were conducted to activate the catalyst surface in a N2 saturated 0.5M H_2SO_4 between 0.0 to 1.2 V vs. RHE at a sweep rate of 100 mV/s until stability of the material (around 120 cycles). FAOR measurements were conducted immediately after activation in a N2 saturated 0.5M H_2SO_4 and 0.5 M HCOOH between 0.0 to 1.2 V vs. RHE at a sweep rate of 50 mV/s. Figure 4.9A shows the CV curves for the samples where it is not observed Cu oxidation-reduction peaks, suggesting that the nanowires surface is well conditioned [14] and not dissolution of copper on the catalyst surface occurred. On the other hand, peaks observed in the range of 0 to 0.4 V vs RHE correspond to two redox regions: hydrogen H_{UPD} adsorption/desorption at the surface, and H absorption/desorption into the PdCu lattice (from the most positive to negative peaks respectively), whereas peaks from 0.6 to 0.8 V vs. RHE correspond to the oxidation/reduction of PdCu surface.[2,11] Moreover, figure 4.9B shows that during positive scan a current is generated while a potential is applied, indicating the indicating the oxidation of formic acid where the maximum current peak is characteristic for each catalyst tested. The mass current density in the y-axis of Figure 4.9B is normalized to the mass of Pd for all the samples. As it is observed, the highest mass activity is for *PdCu nanowires. Impressively, *PdCu intermetallic NWs presents higher activities than their alloy counterpart and seven times higher than commercial Pd, measured under similar conditions.

Their high performance of *PdCu NWs can be attributed to their structural feature of nanowires and bimetallic composition, yet their intermetallic nature plays a major role in its performance. In general, the exceptional performance of PdCu and *PdCu nanowires is related to i) Pd which is the active catalyst for FAO, ii) Cu which enables the adsorption and oxidation of intermediates, and iii) intermetallic nature of *PdCu NWs with a major effect on the catalytic

reaction pathway.[8,27,40] In fact, copper has been used previously to not only improve the catalytic performance but also to enhance the poisoning tolerance to intermediates like CO.[40] Additionally, there exists an electronic effect between Pd and Cu where Pd can gain d-electrons from Cu to relieve adsorption strength for CO. The synergistic effect previously mentioned has also been reported in previous literatures by density functional theory (DFT) calculations suggesting good catalytic activity towards FAOR.[10,27,41] Hence, our palladium copper nanomaterials are expected to be superior for FAOR than commercial palladium.

Our results show that *PdCu nanowires with swollen tips and junctions exhibit better performance toward FAOR, having a mass activity of around 3735 mA/mg_{Pd} which is higher than PdCu alloy NWs and seven times higher than commercial palladium with values of around 2540 and 527 mA/mg_{Pd} respectively. The values for intermetallic *PdCu NWs and alloy PdCu NWs are superior than other previous studies, and the value reported for commercial Pd is in agreement with previous FAOR studies where the activity is roughly 500 mA/mg_{Pd}.[10] A comparison table between our synthesized material and state of art for FAOR are reported on Table 4.2.

FAOR curves of PdCu alloy nanowires presented in Figure 4.9B indicate the appearance of a shoulder around 0.9V which correspond to CO oxidation during positive scan indicating that dehydration pathway ($CO + H_2O$) is still present but the main mechanism controlling the reaction is dehydrogenation (CO_2). Similar scanning is done on *PdCu NWs where the shoulder is reduced or almost non-visible suggesting a better dehydrogenation process and in agreement with previous literature.[14,39] Other factor to consider in FAOR is the onset potential which in the case of *PdCu NWs is much lower or shifted to a more negative value of around 0.168V if compared with PdCu

alloy NWs and Pd commercial with values around 0.178 and 0.188 V vs RHE respectively. Moreover, the sharp peaks observed at around 0.8V vs RHE in the negative scan for both PdCu alloy and *PdCu nanowires indicate that the catalyst surface is regenerated via surface reduction, observed by the sudden jump in the current. These observations suggest that Pd in the *PdCu nanowires is reduced more efficiently which is translated in an efficient reduction of Pd oxide layer, essential process for activation of the formic acid electro-oxidation rate, and in agreement with previous literatures.[10,18] In addition, these demonstrate that the Pd in *PdCu nanowires exhibit a more "noble" character than Pd in commercial Pd.[10] Thus, the higher oxidation peak value for mass activity and the lower onset potential, demonstrate that the electrooxidation activity for FAOR is favored in the ordered *PdCu nanowires. These parameters have been suggested as the chosen ones to find optimum catalysts for the mentioned reaction, which in most cases has involved a mixture of noble metals with non-noble metals as PdCu nanostructures.[8,10,11,40–42]

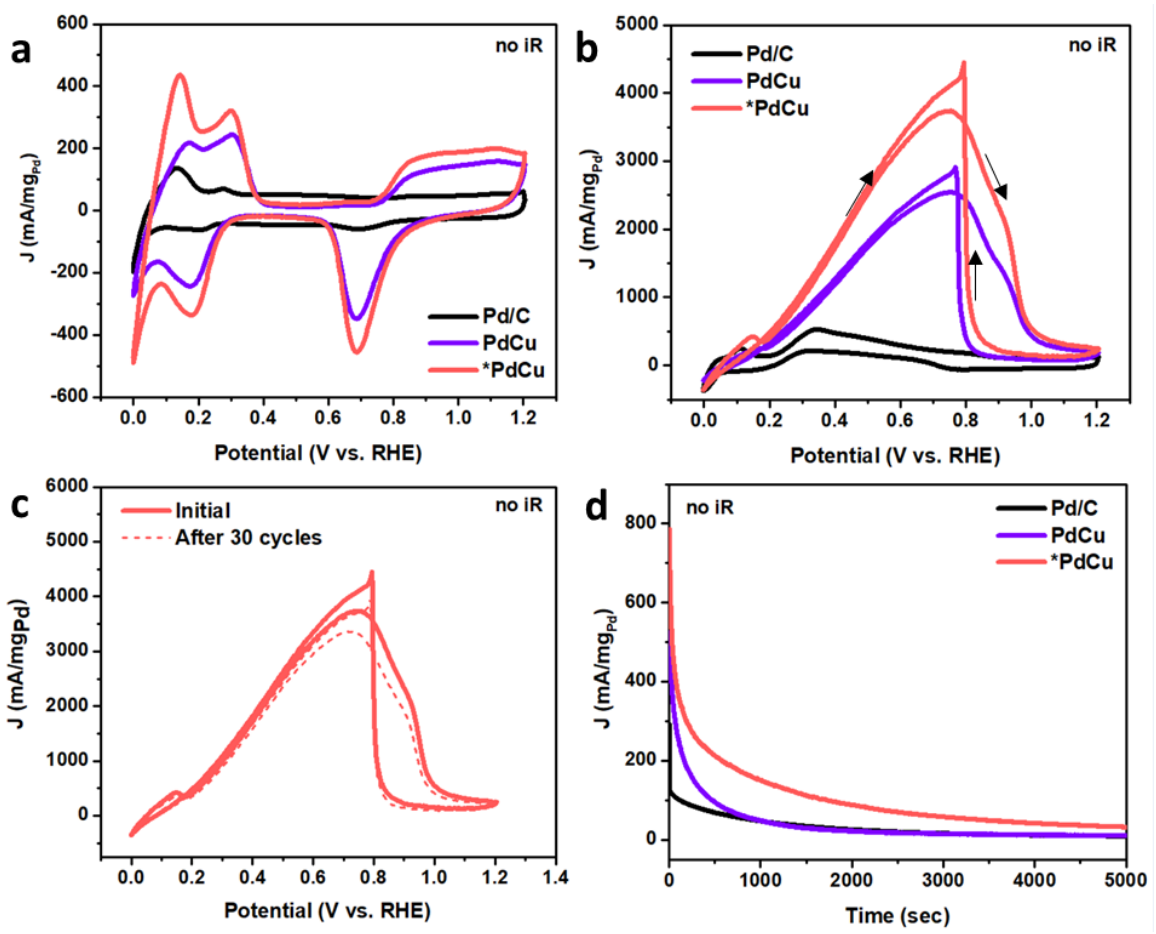

Figure 4. 9 (A) Cyclic voltammetry (CV) curves and (B) FAOR CVs of the as-synthesized nanowires PdCu alloy NWs, *PdCu NWs and commercial Pd/C. (C) FAOR CV of initial *PdCu NWs and after 30 cycles. (D) Chronoamperometry (CA) curves of the as-synthesized nanowires PdCu alloy NWs, *PdCu NWs and commercial Pd/C. The CVs were obtained in N_2 saturated 0.5M H_2SO_4 at a scan rate of 100 mV/s, and the FAOR CVs were in N_2 saturated 0.5M H_2SO_4 + 0.5M HCOOH with a scan rate of 50mV/s. CA curves were recorded at 0.4V for 5000 s in 0.5M H_2SO_4 + 0.5M HCOOH solution. All the tests were conducted at room temperature.

Finally, stability tests were performed by chronoamperometry (CA) measurements in a N_2 saturated solution of 0.5M H_2SO_4 and 0.5 M HCOOH at 0.4V (Figure 4.9D). After stability tests,

not obvious changes in terms of nanowires morphology was observed. During the first 250 seconds, commercial Pd/C decays very fast, then PdCu alloy NWs, and finally *PdCu NWs which decays in a much slower speed. After 1000 seconds, PdCu alloy nanowires and commercial Pd showed equivalent current densities suggesting similar stability in the larger stage while *PdCu NWs exhibit superior stabilities as it displays superior mass current densities than alloy and commercial Pd/C. In addition, *PdCu NWs was under cycling test for 30 cycles in the same conditions as FAOR (Figure 4.9C) with a mass current activity of around 3360.5 mA/mg_{Pd} which is only 10% less than the initial mass current density peak (Figure 4.9C).

Table 4.2 Comparison of the developed *PdCu nanowires with state of art Pd based catalyst for FAOR

Catalyst	**Morphology**	**ECSA (m^2/g)**	**Mass Current Density (mA/mgPd)**	**Electrolyte**	**Reference**
*PdCu	Nanowires	81	3735	0.5M H_2SO_4 + 0.5M HCOOH	This work
PdCu	Nanowires	83	2540	0.5M H_2SO_4 + 0.5M HCOOH	This work
Pd/C	commercial	35	527	0.5M H_2SO_4 + 0.5M HCOOH	This work
PdCu Alloy	Nanosheets	139.8	1655.7	0.5M H_2SO_4 + 0.25M HCOOH	Adv. Mater. **2017**, 29, 1700769
CuPd	Nanoparticle / nanorods	--	2086	0.1M $HClO_4$ + 0.1M HCOOH	J. Am. Chem. Soc. **2017**, 139, 15191−15196
Pd (Penta twinned)	Nanowires	26.2	907.5	0.5M $HClO_4$ + 0.5M HCOOH	ACS Appl. Mater. Interfaces. **2017**, 9, 31203−31212
$Pd/WO_{2.72}$	Nanoparticle / nanorods	--	1618.3	0.1M $HClO_4$ + 0.1M HCOOH	Nano Lett. **2017**, 17, 2727−2731
Cu@Pd core-shell	Nanowires	62.8	2197.88	0.1M $HClO_4$ + 2M HCOOH	Electrochimica. **2014**, acta 143, 44–48
PdCu	Nanotripod	28.7	1580	0.5M H_2SO_4 + 0.5M HCOOH	Adv. Funct. Mater. **2014**, 24, 7520–7529[4]
Pd_3Fe Intermetallic	Nanoparticle	21.3	696.4	0.5M H_2SO_4 + 0.5M HCOOH	Nano Research. **2018**, 11(9): 4686–4696
NiPd/rGO	Nanowires	98.2	604.3	0.5M H_2SO_4 + 0.5M HCOOH	J. Mater. Chem. A **2015**, 3, 14001–14006
Cu@PdCu	Nanotubes @ Nanoparticles	72.8	1806	0.1M $HClO_4$ + 2M HCOOH	Nanotechnology. **2016**, 27, 495403

4.3 Conclusion

In summary, the strategy presented in this work is helpful for future expansion to fabricate alloy and intermetallic nanowires based on noble metals combined with non-noble metals to continue exploring the synergetic properties when they are combined in a one-dimensional nanostructure. Moreover, this approach is an example of new routes for the development of multifunctional catalysts which could encourage investigations to continue finding better options towards a universal catalyst at lower cost but still with high catalytic activity performance for diverse of catalytic reactions.

Our synthesized *PdCu NWs nanomaterials demonstrated enhanced electrocatalytic activity towards HER in acid and basic conditions and towards FAOR, even higher than PdCu alloy NWs, PdNWs and commercial Pd and Pt for their respective reactions.

Intermetallic *PdCu NWs make a difference in the catalytic activities mainly for 3 reasons: i) intermetallic phase presented in the synthesized nanowires since intermetallic compounds have stablished as better catalysts in terms of activity and stability than their alloy counterparts, ii) the synergetic effect between PdCu, iii) the 1D morphology of ultrathin nanowires with swollen tips and junctions. All of these make them suitable for high HER performance and high mass activities during FAOR as it is observed from the experimental results.

4.4 Experimental Methods

4.4.1 Chemicals and materials. Palladium (II) Chloride [$PdCl_2$, ≥99%], Copper (II) Chloride [$CuCl_2$ ≥99.99%], Triton X-100 [t-Oct-C_6H_4-(OCH_2CH_2)xOH, x= 9-10 <3% Polyethylene Glycol], Sodium Borohydride [$NaBH_4$ ≥99.99%] were purchased from Sigma Aldrich. Commercial Pt/C catalyst (40 wt% Pt, particle size 2 to 5 nm) were purchased from Alfa Aesar. Ethanol (200 proof) were obtained from Decon Labs, Inc. All reagents were used as received without further purification. The deionized water (18 MΩ/cm) was obtained from an ultra-pure purification system (Milli-Q advantage A10).

4.4.2 Synthesis of Pd-Cu Alloy Nanowires. 0.1mL of Triton X-100 was diluted to 50mL of water. 135 mg of $CuCl_2$ was dissolved in 10 mL of water to prepare a 100 mM solution. 177 mg $PdCl_2$ and 166 µL HCl were dissolved in 10 mL of water and sonicated for half an hour to prepare a 100 mM solution of $H_2Pd_2Cl_4$. 38 mg of $NaBH_4$ was dissolved into 10 mL water (freshly) to prepare a 100 mM solution. 48 mL of the Triton solution was added to an Erlenmeyer flask, which was then submerged into an ice bath water. 1 mL of prepared solution of $CuCl_2$, and 1 mL $H_2Pd_2Cl_4$ were then added to the flask, at which point the solution was magnetically stirred. Finally, 3mL of $NaBH_4$ solution was added. The solution continued stirring for 5 minutes and left the dispersed product to sit overnight. The Pd-Cu Nanowires were washed with a 50/50% by volume water and ethanol mixture and collected by centrifugation.

4.4.3 Preparation of *PdCu Nanowires Catalysts. The as-prepared *PdCu NWs were obtained electrochemically through a dealloying process in which 10 µL of the synthesized PdCu alloy

nanowires were dropped onto a 5 mm diameter glassy-carbon electrode. The material was first activated through 120 cycles in a CV process using 0.5M H_2SO_4 solution as an electrolyte (refer to CV measurements in HER). After activation process, the material was maintained at constant current of 2 mA for 10 hrs. At these conditions a rearrangement of Pd and Cu atoms to a more ordered structure was observed to form *PdCu nanowires. Reactions as HER or FAOR were tested after this procedure.

4.4.4 Characterization. Transmission electron microscopy (TEM) images were taken on a FEI T12 operated at 120 kV. High resolution TEM images (HR-TEM) was taken on a FEI TITAN operated at 300 kV. Energy-dispersive X-ray spectroscopy (EDS) mapping and high angle annular dark field (HAADF) scanning transmission electron microscopy were acquired by scanning transmission electron microscope (STEM). Samples for TEM measurements were prepared by dropping 10-20 μL of the respective nanowires samples in ethanol dispersed onto a carbon coated copper grids (Ted Pella, Redding, CA) for TEM images. Al grid (Ted Pella, Redding, CA) was used for HRTEM, EDS analysis, and HAADF STEM analysis. Powder X-ray diffraction patterns (PXRD) were collected on a Panalytical X'Pert Pro X-ray Powder Diffractometer with Cu-Kα radiation. The compositions and oxidation states were checked by X-ray photoelectron spectroscopy (XPS) on a K-Alpha XPS spectrometer (ThermoFisher, E.Grinstead, UK) with Al Kα X-ray radiation (1486.6 eV) for excitation. The concentration of catalysts was determined by inductively coupled plasma atomic emission spectroscopy (ICP-AES, Shimadzu ICPE-9000) as well as EDS coupled in ZEISS Supra 40VP scanning electron microscope (SEM).

4.4.5 Electrochemistry measurements. Electrochemical experiments were performed on a three-electrode cell from Pine Research Instrumentation at room temperature. Saturated mercury/mercury sulfate ($Hg/HgSO_4$) and silver/silver chloride (Ag/AgCl) were used as the reference electrodes during hydrogen evolution reaction (HER) and formic acid oxidation reaction (FAOR) respectively, a carbon rod as the counter electrode, and a glassy carbon rotating disk electrode (RDE) coated with corresponding catalyst as the working electrode. All potentials are reported referenced to RHE.

4.4.5.1 Hydrogen evolution reaction. The catalyst ink was prepared by mixing 1 mg of catalyst PdCu with 1 mL of ethanol solution containing 16μL of Nafion (5 wt%) with 15 min ultrasonication time. Then, 10 μL of catalyst ink was dropped onto a 5 mm diameter glassy-carbon electrode (Pine Research Instrumentation), this set up was maintained for all catalysts tested. Estimation of PdCu loading is based on overall Pd:Cu ratio within catalyst determined by ICP-AES, which loading is about 0.8:0.2 μg for PdCu and 0.56:0.44 μg for *PdCu NWs respectively. The ink was dried under an infrared lamp, then the electrode was ready for electrochemical test. Commercial Pt/C catalyst was used as the baseline catalysts for HER in acid and alkaline media, and similar procedure as described above was used to conduct the electrochemical measurements. For all our tested materials for HER (20%Pt/C, Pd NWs, PdCu NWs, and *PdCu NWs) the total loading based on 10 μL of catalyst ink was established to be 51 $\mu g/cm^2$. Cyclic Voltammetry (CV) measurements was conducted in a N2 saturated 0.5M H_2SO_4 for acid conditions, and 1M KOH for alkaline conditions solution between 0.05 to 1.1 V vs. reverse hydrogen electrode (RHE) at a sweep rate of 100 mV/s. Hydrogen evolution reaction (HER) measurements were conducted in an N2 saturated 0.5M H_2SO_4 or 1M KOH solution at a sweep rate of 20 mV/s. The impedance of each

solution was tested on a Princeton VersaSTAT 4 electrochemistry workstation. The solution resistances measured via impedance test are 4.6 Ω and 5.1 Ω for 0.5M H_2SO_4 and 1M KOH, respectively. The above values are used for post-test iR correction results. Chronopotentiometry test was performed in the samples in a N_2 saturated 0.5M H_2SO_4 or 1M KOH solution at a constant rotation disk of around 1600 r.p.m. by applying a constant current of 2 mA.

4.4.5.2 Formic acid oxidation reaction. The catalyst ink for FAOR was prepared in the same way than in the HER procedure with the difference that this time 20 μL of catalyst ink of the catalysts were dropped onto a 5 mm diameter glassy-carbon electrode (Pine Research Instrumentation). Loading was established to be the same for all the palladium-based materials (10%Pd/C, PdCu NWs, *PdCu NWs) resulting in a loading of 82 $\mu g/cm^2$ (Pd mass normalized) for all the catalysts. Once again, estimation of Pd loading is based on overall Pd ratio within catalyst determined by ICP-AES. The ink was dried under an infrared lamp, then the electrode was ready for electrochemical test. Commercial Pd/C catalyst was used as the baseline catalysts for FAOR, and similar procedure as described above was used to conduct the electrochemical measurement. Cyclic Voltammetry (CV) measurements was conducted in a N2 saturated 0.5M H_2SO_4 between 0.0 to 1.2 V vs. reverse hydrogen electrode (RHE) at a sweep rate of 100 mV/s. Formic acid oxidation reaction (FAOR) measurements were conducted in a N2 saturated 0.5M H_2SO_4 + 0.5 M HCOOH between 0.0 to 1.2 V vs. RHE at a sweep rate of 50 mV/s. Stability Test were measured by cycling the material in the same conditions for 120 cycles. Chronoamperometry curves were also conducted for 5000 seconds at 0.4V in a N2 saturated 0.5M H_2SO_4 + 0.5 M HCOOH solution. All the measurements were conducted at room temperature.

4.4.5.3 Electrochemically active surface area. The electrochemically active surface area (ECSA) was measured by CO stripping and compared with the ECSA measured by hydrogen desorption and Pd-O measurements obtained from the CV curves. For the CO stripping voltammetry measurements, working electrodes coated with different catalysts were firstly immersed in a CO saturated 0.5 M H2SO4 solution for 5 min, and then the CO stripping voltammetry was recorded respectively between 0.05 to 1.3 V vs. RHE at a sweep rate of 25 mV/s. ECSA calculation based on hydrogen desorption and Pd-O peaks were performed in N_2-saturated 0.5 M H^2SO^4 solution at scan rate of 100 mV/s. All the measurements were performed at room temperature and curves were normalized by the total mass of the loaded metal (Pt or Pd) based on ICP analysis.

4.5 References

1. Li, J.; Li, F.; Guo, S.; Zhang, J.; Ma, J. PdCu @ Pd Nanocube with Pt-like Activity for Hydrogen Evolution Reaction. *ACS Appl. Mater. Interfaces* **2017**, *9*, *8151-8160*.
2. Zalineeva, A.; Baranton, S.; Coutanceau, C.; Jerkiewicz, G. Octahedral Palladium Nanoparticles as Excellent Hosts for Electrochemically Adsorbed and Absorbed Hydrogen. *Sci. Adv.* **2017**, 3, 1–11.
3. Bhowmik, T.; Kundu, M. K.; Barman, S. Palladium Nanoparticle − Graphitic Carbon Nitride Porous Synergistic Catalyst for Hydrogen Evolution/Oxidation Reactions over a Broad Range of PH and Correlation of Its Catalytic Activity with Measured Hydrogen Binding Energy. *ACS Catal.* **2016**, *6*, 1929–1941.
4. Zhang, H.; An, P.; Zhou, W.; Guan, B. Y.; Zhang, P. Dynamic Traction of Lattice-Confined Platinum Atoms into Mesoporous Carbon Matrix for Hydrogen Evolution Reaction. *Sci. Adv.* **2018**, 4, 1–9.
5. Zheng, Y.; Jiao, Y.; Zhu, Y.; Li, L. H.; Han, Y.; Chen, Y.; Jaroniec, M.; Qiao, S. High Electrocatalytic Hydrogen Evolution Activity of an Anomalous Ruthenium Catalyst. *J. Am. Chem. Soc.* **2016**, *138*, 16174–16181.
6. Mahmood, J.; Li, F.; Jung, S.; Okyay, M. S.; Ahmad, I.; Kim, S.; Park, N.; Jeong, H. Y.; Baek, J. An Efficient and PH-Universal Ruthenium-Based Catalyst for the Hydrogen Evolution Reaction. *Nat. Nanotechnol.* **2017**, *12* (5), 441–446.
7. Cao, L.; Luo, Q.; Liu, W.; Lin, Y.; Liu, X.; Cao, Y.; Zhang, W.; Wu, Y.; Yang, J.; Yao, T.; et al. Identification of Single-Atom Active Sites in Carbon-Based Cobalt Catalysts during Electrocatalytic Hydrogen Evolution. *Nat. Catal.* **2019**, *2*, 134–141.
8. Zhang, L.; Choi, S. Il; Tao, J.; Peng, H. C.; Xie, S.; Zhu, Y.; Xie, Z.; Xia, Y. Pd-Cu

Bimetallic Tripods: A Mechanistic Understanding of the Synthesis and Their Enhanced Electrocatalytic Activity for Formic Acid Oxidation. *Adv. Funct. Mater.* **2014**, *24* (47), 7520–7529.

9. Ding, J.; Bu, L.; Zhang, N.; Yao, J.; Huang, Y.; Huang, X. Facile Synthesis of Ultrathin Bimetallic PtSn Wavy Nanowires by Nanoparticle Attachment as Enhanced Hydrogenation Catalysts. *Chem. - A Eur. J.* **2014**, *21* (10), 3901–3905.
10. Li, S.; Cheng, D.; Qiu, X.; Cao, D. Synthesis of Cu@Pd Core-Shell Nanowires with Enhanced Activity and Stability for Formic Acid Oxidation. *Electrochim. Acta* **2014**, *143*, 44–48.
11. Wang, X.; Yang, J.; Yin, H.; Song, R.; Tang, Z. "Raisin Bun"-Like Nanocomposites of Palladium Clusters and Porphyrin for Superior Formic Acid Oxidation. *Adv. Mater.* **2013**, *25* (19), 2728–2732.
12. Ji, X.; Lee, K. T.; Holden, R.; Zhang, L.; Zhang, J.; Botton, G. A.; Couillard, M.; Nazar, L. F. Nanocrystalline Intermetallics on Mesoporous Carbon for Direct Formic Acid Fuel Cell Anodes. *Nat. Chem.* **2010**, *2* (4), 286–293.
13. Study, A. R. M. Formic Acid Oxidation in a Polymer Electrolyte Fuel Cell. *J. Electrochem. Soc.* **1996**, *143* (7), 1994–1996.
14. Xi, Z.; Li, J.; Su, D.; Muzzio, M.; Yu, C.; Li, Q.; Sun, S. Stabilizing CuPd Nanoparticles via CuPd Coupling to WO2.72Nanorods in Electrochemical Oxidation of Formic Acid. *J. Am. Chem. Soc.* **2017**, *139* (42), 15191–15196.
15. C. Li, Q. Yuan, B. Ni, T. He, S. Zhang, Y. Long, L. Gu, X. W. Dendritic Defect-Rich Palladium-Copper-Cobalt Nanoalloys as Robust Multifunctional Non-Platinum Electrocatalysts for Fuel Cells. *Nat. Commun.* **2018**, *9* (3702), 1–9.

16. Wu, D.; Xu, H.; Cao, D.; Fisher, A.; Gao, Y.; Cheng, D. PdCu Alloy Nanoparticle-Decorated Copper Nanotubes as Enhanced Electrocatalysts : DFT Prediction Validated by Experiment. *Nanotechnology* **2016**, *27*, 1-11.

17. Wen, C.; Wei, Y.; Tang, Di.; Sa, B.; Zhang, T.; Chen, C. Improving the Electrocatalytic Properties of Pd-Based Catalyst for Direct Alcohol Fuel Cells: Effect of Solid Solution. *Sci. Rep.* **2017**, *7* (1), 1–11.

18. Mazumder, V.; Chi, M.; Mankin, M. N.; Liu, Y.; Metin, Ö.; Sun, D.; More, K. L.; Sun, S. A Facile Synthesis of MPd (M = Co, Cu) Nanoparticles and Their Catalysis for Formic Acid Oxidation. *Nano Lett.* **2012**, *12* (2), 1102–1106.

19. Bin, D.; Yang, B.; Ren, F.; Zhang, K.; Yang, P.; Du, Y. Facile Synthesis of PdNi Nanowire Networks Supported on Reduced Graphene Oxide with Enhanced Catalytic Performance for Formic Acid. *J. Mater. Chem. A* **2015**, *3*, 14001–14006.

20. Liu, Z.; Fu, G.; Li, J.; Liu, Z.; Xu, L.; Sun, D.; Tang, Y. Facile Synthesis Based on Novel Carbon-Supported Cyanogel of Structurally Ordered Pd3Fe / C as Electrocatalyst for Formic Acid Oxidation. *Nano Res.* **2018**, *11* (9), 4686–4696.

21. Darby, M. T.; Sykes, E. C. H.; Michaelides, A.; Stamatakis, M. Carbon Monoxide Poisoning Resistance and Structural Stability of Single Atom Alloys. *Top. Catal.* **2018**, *61* (5–6), 428–438.

22. Zhang, J.; Chen, M.; Li, H.; Li, Y.; Ye, J.; Cao, Z.; Fang, M. Stable Palladium Hydride as a Superior Anode Electrocatalyst for Direct Formic Acid Fuel Cells. *Nano Energy* **2018**, *44* (December 2017), 127–134.

23. Wang, H.; Yang, W.; Zhang, Q.; Qiu, Q. Shape-Controlled Synthesis of Palladium-Copper Nanoalloys with Improved Catalytic Activity for Ethanol Electrooxidation. *International*

Journal of Electrochemistry **2016**, 2016, 1–8.

24. Huang, H.; Ruditskiy, A.; Choi, S. Il; Zhang, L.; Liu, J.; Ye, Z.; Xia, Y. One-Pot Synthesis of Penta-Twinned Palladium Nanowires and Their Enhanced Electrocatalytic Properties. *ACS Appl. Mater. Interfaces* **2017**, *9* (36), 31203–31212.
25. Chao, T.; Luo, X.; Chen, W.; Jiang, B.; Ge, J.; Lin, Y.; Wu, G.; Wang, X.; Hu, Y.; Zhuang, Z.; et al. Hydrogen Evolution Reaction Atomically Dispersed Copper – Platinum Dual Sites Alloyed with Palladium Nanorings Catalyze the Hydrogen Evolution Reaction Angewandte. **2017**, 16047–16051.
26. Qiu, Y.; Xin, L.; Li, Y.; Mccrum, I. T.; Guo, F.; Ma, T.; Ren, Y.; Liu, Q. BCC-Phased PdCu Alloy as a Highly Active Electrocatalyst for Hydrogen Oxidation in Alkaline Electrolytes. *J. Am. Chem. Soc.* **2018**, *140*, 16580–16588.
27. Nie, X.; Jiang, X.; Wang, H.; Luo, W.; Janik, M. J.; Chen, Y.; Guo, X.; Song, C. Mechanistic Understanding of Alloy Effect and Water Promotion for Pd-Cu Bimetallic Catalysts in CO2 Hydrogenation to Methanol. *ACS Catal.* **2018**, *8*, 4873–4892.
28. Ma, S.; Sadakiyo, M.; Heima, M.; Luo, R.; Haasch, R. T.; Gold, J. I.; Yamauchi, M.; Kenis, P. J. A. Electroreduction of Carbon Dioxide to Hydrocarbons Using Bimetallic Cu − Pd Catalysts with Different Mixing Patterns. *J. Am. Chem. Soc.* **2017**, *139*, 47–50.
29. Wu, Z.; Shan, S.; Xie, Z.; Kang, N.; Park, K.; Hopkins, E.; Yan, S.; Sharma, A.; Luo, J.; Wang, J.; et al. Revealing the Role of Phase Structures of Bimetallic Nanocatalysts in the Oxygen Reduction Reaction. *ACS Catal.* **2018**, *8*, 11302–11313.
30. Li, J.; Xi, Z.; Pan, Y.; Spendelow, J. S.; Duchesne, P. N.; Su, D.; Li, Q.; Yu, C.; Yin, Z.; Shen, B.; et al. Fe Stabilization by Intermetallic L10 - FePt and Pt Catalysis Enhancement in L10 - FePt/Pt Nanoparticles for Efficient Oxygen Reduction Reaction in Fuel Cells.

J. Am. Chem. Soc. **2018**, *140*, 2926–2932.

31. Gunji, T.; Noh, S. H.; Tanabe, T.; Han, B.; Nien, C. Y.; Ohsaka, T.; Matsumoto, F. Enhanced Electrocatalytic Activity of Carbon-Supported Ordered Intermetallic Palladium − Lead (Pd 3 Pb) Nanoparticles toward Electrooxidation of Formic Acid. *Chem. Mater.* **2017**, *29*, 2906–2913.
32. Shi, Q.; Zhu, C.; Bi, C.; Xia, H.; Engelhard, M. H.; Lin, Y. Intermetallic Pd3Pb Nanowire Networks Boost Ethanol Oxidation and Oxygen Reduction Reactions with Significantly Improved Methanol Tolerance. *J. Mater. Chem.* **2017**, *5*, 23952–23959.
33. Bu, L.; Zhang, X.; Shen, X.; Su, D.; Lu, G.; Zhu, X.; Yao, J.; Guo, J.; Guo, S.; Huang, X. Surface Engineering of Hierarchical Platinum-Cobalt Nanowires for Efficient Electrocatalysis. *Nat. Commun.* **2016**, *7* (May), 1–10.
34. Lv, J.; Wang, Z.; Feng, J.; Qiu, R.; Wang, A.; Xu, X. Facile Synthesis of Highly Active Pd-Cu Nanowires Catalyst through a Simple Wet-Chemical Strategy for Ligand-Free Suzuki Cross Coupling Reaction. *Applied Catal. A, Gen.* **2016**, *522*, 188–193.
35. Yuan, T.; Wang, A.; Fang, K.; Wang, Z.; Feng, J. Hydrogen Evolution-Assisted One-Pot Aqueous Synthesis of Hierarchical Trimetallic PdNiRu Nanochains for Hydrazine Oxidation Reaction. *J. Energy Chem.* **2017**, *26* (6), 1231–1237.
36. Rong, H.; Mao, J.; Li, Y.; Xin, P.; He, D.; Chen, Y. Kinetically Controlling Surface Structure to Construct Defect-Rich Intermetallic Nanocrystals : Effective and Stable Catalysts. *Adv. Funct. Mater.* **2016**, *28*, 2540–2546.
37. Jana, R.; Bhim, A.; Bothra, P.; Pati, S. K.; Peter, S. C. Electrochemical Dealloying of PdCu3 Nanoparticles to Achieve Pt-like Activity for the Hydrogen Evolution Reaction. *ChemSusChem* **2016**, *9*, 2922–2927.

38. Zalineeva, A.; Baranton, S.; Coutanceau, C.; Jerkiewicz, G. Octahedral Palladium Nanoparticles as Excellent Hosts for Electrochemically Adsorbed and Absorbed Hydrogen. *Sci. Adv.* **2017**, *3*, 1–11.

39. Xi, Z.; Erdosy, D. P.; Mendoza-Garcia, A.; Duchesne, P. N.; Li, J.; Muzzio, M.; Li, Q.; Zhang, P.; Sun, S. Pd Nanoparticles Coupled to WO2.72 Nanorods for Enhanced Electrochemical Oxidation of Formic Acid. *Nano Lett.* **2017**, *17* (4), 2727–2731.

40. Yang, N.; Zhang, Z.; Chen, B.; Huang, Y.; Chen, J.; Lai, Z.; Chen, Y.; Sindoro, M.; Wang, A. L.; Cheng, H.; et al. Synthesis of Ultrathin PdCu Alloy Nanosheets Used as a Highly Efficient Electrocatalyst for Formic Acid Oxidation. *Adv. Mater.* **2017**, *29* (29), 1–6.

41. Hu, C.; Guo, Y.; Wang, J.; Yang, L.; Yang, Z.; Bai, Z.; Zhang, J.; Wang, K.; Jiang, K. Additive-Free Fabrication of Spherical Hollow Palladium/Copper Alloyed Nanostructures for Fuel Cell Application. *ACS Appl. Mater. Interfaces* **2012**, *4* (9), 4461–4464.

42. Xu, W.; Zhu, S.; Liang, Y.; Cui, Z.; Yang, X.; Inoue, A.; Wang, H. A Highly e Ffi Cient Electrocatalyst Based on Amorphous Pd – Cu – S Material for Hydrogen Evolution Reaction †. *J. Mater. Chem. A Mater. energy Sustain.* **2017**, *5*, 18793–18800.

Chapter 5

5 Conclusion

In summary, different nanomaterials systems were designed, synthesized, characterized and tested in different catalytic reaction. Overall, the nanomaterials studied in here present a synergistic effect that result in an enhancement in their properties. Each of the component of our materials are deeply investigated and studied to understand the overall effect in their electronic, magnetic and catalytical properties. Three projects were presented and developed during this study and they are next summarized.

First, stable $PdH_{0.43}$ and $Ni/PdH_{0.43}$ nanodendritic hydride materials were developed and catalytically tested for a greener process in benzyl alcohol oxidation reaction. Both nanodendrites, $PdH_{0.43}$ and $Ni/PdH_{0.43,}$ were found with a remarkable stability in what refers to composition and phase. In terms of catalytic activity, both nanostructures exhibited outstanding catalytic activity, higher than commercial Pd/C. Nonetheless, $Ni/PdH_{0.43}$ nanodendrites showed the highest selectivity towards benzaldehyde product and conversion rate of all of them due to the synergistic effect of Ni-rich surface and the $PdH_{0.43}$.

Second, another simple but efficient synthesis of palladium hydride nanoparticles with controllable morphologies, size and H:Pd ratios are investigated. Based on the rational design, stable β-PdHx with hydrogen ratios, up to x~0.6 were obtained as a result of the synergistic effect of palladium hydride and its surface decoration with organic molecules as amines and thiols which

are responsible of the multi-faceted properties of the materials. These encourage to continue finding prospects to achieve hydrogen storage materials with the ability of tune their properties at even room temperature and pressure.

Third, we finally presented a strategy for the synthesis and fabrication of alloys and intermetallic nanowires based on noble metals combined with non-noble metals to continue exploring the synergetic properties when they are combined in a one-dimensional nanostructure. Moreover, this approach is an example of new routes for the development of multifunctional catalysts which could encourage investigations to continue finding better options towards a universal catalyst at lower cost but still with high catalytic activity performance for diverse of catalytic reactions. Our synthesized alloy and intermetallic nanowires of PdCu were tested over important catalytic reactions as hydrogen evolution reaction (HER) in acid and basic media, and formic acid oxidation reaction (FAOR). Overall, it was demonstrated that our *PdCu nanowires exhibit enhanced electrocatalytic activity towards the mentioned reactions.